

EFFECTIVE BETA-DECAY OPERATORS WITH COUPLED CLUSTER
THEORY

By

Samuel John Novario

A DISSERTATION

Submitted to
Michigan State University
in partial fulfillment of the requirements
for the degree of

Physics—Doctor of Philosophy

2018

ABSTRACT

EFFECTIVE BETA-DECAY OPERATORS WITH COUPLED CLUSTER THEORY

By

Samuel John Novario

Coupled Cluster theory is a powerful *ab initio* framework for solving the many-body the Schrödinger equation and has been utilized successfully to describe the highly-correlated systems found in quantum chemistry and nuclear physics. This method uses a special similarity transformation to decouple a system's ground state from excitations from it. This transformation contains significant correlations that can be used to extend coupled cluster theory to excited states and open-shell systems with the equation-of-motions method. Additionally, properties of these states can be obtained by consistently transforming relevant operators using the coupled cluster similarity transformation. The coupled cluster method is systematically improvable and scales polynomially with the system size. With this flexibility and reach, coupled cluster theory can be applied across the nuclear chart to contribute to many important open problems in physics.

Several fundamental questions in modern physics involve electroweak interactions within nuclei, including the search for the elusive neutrinoless double-beta decay. Often the largest uncertainty within these experiments is due to nuclear-structure-dependent quantities that are calculated within some many-body framework. The main focus of this thesis is to apply the coupled cluster method to calculate effective Fermi and Gamow-Teller beta-decay operators between open shell states. By confirming the validity of this method, it can be extended to double-beta decay and other electroweak processes.

ACKNOWLEDGMENTS

First and foremost, I would like to thank my parents, Amy and Steve, for their unconditional support of my educational aspirations and passionate cultivation of my curiosities in addition to their persistent emotional, financial, and logistical aid they have provided during my long journey up till this point. Also, I would like to thank my siblings, Maggie, Lucy, and Charlie, for their friendship and inspiration, as well as the examples they set which I was able to follow. Moreover, I would like to thank my grandparents, aunts, uncles and cousins for their words of encouragement and praise. Lastly, I would like to thank my friends in East Lansing, Illinois, and around the country for helping me have fun and maintain my peace of mind, and never failing to ask me when I would graduate.

Next, I would like to thank my all my teachers throughout my long tenure as a student. I would especially like to acknowledge my science and math teachers that fostered and encouraged my interests. In particular, I would like to credit Bryon Leonard for opening my mind to the beauty of modern physics and the path that leads to where I am now. Additionally, I am thankful for Philippe Collon and Michael Thoennesen for giving me my first research opportunities as an undergraduate student when I'm sure I was more of a burden than a blessing.

I am grateful to Dr. Georg Bollen and Dr. Ryan Ringle for inviting me into the LEBIT collaboration, my first academic family. Along with my fellow graduate students, David Lincoln, Scott Bustabad, and Brad Barquest, my LEBIT colleagues helped me find my place as a graduate student, guided me as a scientist and collaborator, provided opportunities to travel and present at national conferences, and gave me research experience that few theorists hold. While in LEBIT, I was fortunate to share an office with Jenna Smith, who looked over

me as a young graduate student and gave me valuable advice and encouragement when it was greatly needed.

When I mentioned that I decided to change my research direction, my current advisor, Morten Hjorth-Jensen, without hesitation and without any solicitation from me, took a risk by taking me on as a student. For this, I am eternally grateful, and because Morten has become an invaluable mentor, colleague, and friend, I feel very lucky for finding myself in that situation. Along with my advisor, I would like to thank the members of my committee—Scott Bogner, Piotr Piecuch, Carlo Piermarocchi, and Remco Zegers—for agreeing to join my adventure through graduate school and guiding me along the way. I’m also indebted to Heiko Hergert for fielding my relentless questions, Ragnar Stroberg for unknowingly helping with his clean and well-commented code, and Kim Crosslan for shouldering most of my blunders for more than 7 years and for making sure I was aware of them.

Lastly, I would like to thank my fellow graduate students. To Justin Lietz, my office mate, world traveling partner, coupled-cluster colleague, and friend, I’m thankful for lending his advice, his expertise, and his ear. To Nathan Parzchowki, Titus Morris, and Fei Yuan, my fellow nuclear theory colleagues and friends, I’m thankful for their constant help and the pleasant work environment that they created.

And to all of the people that I haven’t mentioned, I realize that I am just a product of the circumstances that unfolded around me, especially the people with which I’ve crossed paths. So I’d like to give thanks to everyone, and to no one in particular, who helped shape my success in completing this dissertation.

TABLE OF CONTENTS

LIST OF TABLES	vii
LIST OF FIGURES	viii
KEY TO SYMBOLS AND ABBREVIATIONS	xiii
Chapter 1 Introduction	1
1.1 A Brief History of Nuclear Structure Theory	2
1.2 Electroweak Theory and Nuclear Structure	4
1.3 Ab-Initio Descriptions of Beta Decay	6
1.4 Thesis Structure	7
Chapter 2 Many-Body Quantum Mechanics	8
2.1 Independent-Particle Model	8
2.2 Second Quantization	10
2.3 Normal Ordering	12
2.4 Wick's Theorem	15
2.5 Hartree–Fock Method	20
2.6 Configuration-Interaction	25
2.7 Many-Body Perturbation Theory	27
2.7.1 Factorization Theorem	31
Chapter 3 Coupled-Cluster Theory	34
3.1 Exponential Ansatz	34
3.1.1 The Coupled Cluster Equations	37
3.2 Linked-Cluster Theorem and MBPT	38
3.3 Example: Pairing Model	43
3.4 Solving the Coupled Cluster Equations	48
3.4.1 Symmetry Channels	49
3.4.2 Matrix Structures and Intermediates	51
3.5 Example: Homogeneous Electron Gas	57
3.6 Coupled Cluster for Finite Nuclei	62
3.6.1 Harmonic Oscillator Basis	62
3.6.2 The Nuclear Interaction	65
3.6.3 Ground-State Results for Nuclei	68
3.7 Ground-State Center-of-Mass Factorization	71
Chapter 4 Equation-of-Motion Method	76
4.1 Equation-of-Motion States	77
4.2 Dual Solutions	80
4.2.1 Induced Three-Body Interaction	82
4.3 Solving the EOM equations	83

4.4	EOM-CC for 2D Quantum Dots	90
4.4.1	Quantum Dot Formalism	90
4.4.2	Quantum Dot Results	92
4.5	Quality of EOM Solutions	93
4.6	EOM-CC for Finite Nuclei	96
Chapter 5	Beta-Decay Effective Operators	103
5.1	Beta-Decay Properties	103
5.2	Coupled Cluster Effective Operators	108
Chapter 6	Conclusions and Perspectives	114
6.1	Summary and Conclusions	114
APPENDICES	116
Appendix A	CCSD Diagrams	117
Appendix B	Effective Hamiltonian Diagrams	124
Appendix C	Computational Implementation	131
Appendix D	Angular Momentum Coupling	142
REFERENCES	147

LIST OF TABLES

Table 5.1: Summary of the selection rules for allowed beta decays according to the angular momentum J and parity π of the initial (I) and final (F) states. 106

LIST OF FIGURES

Figure 1.1:	Nuclear chart of nuclei with ground-state energies which have been calculated with ab-initio methods and NN+3N interactions. Figure taken from [1].	3
Figure 1.2:	Progress of ab-initio nuclear structure from calculations of ground-state energies with NN+3N interactions. Early progress was approximately linear as the problem size scaled with Moore’s law while more recent progress has taken advantage of new algorithms which have outpaced Moore’s law. Data taken from [1].	5
Figure 2.1:	A depiction of the closed-shell reference state in the independent particle model. Each horizontal line represents a shell of single-particle orbits, represented by circles, and the dotted line represents the Fermi level which separates the unoccupied <i>particle</i> states from the occupied <i>hole</i> states.	13
Figure 2.2:	A depiction of 1p-1h, 2p-2h, 1p-0h, and 0p-1h Slater determinants defined relative to the reference state in the independent particle model.	14
Figure 2.3:	Scaling of the matrix size and number of non-zero matrix elements for nuclear CI calculations of light nuclei. Even for modestly-sized model spaces, the memory requirements approach the limit of petascale supercomputers ($\sim 10^{10}$). Figure taken from [2].	27
Figure 3.1:	Schematic representation of the pairing model space. The shells are equally spaced and doubly degenerate with one spin-up and one spin-down state.	43
Figure 3.2:	Correlation energy for the pairing model with exact diagonalization, CCD, and perturbation theory to third (MBPT3) and fourth order (MBPT4) for a range of interaction values, g	46
Figure 3.3:	Visualization of the CCD similarity transform on the pairing Hamiltonian for four particles and six shells. This shows the main function of CCD, which is to decouple 2p-2h excitations from the ground state, shown by the suppression of matrix elements on the first column. In the pairing model, this also has the effect of decoupling 2p-2h excitations from 4p-4h excitations. Also, the non-unitary nature of the transformation is obvious given the asymmetry of the resulting Hamiltonian.	48

Figure 3.4: Visulization of the Fourier transform of a finite box. This transformation characterizes the construction of the single-particle basis for infinite matter, mapping plane waves in coordinate space onto finitely-spaced points in momentum space.	59
Figure 3.5: CCD energy per electron in Hartrees for the 3D homogeneous electron gas as function of the Wigner-Seitz radius in units of Bohr radii. The calculation used periodic boundary conditions and a basis with 25 shells, resulting in a total of 1238 single-particle states. Also plotted are the variational quantum Monte Carlo (VMC) results from [3].	61
Figure 3.6: A schematic illustration of the harmonic oscillator basis used for calculations of nuclei. Shown is an example of a initial reference state for carbon-14, with 6 protons filled to the p3/2-subshell closure and 8 neutrons filled to the p1/2-shell closure. See text for details on the single-particle states.	64
Figure 3.7: Diagrammatic form of the chiral EFT expansion up to N ³ LO. The solid lines represent nucleons and the dashed lines represent pions. The different vertices represent higher-order interactions. Figure taken from [4]. . .	67
Figure 3.8: Ground-state energies for ¹⁶ O for the EM N ³ LO NN only interaction and with the added 3N interaction from Navrátil, both SRG softened with $\lambda_{\text{SRG}} = 1.88, 2.24 \text{ fm}^{-1}$. The energies are plotted for $e_{\max} = 10, 12$. The most obvious difference is between the NN and NN+3N calculations, showing the importance of including 3N forces. The differences between the cutoff parameters are resolved within $\sim 1\%$ with the inclusion of 3N forces and can be rectified further by including additional correlations or full 3N forces. The experimental binding energy is shown with the grey dashed line.	69
Figure 3.9: Ground-state energies for doubly magic nuclei as a function of the harmonic oscillator energy $\hbar\omega$ with the NN+3N(400) interaction, SRG softened with $\lambda_{\text{SRG}} = 2\text{fm}^{-1}$. The energies are plotted for $e_{\max} = 8, 10, 12$, showing the convergence as the model space increases. The results are independent of the underlying oscillator frequency to $\sim 1\%$ for $e_{\max} = 12$. The grey dashed line is the experimental binding energy. The overbinding of this interaction becomes apparent as the system size increases.	70
Figure 3.10: Ground-state energies for singly magic nuclei as a function of the harmonic oscillator energy $\hbar\omega$ with the NN+3N(400) interaction, SRG softened with $\lambda_{\text{SRG}} = 2\text{fm}^{-1}$. The energies are plotted for different e_{\max} . The results are independent of the underlying oscillator frequency to $\sim 1\%$ for $e_{\max} = 12$. The grey dashed line is the experimental binding energy. These results underbind with respect to their doubly-magic counterparts in Fig. 3.9.	71

Figure 3.11: Ground-state COM energies, Eq. (3.68), for ^{16}O and ^{40}Ca at various harmonic oscillator frequencies with the NN+3N(400)-induced interaction with $\lambda_{\text{SRG}} = 2.0 \text{ fm}^{-1}$ at $e_{\max} = 12$. Using the proper COM oscillator frequencies shows the approximate factorization of Eq. (3.67).	75
Figure 4.1: The 42 lowest single-particle states (the first 5 shells) in the 2D harmonic oscillator basis. Each box represents a single-particle state arranged by m_ℓ , m_s , and energy, and the up/down arrows indicate the spin of the states. Within each column, the principal quantum number n increases as one traverses upward.	91
Figure 4.2: Ground state energy (in Hartrees) of quantum dots with N particles and an oscillator frequency of ω calculated with several different methods.	93
Figure 4.3: Particle-attached energy (in Hartrees) of quantum dots with N particles and an oscillator frequency of ω calculated with several different methods.	94
Figure 4.4: Particle-removed energy (in Hartrees) of quantum dots with N particles and an oscillator frequency of ω calculated with several different methods.	94
Figure 4.5: Energy difference of particle-attached and particle-removed states between the EOM-CC method and the exact FCI method for a quantum dot with various parameters plotted against the single-particle overlap of the FCI state, n_1 -particle or n_1 -hol, see Eqs. (4.42) and (4.43). The strong correlation shows that the quality of EOM states can be judged by this metric.	96
Figure 4.6: Ground-state energies for the particle-attached nuclei ^{17}O , ^{17}F , ^{23}O , and ^{23}F as a function of the harmonic oscillator energy $\hbar\omega$ with the NN+3N(400) interaction, SRG softened with $\lambda_{\text{SRG}} = 2\text{fm}^{-1}$. The energies are plotted for $e_{\max} = 8, 10, 12$, showing the convergence as the model space increases. The grey dashed line is the experimental binding energy.	97
Figure 4.7: Ground-state energies for the particle-removed nuclei ^{15}N , ^{15}O , ^{21}N , and ^{21}O as a function of the harmonic oscillator energy $\hbar\omega$ with the NN+3N(400)-induced interaction, SRG softened with $\lambda_{\text{SRG}} = 2\text{fm}^{-1}$. The energies are plotted for $e_{\max} = 8, 10, 12$, showing the convergence as the model space increases. The grey dashed line is the experimental binding energy.	98

Figure 4.8: Ground-state COM energies, Eq. (3.68), for open-shell nuclei at varies harmonic oscillator frequencies with the NN+3N(400)-induced interaction with $\lambda_{\text{SRG}} = 2.0 \text{ fm}^{-1}$ at $e_{\max} = 12$. The top row shows the results for the particle-attached nuclei ^{17}O , ^{17}F , ^{23}O , and ^{23}F , and the bottom row shows the results for the particle-removed nuclei ^{15}N , ^{15}O , ^{21}N , and ^{21}O . The right column shows that the COM wave function practically vanishes according to Eq. (3.67).	100
Figure 4.9: Low-lying PA-EOM states for ^{17}O and ^{17}F with and without a Lawson-Gloeckner term, along with the experimentally determined spectra. The negative-parity states are COM contaminants and are removed by artificially raising the COM excitation energy with the parameter β according to Eq. (3.72).	101
Figure 4.10: Low-lying PA-EOM states for ^{23}O and ^{23}F with and without a Lawson-Gloeckner term. The negative-parity states in ^{17}O are COM contaminants and are removed by artificially raising the COM excitation energy with the Lawson-Gloeckner method, Eq. (3.72). The excited states of these nuclei have not been experimentally determined.	101
Figure 4.11: Low-lying PR-EOM states for ^{15}N and ^{15}O with and without a lawson-gloeckner term, and the experimentally determined spectra. The $1/2^+$ state is a COM contaminant and is removed by artificially raising the COM excitation energy with the parameter β according to Eq. (3.72).	102
Figure 4.12: Low-lying PA-EOM states for ^{21}N and ^{21}O with and without a Lawson-Gloeckner term, Eq. (3.72), and the experimentally determined spectra. The negative-parity states in ^{17}O are COM contaminants and are removed by artificially raising the COM excitation energy. The excited states of these nuclei have not been experimentally detemined.	102
Figure 5.1: Schematic representations of the three free-space weak processes in this work: β^- decay (a), β^+ decay (b), and electron-capture (c). The coupling constant for the point interaction vertex is the weak-interaction coupling constant g_W	105
Figure 5.2: Schematic representations of a higher-order weak interactions involving pion-exchange that occur within a nucleus, for β^- decay (a), β^+ decay (b), and electron-capture (c). These processes are not included in the impulse approximation. The coupling constant for the point interaction vertex is the effective weak-interaction coupling constant G_F	105

Figure 5.3: Schematic representations of the impulse approximations to the different weak processes within an A -body nucleus: β^- decay (a), β^+ decay (b), and electron-capture (c). The active nucleon doesn't interact with the initial and final nuclei during the weak process. The coupling constant for each interaction vertex is the weak-interaction coupling constant G_F . 106

KEY TO SYMBOLS AND ABBREVIATIONS

$Ap\text{-}Bh$ – A -particle, B -hole excitation or de-excitation from the reference state

$|0\rangle$ – vacuum state

$|\Phi_0\rangle$ – reference state

$|\Psi\rangle$ – correlated ground state

$|\Phi_{i_1 \dots i_B}^{a_1 \dots a_A}\rangle$ – specific $Ap\text{-}Bh$ state

$\{\dots\}$ – normal-ordered with respect to the reference state

$\hbar\omega$ – harmonic oscillator energy scale

\hat{H} – Hamiltonian

\bar{H} – similarity-transformed Hamiltonian

\hat{H}_N – normal-ordered Hamiltonian

\bar{H}_N – normal-ordered similarity-transformed Hamiltonian

\hat{T} – cluster operator

$\varepsilon_{i_1 \dots i_B}^{a_1 \dots a_A}$ – energy denominator, $f_{i_1}^{i_1} + \dots + f_{i_B}^{i_B} - f_{a_1}^{a_1} - \dots - f_{a_A}^{a_A}$

CC – coupled cluster

CCD – coupled cluster with doubles

CCSD – coupled cluster with singles and doubles

CCSDT – coupled cluster with singles, doubles, and triples

CI – configuration interaction

FCI – full configuration interaction

COM – center of mass

EOM – equation-of-motion

PA – particle-attached

PR – particle-removed

HF – Hartree-Fock

IM-SRG – in-medium similarity renormalization group

HO – harmonic oscillator

MBPT – many-body perturbation theory

DIIS – direct-inversion of the iterative subspace

QCD – quantum chromodynamics

EFT – effective field theory

NN – nucleon-nucleon

3N – three-nucleon

NLO – next-to leading order

N^2LO – next-to-next-to leading order

N^3LO – next-to-next-to-next-to leading order

Chapter 1

Introduction

Steady progress in any modern scientific endeavor requires a strong, dynamic relationship between experimental data to paint an accurate picture of some natural phenomena and theoretical models to interpret those phenomena with respect to the growing network of other scientific models. Conversely, the predictive capability of theoretical models can highlight blurry or unfinished areas of that picture which can be clarified or completed by new or improved experimental techniques. In the pursuit to understand and describe the atomic nucleus and the corresponding implications from quarks to neutron stars, this push-and-pull coordination between theory and experiment makes progress in modern nuclear physics robust and persistent.

An integral component of modern nuclear physics is describing the structure and emergent properties of self-bound systems of protons and neutrons. The systems in question can be stable nuclei, rare isotopes far from stability, and even infinite nuclear matter which can be used to model neutron stars. Relevant properties to nuclear structure include ground-state energies—for determining nuclear masses, excited-state energies—for identification in gamma or neutron spectroscopy, and transition or decay amplitudes—for calculating the respective rates for those processes. This wide array of emergent properties inserts both nuclear structure theory and experiment into a prominent role within every other subfield of modern nuclear physics, from lattice quantum chromodynamics (QCD) to nuclear astrophysics, and beyond, to questions about fundamental symmetries and dark matter. However, two inextricable characteristics of a comprehensive model of nuclear structure—the increasingly large

size of many-body nuclear systems and the complexity and strength of the nucleon-nucleon interactions—have been imposing hurdles for theorists to overcome.

1.1 A Brief History of Nuclear Structure Theory

A major step in the project to solve the correlation problem in many-fermion systems was taken with the work of Brueckner, Bethe, and Goldstone [5, 6, 7] with the reformulation of the nuclear interaction by accounting for two-body correlations from the nuclear medium. This work continued with the work of Coester [8, 9] and Kummel [10], amongst many others, with a further resummation of nuclear correlations in the form of an exponential ansatz into what would become coupled-cluster (CC) theory. However, there were two major obstacles that hindered the progress in this area for decades. First, while these methods were systematically improvable by including progressively higher-level correlations, the highly nonperturbative nature of the nuclear force required computationally infeasible summations. Second, there wasn't a reliable and consistent theory to model nucleon-nucleon interactions.

On the other hand, with the well-known and highly-perturbative Coulomb force, which underlies the many-electron systems in atoms and molecules, the field of quantum chemistry made consistent advances in *ab-initio* quantum chemistry possible since the 1950s. Along with the quasi-exact method of configuration interaction (CI) theory [11, 12, 13, 14] which have been utilized since the formulation of quantum mechanics, chemists successfully employed approximate methods like many-body perturbation theory (MBPT) [15, 16, 17, 18] and coupled-cluster theory [19, 20, 21, 22, 18].

Fortunately, within the past decade, two breakthroughs have allowed *ab initio* nuclear structure to resurface and thrive the way that quantum chemistry had done in the previous decades. First was the invention of chiral effective field theory (EFT) [23, 24] which gave

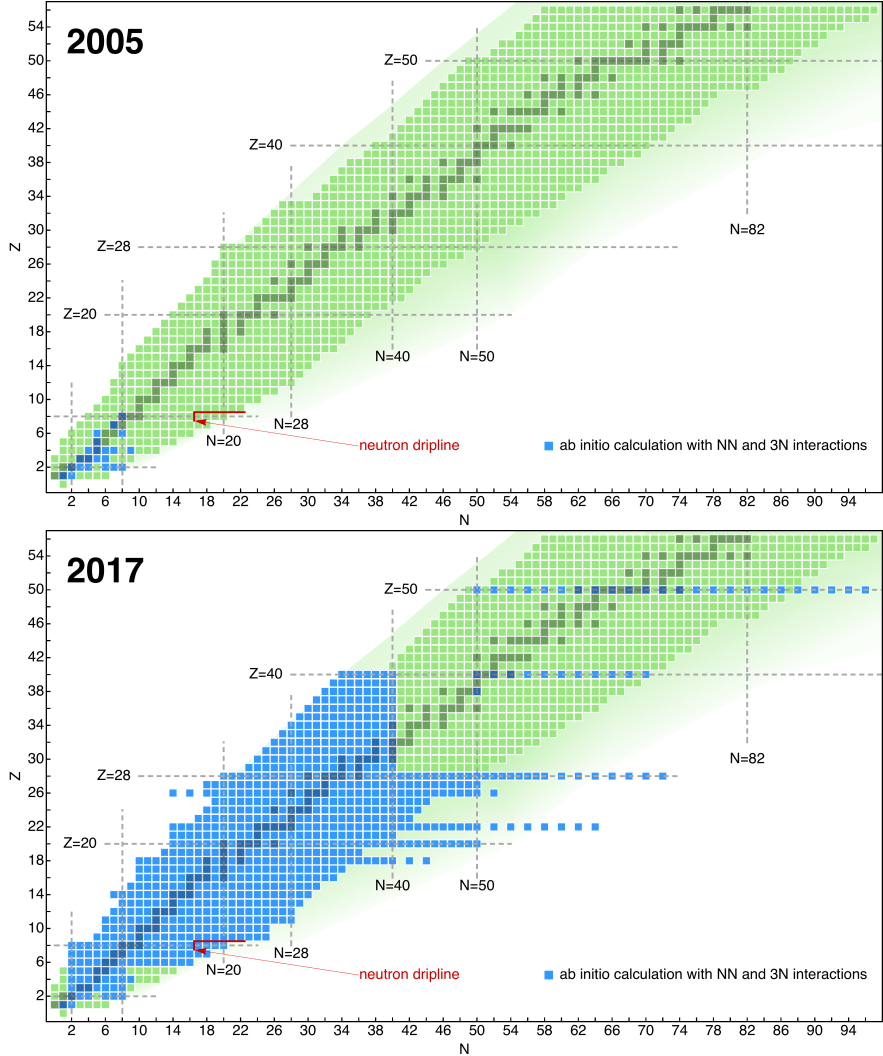


Figure 1.1: Nuclear chart of nuclei with ground-state energies which have been calculated with ab-initio methods and NN+3N interactions. Figure taken from [1].

theorists the ability to construct nucleon-nucleon interactions consistent with the underlying QCD of the strong nuclear force. Second was the application of renormalization group (RG) methods to the nuclear force [25, 26]. This procedure can “soften” the NN interaction, to decouple the high- and low-momentum components of the nuclear force and generate less-correlated systems that can be calculated at a reasonable computational cost. These major changes to nuclear structure theory made it possible to merge the field with the progress of quantum chemistry and open a new area for additional developments in *ab initio* descriptions

of many-fermion systems, see Fig. 1.1.

Along with exponential improvements to high-performance computing, these novel techniques have allowed modern many-body methods to extend their reach and deepen their applicability across the nuclear chart, see Fig. 1.2. The no-core shell model (NCSM), an exact method for a given model space, has been useful in calculating the radii, transition strengths, and effective interactions of light nuclei and has been extended to nuclei in the *sd* shell [27, 28, 29]. A quasi-exact technique which follows a completely different methodology than NCSM, quantum Monte Carlo (QMC), has also progressed and is now capable of calculating properties of light nuclei with modern chiral forces [30, 31, 32]. In addition to these exponentially scaling techniques' successes with lighter nuclei, polynomially scaling techniques—such as the in-medium similarity renormalization group (IMSRG) [33, 34, 35, 36, 37, 38, 39, 40], self-consistent Green's functions (SCGF) [41, 42, 43], and coupled cluster theory [44, 45, 46, 47, 48, 49, 50, 51]—have been able to reach open-shell nuclei through the *pf* shell and even up to the chain of even tin isotopes with equations-of-motion and multi-reference techniques [52].

1.2 Electroweak Theory and Nuclear Structure

Nuclear structure is implicated in performing and analyzing experiments to probe fundamental symmetries and physics beyond the Standard Model. One example is determining the V_{ud} component of the Cabibbo-Kobayashi-Maskawa (CKM) matrix, which relates quark eigenstates of the weak interaction to their mass eigenstates [53, 54]. This component can be determined from by measuring the half-lives of superallowed beta decays [55] and applying a nucleus-dependent structure correction [56, 57, 58, 59, 60]. The value of $|V_{ud}|$ is used to test the unitarity of the CKM matrix and the conserved-vector current hypothesis, which

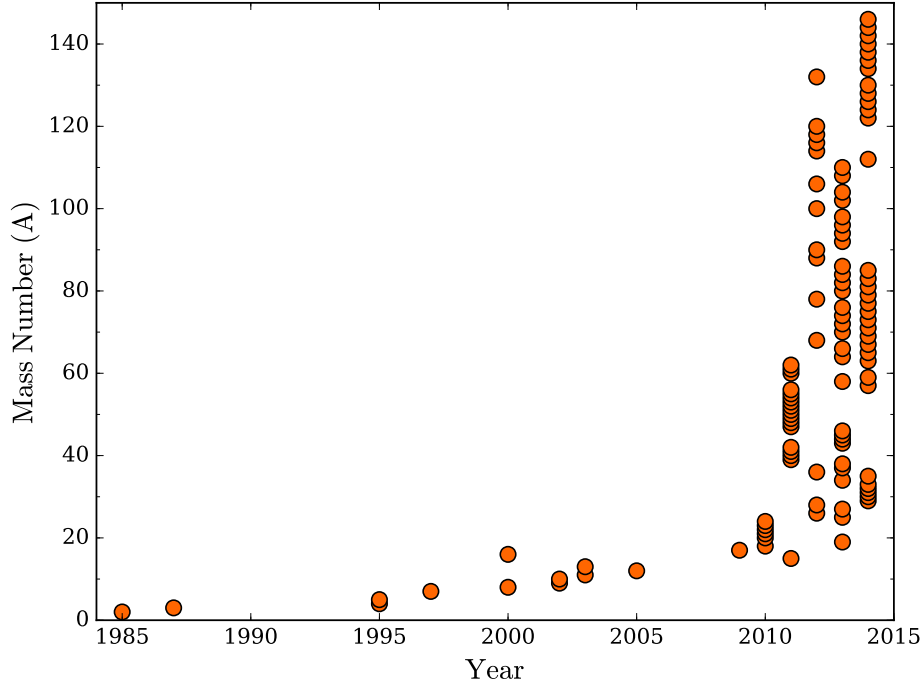


Figure 1.2: Progress of ab-initio nuclear structure from calculations of ground-state energies with NN+3N interactions. Early progress was approximately linear as the problem size scaled with Moore’s law while more recent progress has taken advantage of new algorithms which have outpaced Moore’s law. Data taken from [1].

relates the ft -values of superallowed Fermi β decays of different nuclei, both predicted by the standard model [61].

Another example of physics beyond the standard model is the neutrinoless double-beta decay ($0\nu\beta\beta$) [62, 63]. The extremely-rare, two-neutrino double-beta decay ($2\nu\beta\beta$) has been observed in many experiments [64, 65], which has motivated the search for its neutrinoless counterpart, in which two Majorana neutrinos, being their own antiparticles, annihilate one another, which is not possible in the standard electro-weak theory. The long half-lives of these theoretical decays depend on a phase-space factor, which is highly dependent on the decay Q -value, and a nuclear matrix element. The Q -value can be determined from high-precision mass measurements of the relevant nuclei [66, 67, 68, 69], while the nuclear matrix element, which contributes the largest source of uncertainty, must be calculated with

a reliable many-body theory.

The weak interaction and nuclear structure can also be exploited for supernova neutrino detection and spectroscopy. While these original detectors were based on electron-neutrino scattering [70, 71], more recent experiments utilize correlated nucleon effects of large nuclei to enhance the scattering cross section and therefore the ability to resolve energies and distinguish neutrino flavors [72, 73, 74, 75]. Supernova models predict distinct distributions for different neutrino flavors based on the temperatures at which they are emitted [76, 77]. With nuclear structure calculations that include sufficient nuclear correlations, these high-resolution detectors can be used to verify specific models.

1.3 Ab-Initio Descriptions of Beta Decay

Since Enrico Fermi's originally rejected paper describing beta decay in 1934 [78, 79], theorists have worked to refine this description within the ever-growing library of knowledge concerning the nature of the weak force, the characteristics of the neutrino, and the structure of nuclei. With the success of *ab initio* calculations for nuclear properties such as masses, radii, and electromagnetic phenomena, these techniques also seem promising ways to calculate relevant quantities involved in nuclear beta decay. Because the kinematics of the decay and the underlying weak process are well understood, the remaining task for nuclear theory to tackle is calculating the transition amplitudes between the initial and final nuclei.

Modern calculations of these beta-decay matrix elements were originally performed using phenomenological interactions in the shell model framework [80, 81, 82, 83]. Also, predecessors to current ab-initio techniques like the random-phase approximation (RPA) [84] included core-correlation effects in these early descriptions. These methods were able to successfully reproduce experimental lifetime data and address technical issues such as the quenching of

the axial-vector coupling constant. More recently, the success of the shell model has inspired an extension to the new method, known as the ab-initio shell model [29], where an effective interaction is constructed within a certain valence space using a many-body method such as CC [85] or IMSRG [86]. However, these techniques are computationally expensive and cannot currently reach heavy nuclei of interest. The most common method used in their place is known as the quasiparticle random-phase approximation (QRPA) [87, 88]. While these calculations can be performed for heavy nuclei in large spaces, they also rely on phenomenological effective interactions. Therefore, there is a demand for computationally-economical, *ab initio* techniques that can capture the relevant many-body correlations needed to accurately describe the nuclear structure aspects of electro-weak processes.

1.4 Thesis Structure

The main goal of this work is to explore the *ab initio* description of nuclear beta decay within the coupled-cluster theory framework of the *equation-of-motion coupled cluster with singles and doubles* (EOM-CCSD) method using renormalized chiral NN and 3N interactions. The organization of the thesis builds from a general description of the many-body problem of quantum mechanics in chapter 2. Then, in chapter 3, this many-body framework is applied within the coupled-cluster theory and applied to various systems including, atomic nuclei. In chapter 4, coupled-cluster theory is extended to the equation-of-motion method to describe open-shell systems. Then, in chapter 5, different types of beta decay are described in detail then outlines the procedure to express beta-decay observables as effective coupled-cluster operators and how to calculate those observables in the equation-of-motion framework. Lastly, conclusions and future perspectives are given in chapter 6 while technical details concerning the formalism and implementation are given in the appendices A – D.

Chapter 2

Many-Body Quantum Mechanics

Ab initio structure calculations of many-fermion systems such as those in nuclear and electronic structure aim to describe emergent phenomena from the constituent particles subject to the underlying microscopic Hamiltonian. This amounts to finding the solution to the many-body Schrödinger equation. However, a calculation of the exact solution needs to account for all possible correlations among the particles and thus scales factorially. This motivates the need for approximations to the exact solution that account for the most important correlations. This chapter first establishes the formalism necessary to define the many-body problem then illustrates several successive approximations to its solution. Because the type of fermions and the underlying Hamiltonian can be kept generic until specific systems are considered, the formalism and many-body methods can be kept generic as well.

2.1 Independent-Particle Model

The nonrelativistic A -body quantum problem begins with the Schrödinger equation,

$$\hat{H}\Psi_\nu(\mathbf{r}_1, \dots, \mathbf{r}_A) = E_\nu\Psi_\nu(\mathbf{r}_1, \dots, \mathbf{r}_A), \quad (2.1)$$

for the correlated wave function $\Psi_\nu(\mathbf{r}_1, \dots, \mathbf{r}_A)$ and the corresponding energy E_ν . The Hamiltonian can be written generically as a sum of k -body pieces which, in principle, can

contain up to A -body interactions,

$$\begin{aligned}\hat{H} &= {}^{(1)}\hat{H} + {}^{(2)}\hat{H} + {}^{(3)}\hat{H} + \dots \\ &= \sum_i^A {}^{(1)}\hat{H}(\mathbf{r}_i) + \sum_{i < j}^A {}^{(2)}\hat{H}(\mathbf{r}_i, \mathbf{r}_j) + \sum_{i < j < k}^A {}^{(3)}\hat{H}(\mathbf{r}_i, \mathbf{r}_j, \mathbf{r}_k) + \dots\end{aligned}\quad (2.2)$$

The one-body term can contain the kinetic energy operator, $\frac{-\hbar^2}{2m}\nabla_i^2$, as well as any external potential while the higher-order terms contain inter-particle interactions.

An intuitive way to formulate the solution to the many-body Schrödinger equation is to express the collective wave function in terms of independent single-particle wave functions, or orbitals $\phi(\mathbf{r})$. In this *independent-particle model*, a selection of single-particle wave functions, known as the single-particle basis, are constructed by solving the Schrödinger equation for a single particle in either a mean-field potential for bound systems or in free space for infinite systems. Then a many-body wave function is constructed as a product of these single-particle orbits. This simple model is justified because it becomes exact when inter-particle interactions are completely suppressed and is useful because it provides an intuitive way to interpret complicated many-body dynamics as processes involving few single-particle wave functions.

A many-body wave function of fermions must be anti-symmetric with respect to particle exchange so that the Pauli exclusion principle is followed, such that no single-particle wave function is occupied by more than one fermion. This condition is satisfied by a wave function in the form of a *Slater determinant* [89],

$$\Phi(\mathbf{r}_1, \dots, \mathbf{r}_A) = \frac{1}{\sqrt{A!}} \begin{vmatrix} \phi_1(\mathbf{r}_1) & \phi_1(\mathbf{r}_2) & \cdots & \phi_1(\mathbf{r}_A) \\ \phi_2(\mathbf{r}_1) & \phi_2(\mathbf{r}_2) & \cdots & \phi_2(\mathbf{r}_A) \\ \vdots & \vdots & \ddots & \vdots \\ \phi_A(\mathbf{r}_1) & \phi_A(\mathbf{r}_2) & \cdots & \phi_A(\mathbf{r}_A) \end{vmatrix}, \quad (2.3)$$

where A is the number of particles in the system and $\phi_p(\mathbf{r}_\mu)$ is the p -th orbital filled with the μ -th particle.

If the orbitals are constructed from an appropriate phenomenological potential, a Slater determinant composed of the A lowest orbitals can represent a fairly good approximation to the ground state for a closed-shell system, where the lowest-energy Slater determinant can be uniquely determined. The set of all Slater determinants in a certain model space of single-particle wave functions defines a complete A -body Hilbert space such that a generic wave function can be written as a linear combination of Slater determinants,

$$\Psi_\nu(\mathbf{r}_1, \dots, \mathbf{r}_A) = \sum_{\mu=1}^{\mathcal{N}} C_\nu^\mu \Phi_\mu(\mathbf{r}_1, \dots, \mathbf{r}_A), \quad (2.4)$$

where $C_\nu^\mu = \langle \Psi(\mathbf{r}_1, \dots, \mathbf{r}_A) | \Phi_\nu^\mu(\mathbf{r}_1, \dots, \mathbf{r}_A) \rangle$. The number of Slater determinants \mathcal{N} in an A -body Hilbert space with N orbits is given by,

$$\mathcal{N} = \binom{N}{A} = \frac{N!}{A!(N-A)!}, \quad (2.5)$$

which shows the factorial scaling of the exact problem. However, to reduce the size of the problem, progressively more significant Slater determinants can be chosen to systematically refine approximations to the full solution.

2.2 Second Quantization

Even with the simplification of the independent-particle model, the many-body Schrödinger equation is an unwieldy and complex system of coupled differential equations. A useful reformulation of this equation is to promote the single-particle orbits to operators in a step

known as *second quantization* (see e.g., [18, 90]). In this framework, a Slater determinant is represented by a string of occupied orbitals,

$$\Phi(\mathbf{r}_1, \dots, \mathbf{r}_A) \equiv \mathcal{A}(\phi_{p_1} \phi_{p_2} \phi_{p_3} \cdots \phi_{p_N}) \equiv |p_1 p_2 p_3 \cdots p_N\rangle, \quad (2.6)$$

where \mathcal{A} represents a permutation and normalization operator to correspond with Eq. (2.3). These second-quantized Slater determinants can be constructed with the use of operators that correspond to specific orbitals. A *creation* operator, \hat{a}_p^\dagger , places a particle in the p orbital, and an *annihilation* operator, \hat{a}_p , removes a particle from the p orbital,

$$\hat{a}_p^\dagger |0\rangle = |p\rangle \quad \hat{a}_p |p\rangle = |0\rangle, \quad (2.7)$$

where $|0\rangle$ represents the true vacuum, a state void of any particles. Because there must be a correspondence between the original first quantization and second quantization, these creation and annihilation operators obey the following anticommutation relations ($[\hat{A}, \hat{B}]_+ = \hat{A}\hat{B} + \hat{B}\hat{A}$),

$$[\hat{a}_p^\dagger, \hat{a}_q]_+ = \delta_{pq} \quad [\hat{a}_p^\dagger, \hat{a}_q^\dagger]_+ = [\hat{a}_p, \hat{a}_q]_+ = 0, \quad (2.8)$$

which guarantee that wave functions comprised of these operators obey antisymmetry and the Pauli exclusion principle required of fermionic systems.

The Hamiltonian in the form of Eq. (2.2) can be written with second-quantized operators as,

$$\hat{H} = \sum_{pq} {}^{(1)}H_q^p \hat{a}_p^\dagger \hat{a}_q + \frac{1}{4} \sum_{pqrs} {}^{(2)}H_{rs}^{pq} \hat{a}_p^\dagger \hat{a}_q^\dagger \hat{a}_s \hat{a}_r + \frac{1}{36} \sum_{pqrstu} {}^{(3)}H_{stu}^{pqr} \hat{a}_p^\dagger \hat{a}_q^\dagger \hat{a}_r^\dagger \hat{a}_u \hat{a}_t \hat{a}_s + \dots, \quad (2.9)$$

where the prefactors account for the double counting of particle-particle interactions, and

the matrix elements represent integrals over the relevant single-particle wave functions,

$$\begin{aligned}
{}^{(1)}H_q^p &\equiv \int d\mathbf{r}_1 \phi_p^*(\mathbf{r}_1) {}^{(1)}\hat{H}(\mathbf{r}_1) \phi_q(\mathbf{r}_1) \\
{}^{(2)}H_{rs}^{pq} &\equiv \int d\mathbf{r}_1 d\mathbf{r}_2 \phi_p^*(\mathbf{r}_1) \phi_q^*(\mathbf{r}_2) {}^{(2)}\hat{H}(\mathbf{r}_1, \mathbf{r}_2) [\phi_r(\mathbf{r}_1) \phi_s(\mathbf{r}_2) - \phi_s(\mathbf{r}_1) \phi_r(\mathbf{r}_2)] \\
&\vdots
\end{aligned} \tag{2.10}$$

Matrix elements involving two or more particles include exchange terms which guarantee that they are also antisymmetric,

$$\begin{aligned}
{}^{(2)}H_{rs}^{pq} &= -{}^{(2)}H_{rs}^{qp} = -{}^{(2)}H_{sr}^{pq} = {}^{(2)}H_{sr}^{qp} \\
{}^{(3)}H_{stu}^{pqr} &= -{}^{(3)}H_{stu}^{qpr} = -{}^{(3)}H_{tsu}^{pqr} = {}^{(3)}H_{tsu}^{qpr} = \dots
\end{aligned} \tag{2.11}$$

These definitions apply regardless of the form of the Hamiltonian, and thus this formalism remains generic to the particular system. Second quantization is a crucial step in simplifying the many-body Schrödinger equation because it reduces the complexity of the spatial and spin degrees of freedom within the single-particle wave functions and interactions into precomputed matrix elements. The remaining effort is reduced to algebraic expressions involving creation and annihilation operators.

2.3 Normal Ordering

It's convenient to define an A -particle reference state, where states are filled from the true vacuum up to a closed shell, known as the Fermi level. This reference state must be uniquely determined from the number of particles in the system and therefore nondegenerate with

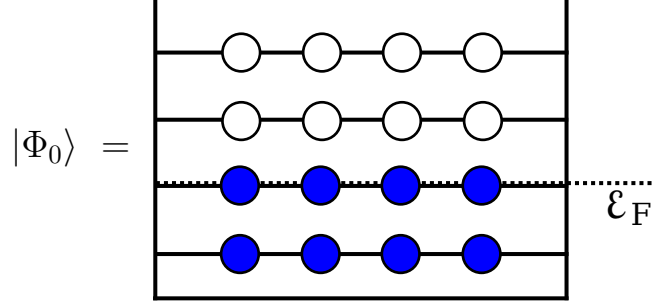


Figure 2.1: A depiction of the closed-shell reference state in the independent particle model. Each horizontal line represents a shell of single-particle orbits, represented by circles, and the dotted line represents the Fermi level which separates the unoccupied *particle* states from the occupied *hole* states.

other Slater determinants,

$$|\Phi_0\rangle = \left\{ \prod_i^A \hat{a}_i^\dagger \right\} |0\rangle. \quad (2.12)$$

This reference determinant defines a new *Fermi vacuum*. States above the Fermi vacuum are called *particle* states and will be denoted with the indices $a, b, c, d\dots$ while states below the Fermi vacuum are called *hole* states and will be denoted with the indices $i, j, k, l\dots$. Generic states above or below the Fermi vacuum will be denoted with the indices $p, q, r, s\dots$.

Any other Slater determinant can be constructed relative to this reference state by adding particles and/or removing holes. A Slater determinant with A particles added and B holes removed from reference state is known as a Ap - Bh excitation. A 1p-1h state is constructed by removing a particle in the occupied state i and adding a particle in the unoccupied state a ,

$$|\Phi_i^a\rangle \equiv \hat{a}_a^\dagger \hat{a}_i |\Phi\rangle. \quad (2.13)$$

Equivalently, a 2p-2h state is constructed by removing particles in states i and j then adding them to states b and a ,

$$|\Phi_{ij}^{ab}\rangle \equiv \hat{a}_a^\dagger \hat{a}_b^\dagger \hat{a}_j \hat{a}_i |\Phi\rangle. \quad (2.14)$$

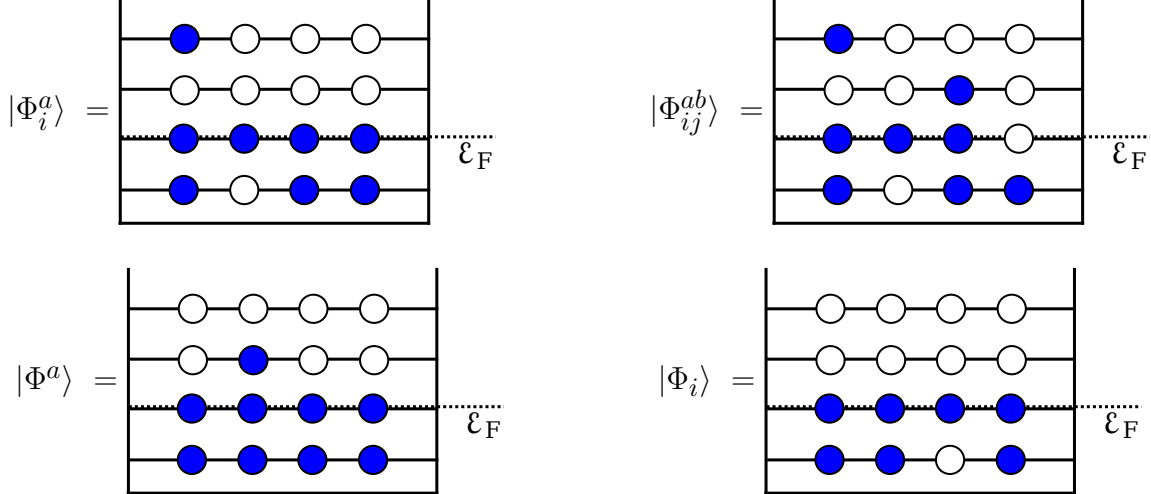


Figure 2.2: A depiction of 1p-1h, 2p-2h, 1p-0h, and 0p-1h Slater determinants defined relative to the reference state in the independent particle model.

The number of creation and annihilation operators doesn't necessarily have to be equal. For instance, a single particle can be added on top of the reference state with a single creation operator,

$$|\Phi^a\rangle \equiv \hat{a}_a^\dagger |\Phi\rangle, \quad (2.15)$$

and a particle can be removed with a single annihilation operator,

$$|\Phi_i\rangle \equiv \hat{a}_i |\Phi\rangle. \quad (2.16)$$

Using these definitions, hole-creation and particle-annihilation operators vanish when acting on the Fermi vacuum from the left, $\hat{a}_i^\dagger |\Phi_0\rangle = \hat{a}_a |\Phi_0\rangle = 0$. Conversely, hole-annihilation and particle-creation operators vanish when acting on the Fermi vacuum from the right, $\langle \Phi_0 | \hat{a}_i = \langle \Phi_0 | \hat{a}_a^\dagger = 0$.

These results can be exploited to simplify expressions involving strings of creation and annihilation operators by a procedure called *normal ordering* with respect to the Fermi vacuum. Denoted by $\{\dots\}$, normal ordering permutes a string of creation and annihilation

operators so that hole-annihilation and particle-creation operators are to the left of hole-creation and particle-annihilation operators, which guarantees that normal ordered operators vanish on the Fermi vacuum, $\langle \Phi_0 | \{ \cdots \} = 0$ and $\{ \cdots \} | \Phi_0 \rangle = 0$.

$$\left\{ \hat{a}_j^\dagger \cdots \hat{a}_i \cdots \hat{a}_b \cdots \hat{a}_a^\dagger \right\} = (-1)^\sigma \hat{a}_i \cdots \hat{a}_a^\dagger \cdots \hat{a}_j^\dagger \cdots \hat{a}_b, \quad (2.17)$$

where σ is the number of two-state permutations required to do the normal ordering.

2.4 Wick's Theorem

At this point, the many-body problem has been reduced to computing long strings of creation and annihilation operators between the normal-ordered Hamiltonian and the correlated wave function using Eq. (2.8). Instead of using a brute-force approach by permuting over and over, a further simplification known as *Wick's theorem* [91] can be introduced. A Wick contraction of two operators with respect to the reference state is defined as

$$\overline{\hat{A}\hat{B}} = \hat{A}\hat{B} - \left\{ \hat{A}\hat{B} \right\}. \quad (2.18)$$

Which, given the definition in Eq. (2.17) and the anticommutation relations int Eq. (2.8), means that the only nonzero contractions are of the form,

$$\overline{\hat{a}_i^\dagger \hat{a}_j} = \delta_{ij} \quad \text{and} \quad \overline{\hat{a}_a \hat{a}_b^\dagger} = \delta_{ab}. \quad (2.19)$$

Because contracted operators simply represent a Kronecker delta, they can be removed from a normal ordered product by permuting the product σ times so that the contracted operators

are next to each other,

$$\{\hat{A} \cdots \hat{B} \cdots \hat{C} \cdots \hat{D}\} = (-1)^\sigma \{\hat{A} \cdots \hat{B} \hat{C} \cdots \hat{D}\} = (-1)^\sigma \hat{B} \hat{C} \{\hat{A} \cdots \hat{D}\}. \quad (2.20)$$

These different definitions for operator manipulation come together to define the time-independent Wick's theorem, which reformulates a product of operators as the sum of its normal-ordered form and all possible contractions of its normal-ordered form,

$$\hat{A} \hat{B} \hat{C} \cdots = \left\{ \hat{A} \hat{B} \hat{C} \cdots \right\} + \sum_{\text{one-contractions}} \left\{ \overbrace{\hat{A} \hat{B} \hat{C} \cdots}^{\square} \right\} + \sum_{\text{two-contractions}} \left\{ \overbrace{\overbrace{\hat{A} \hat{B} \hat{C} \cdots}^{\square}}^{\square} \right\} + \cdots + \sum_{\text{all-contractions}} \left\{ \overbrace{\overbrace{\overbrace{\hat{A} \hat{B} \hat{C} \cdots}^{\square}}^{\square}}^{\square} \right\}. \quad (2.21)$$

Wick's theorem is incredibly useful in many-body techniques because complicated expressions of operators can be expressed as diagrams that are easy to compute with simple diagrammatic rules which correspond to Eqs. (2.8),(2.19), and (2.20). These diagrammatic techniques are an integral component to deriving expressions used in this work, and their underlying rules are extensively discussed in [18].

A powerful application of Wick's theorem is to rewrite the Hamiltonian in Eq. (2.2) as a sum of normal-ordered operators in the form of Eq. (2.21),

$$\hat{H} = E_0 + \sum_{pq} f_q^p \left\{ \hat{a}_p^\dagger \hat{a}_q \right\} + \frac{1}{4} \sum_{pqrs} V_{rs}^{pq} \left\{ \hat{a}_p^\dagger \hat{a}_q^\dagger \hat{a}_s \hat{a}_r \right\} + \frac{1}{36} \sum_{pqrstu} W_{stu}^{pqr} \left\{ \hat{a}_p^\dagger \hat{a}_q^\dagger \hat{a}_r^\dagger \hat{a}_u \hat{a}_t \hat{a}_s \right\} + \cdots. \quad (2.22)$$

This form of the Hamiltonian can be split into a zero-body component E_0 , known as the *reference energy*, and the remaining *normal-ordered Hamiltonian*, \hat{H}_N ,

$$\hat{H}_N = \sum_{pq} f_q^p \left\{ \hat{a}_p^\dagger \hat{a}_q \right\} + \frac{1}{4} \sum_{pqrs} V_{rs}^{pq} \left\{ \hat{a}_p^\dagger \hat{a}_q^\dagger \hat{a}_s \hat{a}_r \right\} + \frac{1}{36} \sum_{pqrstu} W_{stu}^{pqr} \left\{ \hat{a}_p^\dagger \hat{a}_q^\dagger \hat{a}_r^\dagger \hat{a}_u \hat{a}_t \hat{a}_s \right\} + \cdots. \quad (2.23)$$

The reference energy, E_0 , contains fully-contracted terms, and because the Hamiltonian operators are ordered so that the creation operators appear before the annihilations operators, only terms that contract *hole* states in the form $\{\cdots \hat{a}_i^\dagger \cdots \hat{a}_j \cdots\}$ are nonzero. Therefore, the zero-body component of the normal ordered Hamiltonian can be written as a sum over all hole states for each component of the original Hamiltonian,

$$E_0 = \sum_i {}^{(1)}H_i^i + \frac{1}{2} \sum_{ij} {}^{(2)}H_{ij}^{ij} + \frac{1}{6} \sum_{ijk} {}^{(3)}H_{ijk}^{ijk} \dots . \quad (2.24)$$

In a compact diagrammatic form, this sum can be drawn as the sum of connected vertices ($\bullet \cdots \cdots \times$, $\bullet \cdots \cdots \bullet$, etc...) corresponding to the components of the original Hamiltonian in Eq. (2.2),

$$E_0 = \text{Diagram } 1 + \text{Diagram } 2 + \text{Diagram } 3 + \dots . \quad (2.25)$$

The number of lines connected to each vertex defines its type such that the single vertex corresponds to the one-body Hamiltonian, the double vertex corresponds to the two-body Hamiltonian, etc... The looped lines represent a sum over all hole states. The reference energy is also equivalent to the Hamiltonian expectation value for the reference state,

$$E_0 = \langle \Phi_0 | \hat{H} | \Phi_0 \rangle. \quad (2.26)$$

The second component of the normal-ordered Hamiltonian, $f_q^p \left\{ \hat{a}_p^\dagger \hat{a}_q \right\}$, contains terms that have all operators contracted except for one pair. Like the fully-contracted term, these

contractions must involve only hole states,

$$f_q^p = {}^{(1)}H_q^p + \sum_i {}^{(2)}H_{qi}^{pi} + \frac{1}{2} \sum_{ij} {}^{(3)}H_{qij}^{pij} + \dots . \quad (2.27)$$

In diagrammatic notation, the uncontracted pair of operators is represented as two external lines connected to each vertex which, because they are generic states, are drawn as unoriented lines,

$$\text{Diagrammatic equation (2.28)}$$

When a line represents a particle state, it will contain an arrow directed upwards while a line representing a hole state will contain an arrow directed downwards.

The two-body term, $V_{rs}^{pq} \left\{ \hat{a}_p^\dagger \hat{a}_q^\dagger \hat{a}_s \hat{a}_r \right\}$, follows in the same manner such that it represents all terms of the original Hamiltonian with all but two pairs of operators contracted. Like the zero-body and one-body terms, the two-body term contains the original two-body term ${}^{(2)}\hat{H}$ as well as density-dependent terms that sum over hole states in higher-body Hamiltonian terms, leaving four external lines for each diagram vertex,

$$V_{rs}^{pq} = {}^{(2)}H_{rs}^{pq} + \sum_i {}^{(3)}H_{rsi}^{pqi} + \dots$$

$$\text{Diagrammatic equation (2.29)}$$

Three- and four-body normal-ordered terms can also be calculated by following the same

procedure, but in practice are truncated at the two- or three-body level. Because normal ordering the Hamiltonian has the effect of shuffling higher-order interactions into lower-order terms, it becomes feasible to include computationally expensive many-body interactions as normal-ordered few-body interactions. Also, it reorganizes many-body correlations into the reference state so that additional correlations around the Fermi surface can be treated as a perturbation. Therefore, from this point forward, the many-body problem will be formulated in terms of the normal-ordered terms in Eq. (2.22), and the bare interactions will be truncated beyond the three-body level for computational feasibility. Electronic systems are naturally truncated at the level of the two-body Coulomb interaction, while nuclear systems can be successfully described with the two-body normal-ordered piece of the three-body force, in the form of Eq. (2.29).

With this new partition, the many-body Schrödinger equation for the ground state $|\Psi\rangle$ can be written in terms of the normal-ordered Hamiltonian as,

$$\begin{aligned} \hat{H}|\Psi\rangle &= (E_0 + \hat{H}_N)|\Psi\rangle = E|\Psi\rangle \\ \longrightarrow \quad \hat{H}_N|\Psi\rangle &= (E - E_0)|\Psi\rangle = \Delta E|\Psi\rangle, \end{aligned} \tag{2.30}$$

where ΔE is known as the *correlation energy*.

Now that the many-body quantum problem has been formulated, different approaches to solving that problem can be proposed and analyzed. Because taking account of correlations from all particles simultaneously is a demanding—and for some systems, computationally impossible—endeavor, methods for solving the many-body Schrödinger equation should be systematically improvable. Successful methods with this quality incorporate the most dominant correlations in lower-order solutions and approach the exact solution when more and

more orders are included.

2.5 Hartree–Fock Method

A successful, first-order approximation to any many-body method comes from noticing that each individual particle feels a mean-field potential from the cumulative interactions with all the other particles. The *Hartree-Fock* (HF) method [92, 93] aims to transform the original single-particle basis to a Hartree-Fock basis where each orbital is the eigenfunction of its corresponding mean-field. Because the transformation of a single orbital changes its effect on every other particle, this process must be performed iteratively until self-consistency between all the orbitals is reached, which is why this method is also known as the *Self-Consistent Field* (SCF) method.

This mean-field picture results from the following procedure. It begins by minimizing the reference energy with respect to the reference state. This functional is just the zero-body piece of the normal-ordered Hamiltonian,

$$E_{\text{HF}} [\Phi_0] = \langle \Phi_0 | \hat{H} | \Phi_0 \rangle = \sum_i {}^{(1)}H_i^i + \frac{1}{2} \sum_{ij} {}^{(2)}H_{ij}^{ij} + \frac{1}{6} \sum_{ijk} {}^{(3)}H_{ijk}^{ijk}. \quad (2.31)$$

Transforming the reference determinant can be accomplished by rotating the state within the single-particle basis by use of the *Thouless theorem* [94], which states that any Slater determinant can be written as the product of any other Slater determinant and an exponentiated single-excitation operator,

$$|\Phi'\rangle = e^{\hat{C}_1} |\Phi_0\rangle, \quad \text{where } \hat{C}_1 = \sum_{ai} C_i^a \left\{ \hat{a}_a^\dagger \hat{a}_i \right\}. \quad (2.32)$$

If the difference between the two Slater determinants is dominated by single excitations, this transformation can be approximated by expanding the exponential and ignoring higher-order terms,

$$|\Phi'\rangle \simeq \left(1 + \sum_{ai} C_i^a \left\{ \hat{a}_a^\dagger \hat{a}_i \right\} \right) |\Phi_0\rangle. \quad (2.33)$$

The reference energy functional can now be written as a sum of the original reference state and new terms that incorporate the single-excitation variation,

$$E_{\text{HF}} [\Phi'] = \langle \Phi' | \hat{H} | \Phi' \rangle \simeq E_{\text{HF}} [\Phi_0] + \sum_{ai} C_i^a \langle \Phi_0 | \hat{H} | \Phi_i^a \rangle + \sum_{ai} C_i^{a*} \langle \Phi_i^a | \hat{H} | \Phi_0 \rangle. \quad (2.34)$$

The minimum of this functional is found by differentiating the expression with respect to the coefficients C_i^a and setting the result to zero,

$$\delta E_{\text{HF}} [\Phi'] \simeq \sum_{ai} \delta C_i^a \langle \Phi_0 | \hat{H} | \Phi_i^a \rangle + \sum_{ai} \delta C_i^{a*} \langle \Phi_i^a | \hat{H} | \Phi_0 \rangle = 0. \quad (2.35)$$

Because this expression is Hermitian, both terms must vanish independently so that,

$$\langle \Phi_0 | \hat{H} | \Phi_i^a \rangle = \langle \Phi_i^a | \hat{H} | \Phi_0 \rangle = 0. \quad (2.36)$$

This condition is the result of the *Brillouin theorem* [95], which states that the Hamiltonian matrix element must vanish between an optimized Hartree-Fock ground state and any single excitation from it. The Brillouin condition is satisfied by diagonalizing the one-body piece of the normal-ordered Hamiltonian f_q^p (Eq. (2.27)), known as the *Fock* operator, such that off-diagonal pieces like $\langle \Phi_0 | \hat{H} | \Phi_i^a \rangle = f_a^i$ and $\langle \Phi_i^a | \hat{H} | \Phi_0 \rangle = f_i^a$ vanish. Diagonalizing the Fock

operator can be written schematically as,

$$\varepsilon_q^p \delta_{pq} \leftarrow (1)H_q^p + \sum_i (2)H_{qi}^{pi} + \frac{1}{2} \sum_{ij} (3)H_{qij}^{pij}$$
(2.37)

where ε_q^p is the eigenvalue of the Fock operator, and its diagrammatic form vanishes when the external indices differ.

A practical way of solving this system of equations is to express each new orbital in the unknown Hartree-Fock basis, $|p'\rangle \equiv \phi_{p'}(\mathbf{r})$, denoted with primed labels, as a linear combination of the known single-particle basis states, $|p\rangle \equiv \phi_p(\mathbf{r})$, denoted without primed labels. These two bases are related by a unitary transformation $C_{p'}^p \equiv \langle p|p'\rangle$,

$$|p'\rangle = \sum_p \langle p|p'\rangle |p\rangle = \sum_p C_{p'}^p |p\rangle. \quad (2.38)$$

Then the Fock matrix can be written in terms of the Hartree-Fock basis,

$$\begin{aligned} f_{q'}^{p'} &= (1)H_{q'}^{p'} + \sum_{i'} (2)H_{q'i'}^{p'i'} + \frac{1}{2} \sum_{i'j'} (3)H_{q'i'j'}^{p'i'j'} \\ &= \sum_{pq} C_p^{p'*} (1)H_q^p C_{q'}^q + \sum_{\substack{i' \\ prqs}} C_p^{p'*} C_r^{i'*} (2)H_{qs}^{pr} C_{q'}^q C_{i'}^s + \frac{1}{2} \sum_{\substack{i'j' \\ prsqtu}} C_p^{p'*} C_r^{i'*} C_s^{j'*} (3)H_{qtu}^{prs} C_{q'}^q C_{i'}^t C_{j'}^u. \end{aligned} \quad (2.39)$$

Defining the first-order density matrix γ_q^p as the product of expansion coefficients, summed

over all shared hole states,

$$\gamma_q^p = \sum_{i'} C_{i'}^p C_q^{i'*}, \quad (2.40)$$

Eq. (2.38) is simplified to,

$$f_{q'}^{p'} = \sum_{pq} C_p^{p'*} \left[{}^{(1)}H_q^p + \sum_{rs} \gamma_s^r {}^{(2)}H_{qs}^{pr} + \frac{1}{2} \sum_{rstu} \gamma_t^r \gamma_u^s {}^{(3)}H_{qtu}^{prs} \right] C_{q'}^q \rightarrow \varepsilon_{q'}^{p'} \delta_{p'q'}. \quad (2.41)$$

Therefore, the Hartree-Fock equations are ultimately expressed as an eigenvalue problem according to Eq. (2.5) where the matrix to diagonalize is the Fock matrix in the form,

$$\hat{F}_q^p (\hat{C}) = {}^{(1)}H_q^p + \sum_{rs} \gamma_r^s {}^{(2)}H_{qs}^{pr} + \frac{1}{2} \sum_{rstu} \gamma_r^t \gamma_s^u {}^{(3)}H_{qtu}^{prs}, \quad (2.42)$$

and the matrix of coefficients, $\hat{C} = C_{p'}^p$, is the unitary operator that transforms the matrix to a diagonal form,

$$\sum_{pq} C_p^{p'*} F_q^p (\hat{C}) C_{q'}^q = \varepsilon_{q'}^{p'} \delta_{p'q'} \quad (2.43)$$

The iterative nature of the solution comes from the dependence of the Fock matrix on the transformation coefficients. These Hartree-Fock equations are solved numerically by using an iterative algorithm where the Fock matrix is built using a known set of coefficients and diagonalized to obtain an updated set of coefficients. This process is repeated until the unitary set of coefficients is unchanged within a certain tolerance. For most calculations, using the identity matrix as an initial guess for the coefficients is sufficient. To improve the rate of convergence, techniques such as the direct inversion of the iterative subspace (DIIS) [96, 97] or Broyden's method [98] can be implemented. And, to avoid any oscillatory behavior around the solution, techniques such as the level-shifting method or *ad hoc* linear mixing can be implemented to dampen the large changes between iterations.

To make use of the HF solution as the reference state for post-HF calculations, the Hamiltonian matrix elements must be transformed to the new basis and the normal-ordered pieces redefined to account for the additional reordering of one-particle correlations into the HF energy. The one-body piece from Eq. (2.27) is simply the resulting eigenvalues of the diagonalized Fock matrix,

$$f_{q'}^{p'} = \varepsilon_{q'}^{p'} \delta_{p'q'}. \quad (2.44)$$

For the two-body term, Eq. (2.29), first the density-dependent component of the three-body interaction is written with the first-order density matrix. Then the remaining states are transformed according to Eq. (2.38),

$$V_{r's'}^{p'q'} = \sum_{pqrs} C_p^{p'*} C_q^{q'*} \left({}^{(2)}H_{rs}^{pq} + {}^{(3)}H_{rsu}^{pqt} \gamma_t^u \right) C_{r'}^r C_{s'}^s. \quad (2.45)$$

The reference energy from Eqns. (2.24) and (2.26) can be written in terms of the transformed one- and two-body Hamiltonian, Eqns. (2.27) and (2.29), and the original three-body term using first-order density matrices,

$$E_0 = \sum_{i'} \varepsilon_{i'}^{i'} - \frac{1}{2} \sum_{i'j'} V_{i'j'}^{i'j'} + \frac{1}{6} \sum_{pqrsu} {}^{(3)}H_{stu}^{pqr} \gamma_p^s \gamma_q^t \gamma_u^r. \quad (2.46)$$

Additionally, any operators that are constructed in the original basis must be transformed in a similar manner. For example, a one-body operator \hat{O} in the Hartree-Fock basis is,

$$\begin{aligned} \hat{O} &= \sum_{p'q'} O_{q'}^{p'} \left\{ \hat{a}_{p'}^\dagger \hat{a}_{q'} \right\} = \sum_{p'q'pq} C_p^{p'*} O_q^p C_{q'}^q \left\{ \hat{a}_{p'}^\dagger \hat{a}_{q'} \right\} \\ &\longrightarrow O_{q'}^{p'} = \sum_{pq} C_p^{p'*} O_q^p C_{q'}^q. \end{aligned} \quad (2.47)$$

Because the Hartree-Fock basis is diagonal in the one-body piece of the Hamiltonian, any terms that include off-diagonal elements automatically vanish, greatly simplifying any post-Hartree-Fock methods. From this point on, all calculations will use the Hartree-Fock basis unless stated otherwise, and prime symbols will be omitted.

2.6 Configuration-Interaction

The most generic way to write a correlated wave function in a given basis is as a linear combination of all possible Slater determinants. This expansion can, in principle, consist of the 0p-0h reference state and all possible $Np-Nh$ excitations up to $Ap-Ah$ excitations,

$$|\Psi_\nu\rangle = \sum_{\nu_i}^N C_{\nu_i} |\Phi_{\nu_i}\rangle = C_0 |\Phi_0\rangle + \sum_{N=1}^A \left(\frac{1}{N!}\right)^2 \sum_{\substack{a_1 \dots a_N \\ i_1 \dots i_N}} C_{i_1 \dots i_N}^{a_1 \dots a_N} |\Phi_{i_1 \dots i_N}^{a_1 \dots a_N}\rangle. \quad (2.48)$$

Using this form of the wave function in Eq. (2.48), the normal-ordered Schrödinger equation can be reformulated as a standard matrix eigenvalue problem,

$$\begin{aligned} \hat{H}_N |\Psi_\nu\rangle &= \Delta E_\nu |\Psi_\nu\rangle \quad \longrightarrow \quad \langle \Psi_\mu | \hat{H}_N | \Psi_\nu \rangle = \Delta E_\nu \langle \Psi_\mu | \Psi_\nu \rangle \\ &= \sum_{\mu_i \nu_i} C_{\mu_i}^* \langle \Phi_{\mu_i} | \hat{H}_N | \Phi_{\nu_i} \rangle C_{\nu_i} = \Delta E_\nu \sum_{\mu_i \nu_i} C_{\mu_i}^* C_{\nu_i} \delta_{\mu_i \nu_i} \\ &\longrightarrow \mathbf{C}_\mu^T \left(\langle \Phi_{\mu_i} | \hat{H}_N | \Phi_{\nu_i} \rangle - \Delta E_\nu \mathbf{I} \right) \mathbf{C}_\nu = 0. \end{aligned} \quad (2.49)$$

In this case, the matrix elements are Hamiltonian terms that connect two Slater determinants, and the eigenvectors are the ground and excited states in the form of Eq. (2.48). The matrix elements can be found with the help of the Slater-Condon rules [89, 99] which, because the Hamiltonian is restricted to one- and two-body terms, require that any terms

connecting Slater determinants which differ by more than two single-particle states vanish. Also, because the one-body Hamiltonian is diagonal in the Hartree-Fock basis, it only contributes to diagonal elements of the CI matrix. Some examples of these matrix elements are,

$$\begin{aligned}\langle \Phi_i^a | \hat{H} | \Phi_i^a \rangle &= \varepsilon_a - \varepsilon_i - V_{ia}^{ia}, \\ \langle \Phi_{ij}^{ab} | \hat{H} | \Phi_{ij}^{cd} \rangle &= V_{cd}^{ab}, \\ \langle \Phi_{ijk}^{abc} | \hat{H} | \Phi_{ijl}^{abd} \rangle &= -V_{kd}^{lc}.\end{aligned}\tag{2.50}$$

Because the configuration-interaction method exhaustively captures all the correlations of a many-body system, it is considered an “exact” method within a certain model space and becomes truly exact as the number of single-particle states is increased to infinity. However, there is a price to pay for this exactness. The number of Slater determinants in a certain model space, \mathcal{N} , scales factorially according to Eq. (2.5) and the configuration-interaction matrix scales as \mathcal{N}^2 . For sufficiently-sized model spaces, the memory required for this matrix quickly becomes unmanagable even for the largest supercomputers, see Fig. 2.3.

However, for a reference state that is a good approximation to the true ground state, few-body excitations generally dominate the wave functions for low-lying states [100]. This can be exploited by truncating the expansion in Eq. (2.48). Owing to the two-body nature of the interaction, the lowest appropriate truncation is also at the two-body level, known as configuration interaction with singles and doubles (CISD),

$$|\Psi_\nu\rangle = C_0 |\Phi_0\rangle + \sum_{ai} C_i^a |\Phi_i^a\rangle + \frac{1}{4} \sum_{abij} C_{ij}^{ab} |\Phi_{ij}^{ab}\rangle.\tag{2.51}$$

This is a very straightforward and tractable way to approximate the many-body Schrödinger

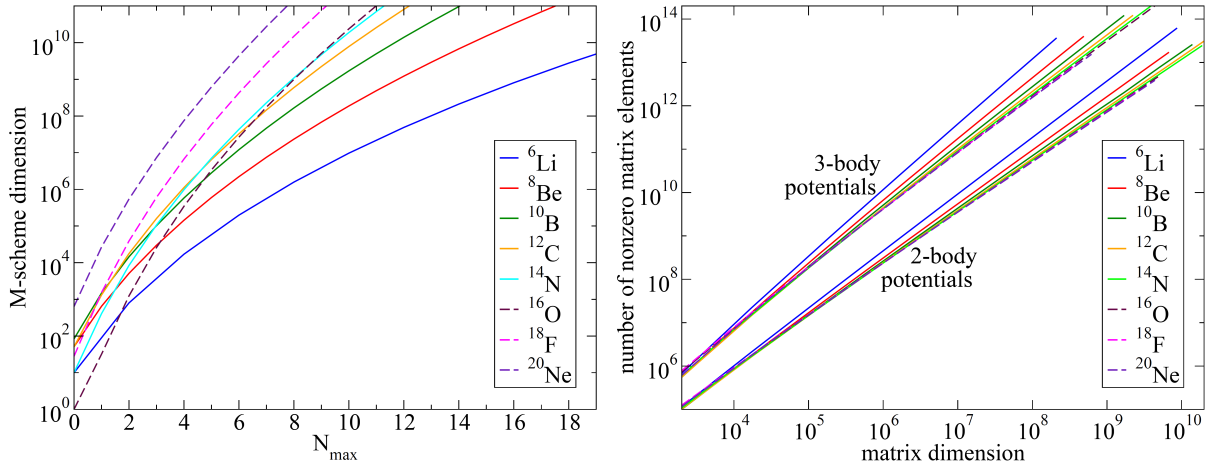


Figure 2.3: Scaling of the matrix size and number of non-zero matrix elements for nuclear CI calculations of light nuclei. Even for modestly-sized model spaces, the memory requirements approach the limit of petascale supercomputers ($\sim 10^{10}$). Figure taken from [2].

equation, and it can be systematically improved by adding more excitations such as triples (CISDT) or triples and quadruples (CISDTQ). But the drawback to this simplicity is that any truncated CI method is not size-extensive such that any extensive property of a system, like the energy, would scale with the size of the system. A desirable many-body method will be both systematically improvable and size-extensive while maintaining computational feasibility.

2.7 Many-Body Perturbation Theory

One many-body method that is both size-extensive and systematically improvable treats particle-particle interactions as a perturbation to the mean-field potential and is known as many-body perturbation theory (MBPT) [101, 15, 16, 18]. The Hamiltonian is partitioned

into a diagonal piece and the interaction piece,

$$\begin{aligned}\hat{H} &= \hat{H}_0 + \hat{V}, \quad \text{with} \\ \hat{H}_0 &= E_0 + \sum_p f_p^p \left\{ \hat{a}_p^\dagger \hat{a}_p \right\} \quad \text{and} \\ \hat{V} &= \frac{1}{4} \sum_{pqrs} V_{pqrs}^{pq} \left\{ \hat{a}_p^\dagger \hat{a}_q^\dagger \hat{a}_s \hat{a}_r \right\}.\end{aligned}\tag{2.52}$$

When not in the Hartree-Fock basis, the interaction piece has the additional off-diagonal Fock term, $\sum_{p \neq q} f_q^p \left\{ \hat{a}_p^\dagger \hat{a}_q \right\}$. This means that the reference state is an eigenstate of the zero-order piece of the Hamiltonian,

$$\hat{H}_0 |\Phi_0\rangle = \left(E_0 + \sum_i f_i^i \left\{ \hat{a}_i^\dagger \hat{a}_i \right\} \right) |\Phi_0\rangle = \left(E_0 + \sum_i \varepsilon_i \right) |\Phi_0\rangle = E_0^{(0)} |\Phi_0\rangle.\tag{2.53}$$

Using *intermediate normalization*, which sets $\langle \Phi_0 | \Psi \rangle = 1$, the Schrödinger equation, Eq. (2.1) for the ground state becomes,

$$\begin{aligned}\langle \Phi_0 | (\hat{H}_0 + \hat{V}) | \Psi \rangle &= \langle \Phi_0 | \hat{H}_0 | \Psi \rangle + \langle \Phi_0 | \hat{V} | \Psi \rangle = E \langle \Phi | \Psi \rangle \\ &= E^{(0)} \langle \Phi | \Psi \rangle + \langle \Phi_0 | \hat{V} | \Psi \rangle = E^{(0)} + \Delta E_0 = E,\end{aligned}\tag{2.54}$$

where the energy difference is $\Delta E_0 \equiv \langle \Phi_0 | \hat{V} | \Psi \rangle$.

Next, the projection operators \hat{P} and \hat{Q} can be introduced,

$$\hat{P} = |\Phi_0\rangle\langle\Phi_0|,\tag{2.55}$$

$$\hat{Q} = \sum_{n \neq 0} |\Phi_n\rangle\langle\Phi_n| = 1 - |\Phi_0\rangle\langle\Phi_0|.\tag{2.56}$$

The \hat{P} operator isolates the reference-state component of any Slater determinant while the

\hat{Q} operator isolates all components *except* the reference-state component out of any Slater determinant. Both these operators are idempotent, which means that $\hat{P}^2 = \hat{P}$ and $\hat{Q}^2 = \hat{Q}$, and because of intermediate normalization, the correlated wave function can be written as $|\Psi\rangle = (\hat{P} + \hat{Q})|\Psi\rangle = |\Phi\rangle + \hat{Q}|\Psi\rangle$. Also, both operators commute with the unperturbed part of the Hamiltonian, $\hat{H}_0\hat{P} = \hat{P}\hat{H}_0$ and $\hat{H}_0\hat{Q} = \hat{Q}\hat{H}_0$. These identities can be applied to an alternate version of the Schrödinger equation which defines a particular version of perturbation theory known as Raleigh-Schrödinger perturbation theory (RSPT) [102, 103]. In this version, the zeroth-order energy $E^{(0)}$ is added to both sides of the Schrödinger equation. Acting with \hat{Q} and rearranging terms gives,

$$\begin{aligned}\hat{Q}(E^{(0)} - \hat{H}_0)|\Psi\rangle &= \hat{Q}(E^{(0)} + \hat{V} - E)|\Psi\rangle \\ \hat{Q}(E^{(0)} - \hat{H}_0)\hat{Q}|\Psi\rangle &= \hat{Q}(\hat{V} - \Delta E_0)|\Psi\rangle,\end{aligned}\tag{2.57}$$

where $\Delta E_0 \equiv E - E^{(0)} = \langle\Phi_0|\hat{V}|\Psi\rangle$. The operator $\hat{Q}(E^{(0)} - \hat{H}_0)\hat{Q}$ is invertible because $(E^{(0)} - \hat{H}_0)^{-1}$ is never singular in Q -space. Therefore, the operator $\hat{R}_0 = \hat{Q}(E^{(0)} - \hat{H}_0)^{-1}\hat{Q}$, known as the *resolvent*, can be applied to both sides which gives,

$$\hat{Q}|\Psi\rangle = \hat{R}_0(\hat{V} - \Delta E_0)|\Psi\rangle.\tag{2.58}$$

The left-hand side of this equation can be rewritten as $\hat{Q}|\Psi\rangle = |\Psi\rangle - |\Phi_0\rangle$ to result in the generating equation for RSPT,

$$|\Psi\rangle = |\Phi\rangle + \hat{R}_0(\hat{V} - \Delta E_0)|\Psi\rangle.\tag{2.59}$$

Because the single-particle states are eigenfunctions of the zeroth-order Hamiltonian, they

are also eigenfunctions of the resolvent, with the resulting eigenvalues, ε , are known as *energy denominators*. Applying the resolvent operator to any state orthogonal to the reference state, see Eqs. (2.13) - (2.16), gives the following relation,

$$\hat{R}_0 |\Phi_{i_1 \dots i_N}^{a_1 \dots a_N}\rangle = \frac{1}{\varepsilon_{i_1 \dots i_N}^{a_1 \dots a_N}} |\Phi_{i_1 \dots i_N}^{a_1 \dots a_N}\rangle, \text{ where}$$

$$\varepsilon_{i_1 \dots i_N}^{a_1 \dots a_N} = \varepsilon_{i_1} + \dots + \varepsilon_{i_N} - \varepsilon_{a_1} - \dots - \varepsilon_{a_N}. \quad (2.60)$$

Equation (2.59) can be iterated infinitely to give the solution for the fully correlated wave function,

$$|\Psi\rangle = \sum_{n=0}^{\infty} \left[\hat{R}_0 (\hat{V} - \Delta E_0) \right]^n |\Phi_0\rangle. \quad (2.61)$$

Applying this form of the correlated wave function into Eq. (2.54) results in the energy difference,

$$\Delta E_0 = \langle \Phi_0 | \hat{V} | \Psi \rangle = \sum_{n=0}^{\infty} \langle \Phi_0 | \hat{V} \left[\hat{R}_0 (\hat{V} - \Delta E_0) \right]^n | \Phi_0 \rangle \quad (2.62)$$

The immediate problem with these equations is that the right-hand sides contain the target energy difference ΔE_0 for which these equations are meant to solve. This can be remedied by expanding the right-hand sides and rearranging terms. Using the fact that $\hat{R}_0 \Delta E_0 |\Phi_0\rangle = \Delta E_0 \hat{R}_0 |\Phi_0\rangle = 0$, the first-order energy $E^{(1)} = \langle \Phi_0 | \hat{V} | \Phi_0 \rangle$, and the shifted term $\tilde{V} \equiv \hat{V} - E^{(1)}$, these simplify to,

$$|\Psi\rangle - |\Phi_0\rangle = \hat{R}_0 \hat{V} |\Phi_0\rangle + \hat{R}_0 \tilde{V} \hat{R}_0 \hat{V} |\Phi_0\rangle$$

$$+ \hat{R}_0 \tilde{V} \hat{R}_0 \tilde{V} \hat{R}_0 \hat{V} |\Phi_0\rangle - \langle \Phi_0 | \hat{V} \hat{R}_0 \hat{V} | \Phi_0 \rangle \hat{R}_0^2 \hat{V} |\Phi_0\rangle + \dots \quad (2.63)$$

$$\Delta E_0 = \langle \Phi_0 | \hat{V} | \Phi_0 \rangle + \langle \Phi_0 | \hat{V} \hat{R}_0 \hat{V} | \Phi_0 \rangle + \langle \Phi_0 | \hat{V} \hat{R}_0 \tilde{V} \hat{R}_0 \hat{V} | \Phi_0 \rangle$$

$$+ \langle \Phi_0 | \hat{V} \hat{R}_0 \tilde{V} \hat{R}_0 \tilde{V} \hat{R}_0 \hat{V} | \Phi_0 \rangle - \langle \Phi_0 | \hat{V} \hat{R}_0 \hat{V} | \Phi_0 \rangle \langle \Phi_0 | \hat{V} \hat{R}_0^2 \hat{V} | \Phi_0 \rangle + \dots \quad (2.64)$$

The order of each term can be easily identified by counting the numbers of times that \hat{V} or \tilde{V} appears. At the third order in the wave function and the fourth order in the energy, *renormalization* terms make their first appearance. These terms contain separated and closed factors in the form of lower-order energy terms, such as $\langle \Phi_0 | \hat{V} \hat{R}_0 \hat{V} | \Phi_0 \rangle \equiv E^{(2)}$. Terms that do not contain normalization factors are known as *principal* terms.

2.7.1 Factorization Theorem

A powerful application of diagrammatic techniques known as the *factorization theorem* [16, 104, 105] can immediately be used to simplify these expansions. By factoring sums of *unlinked* diagrams, where two or more parts of a diagram are closed and separated, from the principal terms, it can be shown that they exactly cancel with the renormalization terms at each order. In the following factorization, two fourth-order energy diagrams which differ by only the time-ordering of the interaction vertices are added together. By multiplying each term by an appropriate factor so that they share a common denominator, the additive property of the energy denominators ($\varepsilon_{ij}^{ab} + \varepsilon_{kl}^{cd} = \varepsilon_{ijkl}^{abcd}$) can be exploited to remove the addition of both terms, now written as the product of two terms,

$$\begin{aligned} \frac{1}{16} \sum_{\substack{abcd \\ i j k l}} \frac{V_{ab}^{ij} V_{ij}^{ab} V_{cd}^{kl} V_{kl}^{cd}}{\varepsilon_{ij}^{ab} \varepsilon_{ijkl}^{abcd} \varepsilon_{kl}^{cd}} + \frac{1}{16} \sum_{\substack{abcd \\ i j k l}} \frac{V_{ab}^{ij} V_{ij}^{ab} V_{cd}^{kl} V_{kl}^{cd}}{\varepsilon_{ij}^{ab} \varepsilon_{ijkl}^{abcd} \varepsilon_{ij}^{ab}} &= \frac{1}{16} \sum_{\substack{abcd \\ i j k l}} V_{ab}^{ij} V_{ij}^{ab} V_{cd}^{kl} V_{kl}^{cd} \frac{\varepsilon_{ij}^{ab} + \varepsilon_{kl}^{cd}}{\left(\varepsilon_{ij}^{ab}\right)^2 \varepsilon_{ijkl}^{abcd} \varepsilon_{kl}^{cd}} \\ &= \frac{1}{4} \sum_{\substack{abij}} \frac{V_{ab}^{ij} V_{ij}^{ab}}{\left(\varepsilon_{ij}^{ab}\right)^2} \cdot \frac{1}{4} \sum_{\substack{cdkl}} \frac{V_{cd}^{kl} V_{kl}^{cd}}{\varepsilon_{kl}^{cd}} = \langle \Psi_n^{(1)} | \Psi_n^{(1)} \rangle E_n^{(2)}. \end{aligned} \quad (2.65)$$

In diagrammatic form, these sums are represented by internal lines between vertices. The common resolvent in each term, drawn as a line through the relevant state, is removed, and

the common diagrams which result are shown as a product (see [18] for more details),

$$\begin{array}{c} R_0 \\ \hline R_0 \\ \hline R_0 \end{array} +
 \begin{array}{c} R_0 \\ \hline R_0 \\ \hline R_0 \end{array} =
 \begin{array}{c} R_0 \\ \hline R_0 \\ \hline R_0 \end{array}. \quad (2.66)$$

A similar factorization can be performed on the wave function terms. The following example uses two similar third-order terms with different time-ordered interaction vertices. Once again, the additive property of the energy denominators is used to factor the common denominator between the terms, resulting in the product of two lower-order terms,

$$\begin{aligned}
 \frac{1}{16} \sum_{\substack{abcd \\ i j k l}} \frac{V_{ij}^{ab} V_{cd}^{kl} V_{kl}^{cd}}{\varepsilon_{cd}^{kl} \varepsilon_{ijkl}^{ab} \varepsilon_{ij}^{ab}} |\Phi_{ij}^{ab}\rangle + \frac{1}{16} \sum_{\substack{abcd \\ i j k l}} \frac{V_{ij}^{ab} V_{cd}^{kl} V_{kl}^{cd}}{\varepsilon_{ij}^{ab} \varepsilon_{ijkl}^{ab} \varepsilon_{ij}^{ab}} |\Phi_{ij}^{ab}\rangle &= \frac{1}{16} \sum_{\substack{abcd \\ i j k l}} V_{ij}^{ab} V_{cd}^{kl} V_{kl}^{cd} \frac{\varepsilon_{ij}^{ab} + \varepsilon_{kl}^{cd}}{\left(\varepsilon_{ij}^{ab}\right)^2 \varepsilon_{ijkl}^{ab} \varepsilon_{kl}^{cd}} |\Phi_{ij}^{ab}\rangle \\
 &= \frac{1}{4} \sum_{\substack{abij \\ cdkl}} \frac{V_{ij}^{ab}}{\left(\varepsilon_{ij}^{ab}\right)^2} |\Phi_{ij}^{ab}\rangle \cdot \frac{1}{4} \sum_{\substack{cdkl \\ cdkl}} \frac{V_{cd}^{kl} V_{kl}^{cd}}{\varepsilon_{kl}^{cd}} = \frac{|\Psi_n^{(1)}\rangle}{\varepsilon_n} E_n^{(2)}
 \end{aligned}$$

The factorization theorem is also valid with off-diagonal Fock terms and applies to the MBPT expansions of both the wave function and energy. Therefore, the MBPT expansions in Eqs. (2.61) and (2.62) can be written in terms of *linked diagrams* only [7],

$$|\Psi\rangle = \sum_{n=0}^{\infty} \left[\hat{R}_0 (\hat{V} - \Delta E_0) \right]^n |\Phi_0\rangle_L, \quad (2.68)$$

$$\Delta E_0 = \sum_{n=0}^{\infty} \langle \Phi_0 | \hat{V} \left[\hat{R}_0 (\hat{V} - \Delta E_0) \right]^n | \Phi_0 \rangle_L, \quad (2.69)$$

where “L” denotes that no diagrams with closed, disconnected pieces should be included. This result not only simplifies the MBPT expressions, but it guarantees the size-extensivity of the MBPT wave function at each order [18]. Also, it is a useful step towards coupled-cluster theory which reorganizes the connected diagrams from MBPT such that certain classes can be summed to infinite order, see section 3.2.

Chapter 3

Coupled-Cluster Theory

Coupled-cluster theory is a powerful method for approximating solutions to the many-body Schrödinger equation. Because of its effectiveness and economical scaling it has been a staple of many-body quantum mechanics for decades. This chapter details various aspects of the coupled-cluster approach and presents ground-state results for multiple systems. First, the CC wave operator and the corresponding effective Hamiltonian will be introduced and used to derive the CC equations. Then, results from MBPT are used to illuminate the underlying many-body physics of the CC wave function. After the mathematical foundations of coupled cluster theory are outlined, specific implementation details are discussed and demonstrated by focusing on two simple examples. Finally, the nuclear many-body problem is formally introduced, along with a brief description of the nuclear interactions used in this work, and selected results are shown.

3.1 Exponential Ansatz

Coupled cluster theory is based on expressing the A -particle correlated wave function $|\Psi\rangle$ using the exponential ansatz [9, 19, 15, 16],

$$|\Psi\rangle = e^{\hat{T}} |\Phi_0\rangle. \quad (3.1)$$

The cluster operator $\hat{T} \equiv \hat{T}_1 + \hat{T}_2 + \cdots + \hat{T}_A$, is composed of k -particle k -hole excitation operators, \hat{T}_k , which have the form,

$$\begin{aligned}\hat{T}_1 &\equiv \sum_{ai} t_i^a \left\{ \hat{a}_a^\dagger \hat{a}_i \right\}, \\ \hat{T}_2 &\equiv \frac{1}{4} \sum_{abij} t_{ij}^{ab} \left\{ \hat{a}_a^\dagger \hat{a}_b^\dagger \hat{a}_j \hat{a}_i \right\}, \\ &\vdots \\ \hat{T}_k &\equiv \left(\frac{1}{k!} \right)^2 \sum_{\substack{a_1 \dots a_k \\ i_1 \dots i_k}} t_{i_1 \dots i_k}^{a_1 \dots a_k} \left\{ \hat{a}_{a_1}^\dagger \dots \hat{a}_{a_k}^\dagger \hat{a}_{i_k} \dots \hat{a}_{i_1} \right\},\end{aligned}\tag{3.2}$$

where the unknown matrix elements, $t_{i_1 \dots i_k}^{a_1 \dots a_k}$, are known as *cluster amplitudes* [18].

Using the CC ansatz, the Schrödinger equation can be rewritten by left-multiplying with $\langle \Phi_0 | e^{-\hat{T}}$ as,

$$\begin{aligned}\hat{H} e^{\hat{T}} |\Phi_0\rangle &= E e^{\hat{T}} |\Phi_0\rangle \\ \longrightarrow \quad \langle \Phi_0 | \bar{H} |\Phi_0\rangle &= E,\end{aligned}\tag{3.3}$$

where the *coupled cluster effective Hamiltonian* is defined as,

$$\bar{H} \equiv e^{-\hat{T}} \hat{H} e^{\hat{T}},\tag{3.4}$$

in which the wave operator, $e^{\hat{T}}$, acts as a similarity transform on the Hamiltonian. Using the normal-ordered Hamiltonian \bar{H}_N and the correlation energy ΔE from Eq. (2.4), this can

rewritten as,

$$\begin{aligned} \hat{H}_N e^{\hat{T}} |\Phi_0\rangle &= \Delta E e^{\hat{T}} |\Phi_0\rangle \\ \longrightarrow \quad \langle \Phi_0 | \bar{H}_N |\Phi_0\rangle &= \Delta E, \end{aligned} \quad (3.5)$$

where the *normal-ordered effective Hamiltonian* is constructed equivalently to Eq. (3.6),

$$\bar{H}_N \equiv e^{-\hat{T}} \hat{H}_N e^{\hat{T}}. \quad (3.6)$$

An important characteristic of the effective Hamiltonian, \bar{H} and \bar{H}_N , is that because the cluster operator, which contains no de-excitations, is not Hermitian, the exponential wave operator cannot be unitary, and thus \bar{H} is not Hermitian. This initially seems like an explicit contradiction to any standard quantum mechanics formulation where observables are associated with the real eigenvalues of Hermitian matrices. Technically, the existence and reality of the CC solution is only guaranteed when the full cluster operator is used $\hat{T} = \hat{T}_1 + \cdots + \hat{T}_A$, see [106, 107, 108, 109]. However, while the non-Hermiticity does require some special considerations which will be discussed, this fundamental problem does not materialize in this work.

The effective Hamiltonian in Eq. (3.6) can be rewritten with commutators ($[\hat{A}, \hat{B}] = \hat{A}\hat{B} - \hat{B}\hat{A}$) according to the Baker–Campbell–Hausdorff expansion as,

$$\bar{H} = \hat{H} + [\hat{H}, \hat{T}] + \frac{1}{2!}[[\hat{H}, \hat{T}], \hat{T}] + \frac{1}{3!}[[[\hat{H}, \hat{T}], \hat{T}], \hat{T}] + \frac{1}{4!}[[[[\hat{H}, \hat{T}], \hat{T}], \hat{T}], \hat{T}] + \cdots, \quad (3.7)$$

which terminates at four-nested commutators when using a two-body interaction. This commutator expression ensures that CC theory is size-extensive and contains only connected

terms. In addition, because \hat{T} is an excitation operator, terms of the form $\hat{T}\hat{H}$ are necessarily disconnected and thus vanish [18]. Therefore the CC effective Hamiltonian can be further reduced to

$$\bar{H} = \left(\hat{H} e^{\hat{T}} \right)_c, \quad (3.8)$$

where the subscript “c” indicates that only connected terms are used.

3.1.1 The Coupled Cluster Equations

In practice, the cluster operator \hat{T} must be truncated for calculations to be computationally feasible. In this work, we use only single and double excitations where applicable,

$$\hat{T} = \hat{T}_1 + \hat{T}_2.$$

This is known as coupled cluster with singles and doubles (CCSD), with an asymptotic computational cost that scales like $\mathcal{O}(n_p^4 n_h^2)$, where n_h is the number of hole states and n_p is the number of particle states. This truncation has been successfully applied to many problems in quantum chemistry [110] and nuclear physics [49, 111].

The unknown cluster amplitudes in CCSD, t_i^a and t_{ij}^{ab} , can be calculated by left-multiplying Eq. (3.1) with $\langle \Phi_i^a | e^{-\hat{T}}$ and with $\langle \Phi_{ij}^{ab} | e^{-\hat{T}}$, respectively,

$$\begin{aligned} \langle \Phi_i^a | \bar{H} | \Phi_0 \rangle &= 0, \\ \langle \Phi_{ij}^{ab} | \bar{H} | \Phi_0 \rangle &= 0. \end{aligned} \quad (3.9)$$

After the Fock matrix has been diagonalized, the diagonal components of Eq. (3.9) can be

separated and, after expanding the exponent in Eq. (3.8), the non-vanishing terms of the CCSD amplitude equations in the HF basis become,

$$\langle \Phi_i^a | \left[\hat{H}_2 \left(\hat{T}_1 + \hat{T}_2 + \hat{T}_1 \hat{T}_2 + \frac{1}{2!} \hat{T}_1^2 + \frac{1}{3!} \hat{T}_1^3 \right) \right]_c | \Phi_0 \rangle = \varepsilon_i^a t_i^a \quad (3.10)$$

$$\langle \Phi_{ij}^{ab} | \left[\hat{H}_2 \left(1 + \hat{T}_1 + \hat{T}_2 + \frac{1}{2} \hat{T}_1^2 + \hat{T}_1 \hat{T}_2 + \frac{1}{2!} \hat{T}_2^2 + \frac{1}{3!} \hat{T}_1^3 + \frac{1}{2!} \hat{T}_1^2 \hat{T}_2 + \frac{1}{4!} \hat{T}_1^4 \right) \right]_c | \Phi_0 \rangle = \varepsilon_{ij}^{ab} t_{ij}^{ab},$$

where ε are equivalent to the MBPT energy denominators from Eq. (2.7).

These non-linear equations are solved using an iterative procedure where the cluster amplitudes on the right-hand side of Eq. (3.9) and Eq. (3.10) are updated by calculating the terms on the left-hand side until a fixed point is reached. Like the HF iterative procedure, employing convergence acceleration techniques can reduce the number of CC iterations required. Detailed techniques for solving these equations are discussed in section 3.4.

3.2 Linked-Cluster Theorem and MBPT

The exponential ansatz in Eq. (3.1) and the cluster amplitudes in Eq. (3.1) are not just useful mathematical constructs for solving the many-body problem. They represent physical many-body dynamics and can be derived from the results of many-body perturbation theory, see section 2.7. The *linked-cluster theorem* [16, 104, 105] states that the sum of all time orderings of a disconnected diagram is equal to the product of the two subdiagrams. Using the results and techniques from the factorization theorem, 2.7.1, the linked-cluster theorem can be used to factorize specific MBPT terms such that they can be analytically summed to infinite order. This infinite summation is the main principle behind coupled cluster theory and can be shown to lead naturally to the exponential ansatz.

The first step in deriving the exponential ansatz is to group all the linked MBPT diagrams

of Eq. (2.68) into classes according to their number of disconnected pieces. The first class, where all the terms are connected, can be defined as the cluster excitation operator \hat{T} , depicted by the vertex type . The connected terms can then be characterized by their excitation type such that \hat{T}_k corresponds to k p- k h excitations.

The \hat{T}_1 operator represents the class of all connected 1p-1h MBPT diagrams, which are determined by the number of particle-hole pairs (or pair of up- and down-lines) at the top of the diagram,

$$\begin{aligned} \hat{T}_1 |\Phi_0\rangle \equiv & \text{Diagram with one V-shaped pair of lines} = (\hat{T}_1^{(1)} + \hat{T}_1^{(2)} + \dots) |\Phi_0\rangle = \text{Diagram with one V-shaped pair of lines} + \text{Diagram with one V-shaped pair of lines and one loop} \\ & + \text{Diagram with one V-shaped pair of lines and one loop} + \text{Diagram with one V-shaped pair of lines and one loop} + \dots, \end{aligned} \quad (3.11)$$

where only first-order $\hat{T}^{(1)}$ and second-order $\hat{T}^{(2)}$ terms are shown while resolvant lines and labels are removed for clarity. The \hat{T}_2 operator similarly represents the class of all connected 2p-2h MBPT diagrams. The first- and second-order terms that belong to this class are,

$$\begin{aligned} \hat{T}_2 |\Phi_0\rangle \equiv & \text{Diagram with two V-shaped pairs of lines} = (\hat{T}_2^{(1)} + \hat{T}_2^{(2)} + \dots) |\Phi_0\rangle = \text{Diagram with two V-shaped pairs of lines} + \text{Diagram with two V-shaped pairs of lines} \\ & + \text{Diagram with two V-shaped pairs of lines} + \text{Diagram with two V-shaped pairs of lines} + \text{Diagram with two V-shaped pairs of lines} + \dots. \end{aligned} \quad (3.12)$$

Additionally, the \hat{T}_3 operator represents the class of all connected 3p-3h MBPT diagrams,

of which there is only two second-order terms,

$$\hat{T}_3 |\Phi_0\rangle \equiv \begin{array}{c} \text{Diagram: } \text{Two vertical lines } \backslash\backslash \text{ and } / / \text{ meeting at a point below a horizontal line } R_0. \end{array} = (\hat{T}_3^{(2)} + \dots) |\Phi_0\rangle = \begin{array}{c} \text{Diagram: } \text{Two vertical lines } \backslash\backslash \text{ and } / / \text{ meeting at a point below a dashed horizontal line } R_0. \end{array} + \begin{array}{c} \text{Diagram: } \text{Two vertical lines } \backslash\backslash \text{ and } / / \text{ meeting at a point above a dashed horizontal line } R_0. \end{array} + \dots \quad (3.13)$$

So far, this is merely a redefinition of the connected class of MBPT diagrams up to all orders and is not particularly useful. But the disconnected diagrams, neglected up to this point, can be recombined using the factorization theorem 2.7.1 to provide a powerful simplification (see [18] for a more thorough derivation).

As an example, the remaining disconnected first- and second-order diagrams can be written as the product of connected diagrams. First, the second-order disconnected diagram from the term $\hat{f}^2 |\Phi_0\rangle$ can be rewritten by adding a duplicate with the left and right subdiagrams exchanged, which doesn't change the value because the state labels are generic. Then, the two disconnected diagrams can be rewritten using the factorization theorem following the example of Eq. (2.7.1),

$$\begin{array}{c} \text{Diagram: } \text{Two vertical lines } \backslash\backslash \text{ and } / / \text{ meeting at a point below a horizontal line } R_0. \text{ The left line has points } a \text{ and } i, \text{ the right line has points } b \text{ and } j. \end{array} = \frac{1}{2} \left(\begin{array}{c} \text{Diagram: } \text{Two vertical lines } \backslash\backslash \text{ and } / / \text{ meeting at a point below a horizontal line } R_0. \text{ The left line has points } a \text{ and } i, \text{ the right line has points } b \text{ and } j. \\ \text{Diagram: } \text{Two vertical lines } \backslash\backslash \text{ and } / / \text{ meeting at a point below a horizontal line } R_0. \text{ The left line has points } b \text{ and } j, \text{ the right line has points } a \text{ and } i. \end{array} \right) = \frac{1}{2} \left(\begin{array}{c} \text{Diagram: } \text{Two vertical lines } \backslash\backslash \text{ and } / / \text{ meeting at a point below a horizontal line } R_0. \text{ The left line has points } a \text{ and } i. \end{array} \right)^2. \quad (3.14)$$

The resulting product involves the first-order component of the \hat{T}_1 operator in Eq. (3.11),

$\hat{T}_1^{(1)}$. Algebraically, this process is written below,

$$\begin{aligned} \sum_{abij} \frac{f_i^a f_j^b}{\varepsilon_{ij}^{ab} \varepsilon_i^a} |\Phi_{ij}^{ab}\rangle &= \frac{1}{2} \sum_{abij} \frac{f_i^a f_j^b}{\varepsilon_{ij}^{ab} \varepsilon_i^a} |\Phi_{ij}^{ab}\rangle + \frac{1}{2} \sum_{abij} \frac{f_i^a f_j^b}{\varepsilon_{ij}^{ab} \varepsilon_j^b} |\Phi_{ij}^{ab}\rangle = \frac{1}{2} \sum_{abij} f_i^a f_j^b \frac{\varepsilon_j^b + \varepsilon_i^a}{\varepsilon_{ij}^{ab} \varepsilon_i^a \varepsilon_j^b} |\Phi_{ij}^{ab}\rangle \\ &= \frac{1}{2} \left(\sum_{ai} \frac{f_i^a}{\varepsilon_i^a} |\Phi_i^a\rangle \right) \left(\sum_{bj} \frac{f_j^b}{\varepsilon_j^b} |\Phi_j^b\rangle \right) = \frac{1}{2} (\hat{T}_1^{(1)})^2. \end{aligned} \quad (3.15)$$

This procedure can be repeated for the single second-order disconnected term from $\hat{V}^2 |\Phi_0\rangle$,

$$\begin{aligned} \text{Diagram: } &\text{A Feynman diagram showing two horizontal lines labeled } R_0. \text{ The left line has vertices } a \text{ and } b \text{ with internal lines } i \text{ and } j \text{ connecting them. The right line has vertices } c \text{ and } d \text{ with internal lines } k \text{ and } l \text{ connecting them. A dashed line connects } b \text{ and } c. \\ &= \frac{1}{2} \left(\text{Diagram: } R_0 \text{ with vertices } a, b, c, d \text{ and internal lines } i, j, k, l \text{ connected by dashed lines between } b \text{ and } c \text{ and } c \text{ and } d. \right. \\ &\quad \left. + \text{Diagram: } R_0 \text{ with vertices } a, b, c, d \text{ and internal lines } i, j, k, l \text{ connected by dashed lines between } a \text{ and } b \text{ and } c \text{ and } d. \right) \\ &= \frac{1}{2} \left(\text{Diagram: } R_0 \text{ with vertices } a, b \text{ and internal lines } i, j \text{ connected by dashed lines.} \right)^2. \end{aligned} \quad (3.16)$$

A similar results gives the product involving the first-order component of the \hat{T}_2 operator in Eq. (3.12), $\hat{T}_2^{(1)}$. Again, the factorization process is written algebraically,

$$\begin{aligned} \frac{1}{16} \sum_{ijkl} \frac{V_{ij}^{ab} V_{kl}^{cd}}{\varepsilon_{ijkl}^{abcd} \varepsilon_{ij}^{ab}} |\Phi_{ijkl}^{abcd}\rangle &= \frac{1}{32} \sum_{ijkl} \frac{V_{ij}^{ab} V_{kl}^{cd}}{\varepsilon_{ijkl}^{abcd} \varepsilon_{ij}^{ab}} |\Phi_{ijkl}^{abcd}\rangle + \frac{1}{32} \sum_{ijkl} \frac{V_{ij}^{ab} V_{kl}^{cd}}{\varepsilon_{ijkl}^{abcd} \varepsilon_{cd}^{kl}} |\Phi_{ijkl}^{abcd}\rangle \\ &= \frac{1}{32} \sum_{ijkl} \frac{V_{ij}^{ab} V_{kl}^{cd}}{\varepsilon_{ijkl}^{abcd} \varepsilon_{ij}^{ab} \varepsilon_{kl}^{cd}} \frac{\varepsilon_{kl}^{cd} + \varepsilon_{ij}^{ab}}{\varepsilon_{ijkl}^{abcd} \varepsilon_{ij}^{ab} \varepsilon_{kl}^{cd}} |\Phi_{ijkl}^{abcd}\rangle \\ &= \frac{1}{2} \left(\frac{1}{4} \sum_{abij} \frac{V_{ij}^{ab}}{\varepsilon_{ij}^{ab}} |\Phi_{ij}^{ab}\rangle \right) \left(\frac{1}{4} \sum_{cdkl} \frac{V_{kl}^{cd}}{\varepsilon_{kl}^{cd}} |\Phi_{kl}^{cd}\rangle \right) = \frac{1}{2} (\hat{T}_2^{(1)})^2. \end{aligned} \quad (3.17)$$

Lastly, for the disconnected terms from $\hat{V} \hat{f} |\Phi_0\rangle$ and $\hat{f} \hat{V} |\Phi_0\rangle$, the first duplication step

can be skipped and the diagrams can be factorized following the procedure in Eq. (2.7.1),

$$\text{Diagram on the left} + \text{Diagram in the middle} = \text{Diagram on the right} . \quad (3.18)$$

This factorization results in a mixed term between the first-order components from the \hat{T}_1 and \hat{T}_2 operators,

$$\begin{aligned} \frac{1}{4} \sum_{\substack{abc \\ ijk}} \frac{V_{ij}^{ab} f_k^c}{\varepsilon_{ijk}^{abc} \varepsilon_{ij}^{ab}} |\Phi_{ijk}^{abc}\rangle + \frac{1}{4} \sum_{\substack{abc \\ ijk}} \frac{V_{ij}^{ab} f_k^c}{\varepsilon_{ijk}^{abc} \varepsilon_k^c} |\Phi_{ijk}^{abc}\rangle &= \frac{1}{4} \sum_{\substack{abcd \\ ijk}} V_{ij}^{ab} f_k^c \frac{\varepsilon_k^c + \varepsilon_{ij}^{ab}}{\varepsilon_{ijk}^{abc} \varepsilon_{ij}^{ab} \varepsilon_k^c} |\Phi_{ijk}^{abc}\rangle \\ &= \left(\sum_{ck} \frac{f_k^c}{\varepsilon_k^c} |\Phi_k^c\rangle \right) \left(\frac{1}{4} \sum_{abi} \frac{V_{ij}^{ab}}{\varepsilon_{ij}^{ab}} |\Phi_{ij}^{ab}\rangle \right) = \hat{T}_1^{(1)} \hat{T}_2^{(1)} \end{aligned} \quad (3.19)$$

Adding these factorized contributions from Eqs. (3.15), (3.17), and (3.19) gives $\frac{1}{2} (\hat{T}_1^{(1)})^2 + \hat{T}_1^{(1)} \hat{T}_2^{(1)} + \frac{1}{2} (\hat{T}_2^{(1)})^2 = \frac{1}{2} (\hat{T}_1^{(1)} + \hat{T}_2^{(1)})^2$. Repeating this procedure for all diagrams with two disconnected parts ($L = 2$) adds similar terms of all orders. The final contribution from the $L = 2$ class of diagrams with two disconnected parts is,

$$\sum_{n=0}^{\infty} [\hat{R}_0 (\hat{V} - \Delta E_0)]^n |\Phi_0\rangle_{L=2} = \frac{1}{2} \hat{T}^2. \quad (3.20)$$

A similar form results from any class of diagrams with k disconnected pieces,

$$\sum_{n=0}^{\infty} [\hat{R}_0 (\hat{V} - \Delta E_0)]^n |\Phi_0\rangle_{L=k} = \frac{1}{k!} \hat{T}^k. \quad (3.21)$$

Therefore, summing over all classes of diagrams gives the final result that justifies the

exponential ansatz,

$$|\Psi\rangle = \sum_{k=0}^{\infty} \sum_{n=0}^{\infty} \left[\hat{R}_0 (\hat{V} - \Delta E_0) \right]^n |\Phi_0\rangle_{L=k} = \sum_{k=0}^{\infty} \frac{1}{k!} \hat{T}^k |\Phi_0\rangle = e^{\hat{T}} |\Phi_0\rangle. \quad (3.22)$$

This equation shows the true strength and elegance of coupled cluster theory. By an ingenious reorganization and factorization of certain MBPT diagrams, the exponential ansatz captures the contribution of these excitations to infinite order. A more comprehensive derivation of the linked-cluster theorem can be found in [18].

3.3 Example: Pairing Model

It's beneficial to illustrate a simplified example of coupled cluster theory. For this purpose, we turn our attention to the simple pairing model. This system uses a model space of N shells, or degenerate groups of single-particle states, each with two opposite spin orbitals.

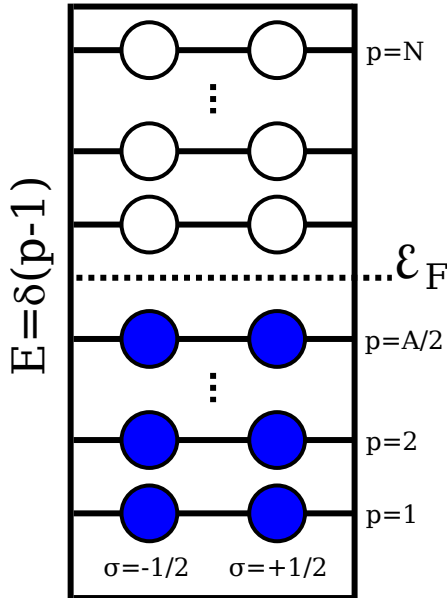


Figure 3.1: Schematic representation of the pairing model space. The shells are equally spaced and doubly degenerate with one spin-up and one spin-down state.

With a closed-shell reference state, the Hamiltonian is restricted to interact only between unbroken pairs, which can be written as,

$$\begin{aligned} {}^{(1)}\hat{H} &= \delta \sum_p^N (p-1) \left[\hat{a}_{p+}^\dagger \hat{a}_{p+} + \hat{a}_{p-}^\dagger \hat{a}_{p-} \right], \quad \text{and} \\ {}^{(2)}\hat{H} &= -\frac{g}{2} \sum_{pq}^N \hat{a}_{p+}^\dagger \hat{a}_{p-}^\dagger \hat{a}_{q-} \hat{a}_{q+}, \end{aligned} \quad (3.23)$$

where δ and g are free parameters and the \pm labels represent the spin-up and spin-down states, respectively.

As with all other coupled cluster calculations in this work, the first step is transforming the problem to the Hartree-Fock basis. In this case, the restriction to unbroken pairs means that the original single-particle states do not mix with states in other shells. In fact, the original basis is already an eigenbasis of the Fock operator, Eq. (2.5), so that the HF transformation is reduced to a redefinition of the single-particle energies to their corresponding Hartree-Fock energies, leaving the two-body interaction unchanged,

$$\begin{aligned} \varepsilon_{pmp} &= {}^{(1)}H_{pmp}^{pmp} + \sum_{im_i} {}^{(2)}H_{pmp}^{pmp}{}^{im_i} = \delta(p-1) - \frac{g}{2}, \\ V_{rs}^{pq} &= {}^{(2)}H_{rs}^{pq}. \end{aligned} \quad (3.24)$$

Because of the pairing restriction, only hole-state energies have to be redefined.

The next step in calculating the ground-state correlation energy is to solve the CCD equations in the Hartree-Fock basis. The system of equations comes from the terms of Eq. (3.10) that contain only the \hat{T}_2 operator, and are most easily derived with diagrammatic

techniques, see [18].

$$\begin{aligned}
 & \langle \Phi_{ij}^{ab} | (\hat{H} e^{\hat{T}_2})_C | \Phi_0 \rangle - \text{(diagram with crossed dashed line)} - \text{(diagram with crossed dashed line)} = \text{(diagram with crossed dashed line)} \\
 & + \text{(diagram with crossed dashed line)} \\
 & + \text{(diagram with crossed dashed line)} \\
 & (\varepsilon_i + \varepsilon_j - \varepsilon_a - \varepsilon_b) t_{ij}^{ab} = V_{ij}^{ab} + \frac{1}{2} \sum_{kl} V_{ij}^{kl} t_{kl}^{ab} + \frac{1}{2} \sum_{cd} V_{cd}^{ab} t_{ij}^{cd} - \hat{P}(ij|ab) \sum_{kc} V_{ic}^{kb} t_{kj}^{ac} \\
 & + \frac{1}{4} \sum_{klcd} V_{cd}^{kl} t_{kl}^{ab} t_{ij}^{cd} + \hat{P}(ab) \sum_{klcd} V_{cd}^{kl} t_{lj}^{ac} t_{ki}^{bd} - \hat{P}(ij) \frac{1}{2} \sum_{klcd} V_{cd}^{kl} t_{lj}^{ab} t_{ki}^{cd} - \hat{P}(ab) \frac{1}{2} \sum_{klcd} V_{cd}^{kl} t_{ij}^{db} t_{kl}^{ca}. \tag{3.25}
 \end{aligned}$$

The CCD equations are written in this particular form so that an initial guess for all the amplitudes t_{ij}^{ab} can be used to calculate the right-hand side of Eq. (3.3) and update the amplitudes on the left-hand side iteratively until the amplitudes do not change within a certain tolerance.

Lastly, the CCD correlation energy can be found with the \hat{T}_2 term of Eq. (3.1),

$$\Delta E_{\text{CCD}} = \langle \Phi_0 | (\hat{H} e^{\hat{T}_2})_C | \Phi_0 \rangle = \text{(diagram with two loops)} = \frac{1}{4} \sum_{klcd} V_{cd}^{kl} t_{kl}^{cd}. \tag{3.26}$$

The correlation energies for a specific case, with $\delta = 1.0$, $N = 4$, and $A = 4$, were calculated for a number of different interaction strengths, g . The results are shown in Fig. 3.2 along

with the MBPT correlation energies to third (MBPT3) and fourth (MBPT4) orders for comparison. The nonzero MBPT expressions for second and third order are,

$$\Delta E_{\text{MBPT}2} = \frac{1}{4} \sum_{ijab} \frac{V_{ab}^{ij} V_{ij}^{ab}}{\varepsilon_{ij}^{ab}}, \quad (3.27)$$

$$\Delta E_{\text{MBPT}3} = \Delta E_{\text{MBPT}2} + \frac{1}{8} \sum_{ijabcd} \frac{V_{ab}^{ij} V_{cd}^{ab} V_{ij}^{cd}}{\varepsilon_{ij}^{ab} \varepsilon_{ij}^{cd}} + \frac{1}{8} \sum_{ijklab} \frac{V_{ab}^{ij} V_{ij}^{kl} V_{kl}^{ab}}{\varepsilon_{ij}^{ab} \varepsilon_{kl}^{ab}}. \quad (3.28)$$

Generally, the fourth-order expression contains 39 additional terms. However, most of these vanish in this case because of the form of the pairing interaction.

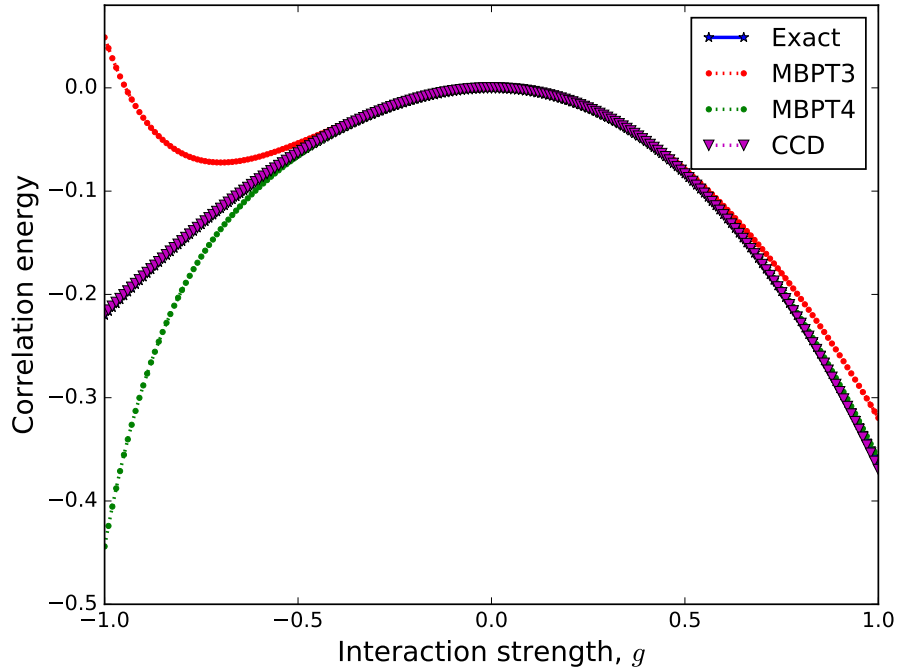


Figure 3.2: Correlation energy for the pairing model with exact diagonalization, CCD, and perturbation theory to third (MBPT3) and fourth order (MBPT4) for a range of interaction values, g .

Also shown are the exact results from the CI method. With an example this small, it's possible to diagonalize, and even show explicitly, the full CI Hamiltonian matrix for an exact result. There are six possible Slater determinants with no broken pairs, one representing the

reference state, four representing various 2p-2h excitations, and one representing a 4p-4h excitation. The diagonal elements of the matrix include the single-particle energies of the constituent states, and the matrix elements between Slater determinants with no overlap vanish in accordance with the Slater-Condon rules, see Eq. (2.6) and [89, 99]. The full Hamiltonian matrix to be diagonalized is,

$$H = \begin{bmatrix} 2\delta - g & -g/2 & -g/2 & -g/2 & -g/2 & 0 \\ -g/2 & 4\delta - g & -g/2 & -g/2 & -0 & -g/2 \\ -g/2 & -g/2 & 6\delta - g & 0 & -g/2 & -g/2 \\ -g/2 & -g/2 & 0 & 6\delta - g & -g/2 & -g/2 \\ -g/2 & 0 & -g/2 & -g/2 & 8\delta - g & -g/2 \\ 0 & -g/2 & -g/2 & -g/2 & -g/2 & 10\delta - g \end{bmatrix}. \quad (3.29)$$

As methods to obtain the ground-state correlation energy, both CI and CC decouple, to some degree, the reference state and excitations from it. This decoupling has the effect of shuffling correlations into the reference state and suppressing matrix elements connected to it. Full decoupling between the reference state and all other Slater determinants can only be achieved with untruncated versions of these techniques, while decoupling of the strongest correlations can be approximately obtained with appropriate truncations. However, unlike other many-body methods, the most unique aspect of the CC similarity transformation is that because of its non-unitarity, the resulting Hamiltonian will not be Hermitian. This decoupling and non-Hermiticity can be seen in Fig. 3.3, which shows the effect of the CC similarity transformation on the Hamiltonian for a pairing case with $N = 6$ and $A = 4$. The effective Hamiltonian \bar{H} shown in Fig. 3.3 can be explicitly built, and it happens to be beneficial to do so as part of most CC calculations, both for solving the CC equations and for use in post-CC methods. This topic is discussed in detail in the next section.

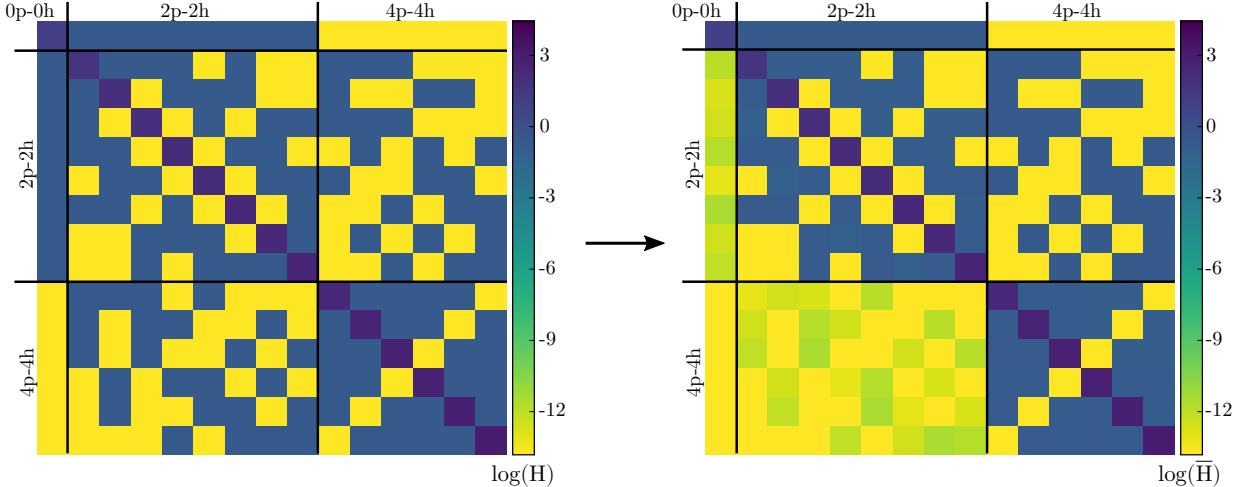


Figure 3.3: Visualization of the CCD similarity transform on the pairing Hamiltonian for four particles and six shells. This shows the main function of CCD, which is to decouple 2p-2h excitations from the ground state, shown by the suppression of matrix elements on the first column. In the pairing model, this also has the effect of decoupling 2p-2h excitations from 4p-4h excitations. Also, the non-unitary nature of the transformation is obvious given the asymmetry of the resulting Hamiltonian.

3.4 Solving the Coupled Cluster Equations

As described above, the coupled cluster equations are solved by first initializing all of the cluster amplitudes, then updating them by computing various sums over particle and hole combinations, $\text{CC}(\hat{T})$. This updating procedure is performed over multiple iterations until the amplitudes stay unchanged within a certain tolerance,

$$\begin{aligned} \text{Initialize : } & \quad \hat{T}^{(0)} = \hat{T}_{\text{init}}, \\ \text{Iterate : } & \quad \hat{T}^{(n+1)} \leftarrow \text{CC}(\hat{T}^{(n)}). \end{aligned} \quad (3.30)$$

Generally, the convergence of this algorithm depends on the relative magnitudes between the inter-particle force and the single-particle energy spacing. For a relatively small Fermi gap between the closed shell of occupied states and the unoccupied particle states, the energy denominators will approach zero and cause a divergent or chaotic solution [112]. Physically,

this situation occurs when a system exhibits strong many-particle clustering, which is difficult to capture with only the single and double excitations of CCSD. A simple way to avoid this ill-defined behavior is to scale the energy denominators for early iterations or to employ linear mixing to dampen the solution,

$$\hat{T}^{(n+1)} \leftarrow \alpha \text{CC}(\hat{T}^{(n)}) + (1 - \alpha) \hat{T}^{(n)}. \quad (3.31)$$

If a solution to a highly-collective system does not diverge, it typically converges very slowly. To improve the convergence rate, techniques already utilized for the Hartree-Fock iterations can also be employed here, such as DIIS [96, 97] or Broyden's method [98]. The additional computational complexity for the CC iterations is simply a multiplicative factor equal to the number of iterations performed. Typical calculations in this work with DIIS acceleration are converged within ~ 30 iterations. Therefore, any significant improvements to the CC algorithm will involve the expensive sums embedded within the function $\text{CC}(\hat{T}^{(n)})$.

3.4.1 Symmetry Channels

For the coupled cluster equations, as well as many other many-body methods, the first way to simplify the various sums is to exploit any symmetries of the underlying Hamiltonian of a particular problem. These symmetries manifest as conserved quantities, and because of the underlying nature of the cluster operators, see Section 3.2, these must conserve these quantum numbers as well. For example, the pairing Hamiltonian of Section 3.3 has a symmetry that conserves both the total spin projection and the number of pairs. The Coulomb Hamiltonian of Section 3.5, which has translational symmetry, conserves the linear momentum of any state. Finally, the spherical symmetry of the nuclear Hamiltonian ensures that angular

momentum and parity are conserved. To utilize these symmetries, any sums that contain many-body states with different conserved quantum numbers can be ignored. For efficiency, these symmetry groups can be pre-sorted into *channels*, $\Sigma_{\vec{\xi}}$, where $\vec{\xi}$ represents the relevant quantum numbers of a certain channel.

For CCSD calculations, useful types of channels include the direct two-body channels, $\Sigma_{\vec{\xi}_1}$ —which categorizes the vector sum of two single-particle-state quantum numbers—and the cross two-body channels, $\Sigma_{\vec{\xi}_2}$ —which categorizes the vector difference of two single-particle-state quantum numbers or, equivalently, the vector sum of a the quantum numbers of a single-particle state and a time-reversed single-particle state.

$$\vec{\xi}_{pq} = \vec{\xi}_p + \vec{\xi}_q \longrightarrow |pq\rangle \in \Sigma_{\vec{\xi}_1=\vec{\xi}_{pq}} \quad (3.32)$$

$$\vec{\xi}_{p\bar{q}} = \vec{\xi}_p - \vec{\xi}_q = \vec{\xi}_p + \vec{\xi}_{\bar{q}} \longrightarrow |p\bar{q}\rangle \in \Sigma_{\vec{\xi}_2=\vec{\xi}_{p\bar{q}}} \quad (3.33)$$

Also useful are the one-body channels, $\Sigma_{\vec{\xi}_3}$, which categorize both single-particle states by their conserved quantum numbers. These one-body channels can also characterize a special type of three-body state: the vector difference between the quantum numbers of a direct two-body state and a single-particle state or, equivalently, the vector sum of the quantum numbers of a two-body direct state and a time-reversed single-particle state,

$$\vec{\xi}_p \longrightarrow |p\rangle \in \Sigma_{\vec{\xi}_3=\vec{\xi}_p} \quad (3.34)$$

$$\vec{\xi}_{pqr} = \vec{\xi}_p + \vec{\xi}_q - \vec{\xi}_r = \vec{\xi}_p + \vec{\xi}_q + \vec{\xi}_{\bar{r}} \longrightarrow |pqr\rangle \in \Sigma_{\vec{\xi}_3=\vec{\xi}_{pqr}}. \quad (3.35)$$

Using these channel structures, the interaction matrix elements and cluster amplitudes can be built in different ways. The full applicability of these structures are shown in detail

in appendix C, but a few examples using sums in the CCD equations (3.3) are shown here. The direct two-body channels can be used when two summed indices appear in the bra- or ket-state of multiple matrix-elements,

$$\frac{1}{2} \sum_{cd} V_{cd}^{ab} t_{ij}^{cd} = \frac{1}{2} \sum_{|cd\rangle} V_{cd}^{ab} t_{ij}^{cd} \text{ for } |cd\rangle \in \Sigma_{\vec{\xi}_{ab}} = \Sigma_{\vec{\xi}_{ij}}. \quad (3.36)$$

The cross two-body channels are used when two summed indices appear in the opposite corresponding bra- and ket-states of multiple matrix-matrix elements,

$$\sum_{kc} V_{ic}^{kb} t_{kj}^{ac} = \sum_{|k\bar{c}\rangle} V_{i\bar{b}}^{k\bar{c}} t_{k\bar{c}}^{a\bar{j}} \text{ for } |k\bar{c}\rangle \in \Sigma_{\vec{\xi}_{i\bar{b}}} = \Sigma_{\vec{\xi}_{a\bar{j}}}. \quad (3.37)$$

Lastly, the one- and three-body channels are used when a single summed index appears opposite a direct two-body state in multiple matrix elements,

$$\frac{1}{2} \sum_{klcd} V_{cd}^{kl} t_{ij}^{db} t_{kl}^{ca} = \frac{1}{2} \sum_{\substack{|kl\bar{c}\rangle \\ |d\rangle}} V_d^{kl\bar{c}} t_{ij\bar{b}}^d t_{kl\bar{c}}^a \text{ for } |kl\bar{c}\rangle, |d\rangle \in \Sigma_{\vec{\xi}_{ij\bar{b}}} = \Sigma_{\vec{\xi}_a}. \quad (3.38)$$

3.4.2 Matrix Structures and Intermediates

Symmetry channels not only provide an organized structure for the interaction matrix elements and cluster amplitudes, and remove any terms that violate the underlying symmetry of a problem, but they also naturally provide an efficient way of performing sums using matrix-matrix multiplications. For example, the sums in Eqs. (3.36)–(3.38) can be reformulated as matrix-matrix multiplications by structuring the channel-separated interaction matrix elements and cluster amplitudes into individual matrices. These operations can be performed very quickly using highly optimized linear algebra algorithms like those found in

BLAS (Basic Linear Algebra Subprograms) [113]. The matrices can be reordered so that the summed indices correspond to the internal columns and rows of those matrices.

For the direct two-body case of Eq. (3.36), the structures are already in the correct order such that the state $|cd\rangle$, indexed by the columns of \mathbf{V} and the rows of \mathbf{t} , is summed by multiplying the two matrices,

$$\frac{1}{2} \sum_{cd} V_{cd}^{ab} t_{ij}^{cd} = \frac{1}{2} \mathbf{V}_{cd}^{ab} \cdot \mathbf{t}_{ij}^{cd} \text{ for } |ab\rangle, |ij\rangle, |cd\rangle \in \Sigma_{\vec{\xi}_1}. \quad (3.39)$$

For the cross two-body case of Eq. (3.37), the states $|j\rangle$, $|b\rangle$, and $|c\rangle$ are time reversed so that the summed variables are collected in a state $|k\bar{c}\rangle$. Then the matrix structures are reordered so this state is indexed by columns and rows of \mathbf{t} and \mathbf{V} , respectively,

$$\sum_{kc} V_{ic}^{kb} t_{kj}^{ac} = \mathbf{t}_{k\bar{c}}^{a\bar{j}} \cdot \mathbf{V}_{ib}^{k\bar{c}} \text{ for } |a\bar{j}\rangle, |i\bar{b}\rangle, |k\bar{c}\rangle \in \Sigma_{\vec{\xi}_2}. \quad (3.40)$$

Lastly, for the case of Eq. (3.38), the states $|b\rangle$ and $|c\rangle$ are time-reversed so that the states $|d\rangle$ and $|kl\bar{c}\rangle$ appear in two different matrix elements. Then, the matrix structures are reorganized so the summed states occur in the appropriate rows and columns for matrix-matrix multiplication,

$$\frac{1}{2} \sum_{klcd} V_{cd}^{kl} t_{ij}^{db} t_{kl}^{ca} = \frac{1}{2} \mathbf{t}_{kl\bar{c}}^a \cdot \mathbf{V}_d^{kl\bar{c}} \cdot \mathbf{t}_{ij\bar{b}}^d \text{ for } |a\rangle, |ij\bar{b}\rangle, |kl\bar{c}\rangle, |d\rangle \in \Sigma_{\vec{\xi}_3}. \quad (3.41)$$

These sums correspond to different components of the updated cluster amplitudes according to Eq. (3.30), so that different channel structures of the matrix-matrix multiplications correspond to different amplitude structures according to the sum's external indices. The two external direct two-body states of Eq. (3.39), $|ab\rangle$ and $|ij\rangle$, naturally map to the direct

amplitude structure,

$$\mathbf{t}_{ij}^{ab} \leftarrow \frac{1}{2} \mathbf{V}_{cd}^{ab} \cdot \mathbf{t}_{ij}^{cd} \text{ for } |ab\rangle, |ij\rangle, |cd\rangle \in \Sigma_{\vec{\xi}_1}. \quad (3.42)$$

Similarly, the two external cross two-body states of Eq. (3.40), $|a\bar{j}\rangle$ and $|i\bar{b}\rangle$, naturally map to the cross amplitude structure,

$$\mathbf{t}_{i\bar{b}}^{a\bar{j}} \leftarrow \mathbf{t}_{k\bar{c}}^{a\bar{j}} \cdot \mathbf{V}_{i\bar{b}}^{k\bar{c}} \text{ for } |a\bar{j}\rangle, |i\bar{b}\rangle, |k\bar{c}\rangle \in \Sigma_{\vec{\xi}_2}. \quad (3.43)$$

Lastly, the one- and three-body external states of of Eq. (3.41), $|a\rangle$ and $|i\bar{b}\rangle$, naturally map to the one-body amplitude structure characterized by the index a ,

$$\mathbf{t}_{ij\bar{b}}^a \leftarrow \frac{1}{2} \mathbf{t}_{kl\bar{c}}^a \cdot \mathbf{V}_d^{kl\bar{c}} \cdot \mathbf{t}_{ij\bar{b}}^d \text{ for } |a\rangle, |ij\bar{b}\rangle, |kl\bar{c}\rangle, |d\rangle \in \Sigma_{\vec{\xi}_3}. \quad (3.44)$$

The last summation in the matrix-matrix form of Eqs. (3.41) and (3.44) involves two multiplications, which suggests the need for an *intermediate* matrix to hold the result of the first operation. This is the last main ingredient to an efficient CC algorithm. To see the benefit of intermediate structures, it's helpful to examine an expensive sum from the CCD equations. For typical calculations, particle states outnumber hole states by an order of magnitude, $n_p \sim 10n_h$, which means that one of the most expensive sums is,

$$\frac{1}{4} \sum_{klcd} \mathbf{V}_{cd}^{kl} t_{kl}^{ab} t_{ij}^{cd}. \quad (3.45)$$

Because this term must be computed for each t_{ij}^{ab} , its computational cost naively scales as

$\mathcal{O}(N_h^4 N_p^4)$. However, using the matrix form of this sum and an intermediate matrix,

$$\frac{1}{4} \sum_{klcd} V_{cd}^{kl} t_{kl}^{ab} t_{ij}^{cd} = \frac{1}{4} \mathbf{t}_{kl}^{ab} \cdot (\mathbf{V}_{cd}^{kl} \cdot \mathbf{t}_{ij}^{cd}) = \frac{1}{4} \mathbf{t}_{kl}^{ab} \cdot \mathbf{X}_{ij}^{kl} \rightarrow \mathbf{t}_{ij}^{ab}. \quad (3.46)$$

this term is now computed as the combination of two sums, each scaling as $\mathcal{O}(N_h^4 N_p^2)$.

These intermediates can also be used as a way to combine similar sums. For example, the last step of Eq. (3.46) has a very similar structure to the first sum in Eq. (3.3). Therefore, the two sums can be written with a common intermediate as,

$$\begin{aligned} \frac{1}{2} \sum_{kl} V_{ij}^{kl} t_{kl}^{ab} + \frac{1}{4} \sum_{klcd} V_{cd}^{kl} t_{kl}^{ab} t_{ij}^{cd} &= \frac{1}{2} \mathbf{t}_{kl}^{ab} \cdot \left[\mathbf{V}_{ij}^{kl} + \frac{1}{2} \mathbf{V}_{cd}^{kl} \cdot \mathbf{t}_{ij}^{cd} \right] = \frac{1}{4} \mathbf{t}_{kl}^{ab} \cdot \mathbf{X}_{ij}^{kl} \rightarrow \mathbf{t}_{ij}^{ab}, \\ \text{where, } \mathbf{X}_{ij}^{kl} &= \mathbf{V}_{ij}^{kl} + \frac{1}{2} \mathbf{V}_{cd}^{kl} \cdot \mathbf{t}_{ij}^{cd}. \end{aligned} \quad (3.47)$$

It just so happens that this form of the intermediate X_{ij}^{kl} is equivalent to the hhhh component of the CCD similarity transformed Hamiltonian, \bar{H} . Constructing other intermediates in this way gives similar results, so it's a natural extension to actually construct the effective Hamiltonian at each iteration for the express purpose of using it as different intermediate components for the CC equations. This has the added benefit of having already computed the effective Hamiltonian for post-CC methods. The different components of the CCD effective Hamiltonian, $\bar{H}_{\text{CCD}} = (\hat{H} e^{\hat{T}_2})_c$, are written below in both algebraic and diagrammatic form. One-body components correspond to the vertex type  and two-body terms correspond to the vertex type . The pp, one-body component of \bar{H}_{CCD}

is,

$$X_b^a = f_b^a - \frac{1}{2} \sum_{klc} V_{bc}^{kl} t_{kl}^{ac}. \quad (3.48)$$

The hh, one-body component is,

$$X_j^i = f_j^i + \frac{1}{2} \sum_{kcd} V_{cd}^{ik} t_{jk}^{cd}. \quad (3.49)$$

The hhhh, two-body component, which appears as the intermediate in Eqs. (3.46) and (3.4.2),

is,

$$X_{kl}^{ij} = V_{kl}^{ij} + \frac{1}{2} \sum_{cd} V_{cd}^{ij} t_{kl}^{cd}. \quad (3.50)$$

Lastly, the hphp, two-body component is,

$$\begin{aligned}
 & \text{Diagram: Two vertical lines } j \text{ and } i \text{ with arrows } j \downarrow \text{ and } i \downarrow \text{ connected by a wavy line labeled } a \text{ and } b. \\
 & = \text{Diagram: Two vertical lines } j \text{ and } i \text{ with arrows } j \downarrow \text{ and } i \downarrow \text{ connected by a dashed line.} \\
 & + \frac{1}{2} \text{Diagram: Three vertical lines } j, i, k \text{ with arrows } j \downarrow, i \downarrow, k \downarrow \text{ connected by a wavy line } a \text{ and } b. \\
 X_{jb}^{ia} &= V_{jb}^{ia} - \frac{1}{2} \sum_{kc} V_{cb}^{ik} t_{jk}^{ca}. \quad (3.51)
 \end{aligned}$$

Using these terms, the CCD equations can be written in pseudo-linear form using the 2p-2h component of effective Hamiltonian form of the equations, Eq. (3.9). This also explicitly shows the decoupling of the effective Hamiltonian with 2p-2h excitations. The pphh, two-body component, which should vanish when the CCS amplitudes have converged, is,

$$\begin{aligned}
 & \text{Diagram: Two vertical lines } a \text{ and } b \text{ with arrows } a \uparrow \text{ and } b \uparrow \text{ connected by a wavy line.} \\
 & = 0 = \text{Diagram: Two vertical lines } a \text{ and } b \text{ with arrows } a \uparrow \text{ and } b \uparrow \text{ connected by a dashed line.} \\
 & + \text{Diagram: Two vertical lines } a \text{ and } b \text{ with arrows } a \uparrow \text{ and } b \uparrow \text{ connected by a wavy line } c \text{ and } i. \\
 & + \text{Diagram: Two vertical lines } a \text{ and } b \text{ with arrows } a \uparrow \text{ and } b \uparrow \text{ connected by a wavy line } k \text{ and } j. \\
 & + \text{Diagram: Three vertical lines } a, c, d \text{ with arrows } a \uparrow, c \uparrow, d \uparrow \text{ connected by a dashed line.} \\
 & + \text{Diagram: Three vertical lines } a, k, l \text{ with arrows } a \uparrow, k \uparrow, l \uparrow \text{ connected by a wavy line } i. \\
 & + \text{Diagram: Three vertical lines } a, k, c \text{ with arrows } a \uparrow, k \uparrow, c \uparrow \text{ connected by a wavy line } i. \\
 X_{ij}^{ab} &= 0 = V_{ij}^{ab} + \hat{P}(ab) \sum_c X_c^a t_{ij}^{cb} - \hat{P}(ij) \sum_k X_i^k t_{kj}^{ab} \\
 & + \frac{1}{2} \sum_{cd} X_{cd}^{ab} t_{ij}^{cd} + \frac{1}{2} \sum_{kl} X_{ij}^{kl} t_{kl}^{ab} - \hat{P}(ab|ij) \sum_{kc} X_{ic}^{kb} t_{kj}^{ac}. \quad (3.52)
 \end{aligned}$$

The components and intermediates of the CCSD effective Hamiltonian are much more complicated and are shown with their corresponding sums in appendix B.

3.5 Example: Homogeneous Electron Gas

Another relatively simple calculation using the CCD approximation is the homogeneous electron gas. This example aims to calculate the ground state energy of a three-dimensional gas of electrons subject to Coulomb repulsion. This is an approximate model of the valence electrons in a metal, subject to a uniform background of positive charge from the nuclei and core electrons [114]. As will be explained below, this calculation employs pure-momentum eigenstates such that 1p-1h excitations from the reference state are forbidden by momentum conservation. This means that the problem reduces to the doubles approximation. To obtain realistic results, a sufficiently-sized basis with a sufficient number of electrons must be used. Therefore, the improvements discussed in Section 3.4 are necessary to keep the computation time manageable as the system size increases.

With a uniform background potential, the electron gas can be constructed using eigenfunctions of the kinetic energy operator, $(^1)\hat{H} = \hat{T} = -\frac{\hbar^2}{2m}\nabla^2$. In an infinite volume, however, there are an unlistable number of plane wave modes which satisfy this condition due to the continuous nature of the linear momentum eigenstates. Therefore, the single-particle orbits will be constructed in a finite box of volume Ω and length L , and then the limit $L \rightarrow \infty$ can be taken after various expectation values have been computed,

$$\begin{aligned} \frac{-\hbar^2}{2m}\nabla^2\phi_{\mathbf{k}\sigma}(\mathbf{r}) &= \epsilon_{\mathbf{k}}\phi_{\mathbf{k}\sigma}(\mathbf{r}), \\ \phi_{\mathbf{k}\sigma}(\mathbf{r}) &= \frac{1}{\sqrt{\Omega}}\exp(i\mathbf{k}\mathbf{r})\xi_{\sigma}, \end{aligned} \tag{3.53}$$

where m is the electron mass, \mathbf{k} is the wave number, and ξ_{σ} is the spin function for either

spin up or down electrons

$$\xi_{\sigma=+1/2} = \begin{pmatrix} 1 \\ 0 \end{pmatrix} \quad \xi_{\sigma=-1/2} = \begin{pmatrix} 0 \\ 1 \end{pmatrix}. \quad (3.54)$$

Assuming the single-particle orbits follow periodic boundary conditions within the containing box ($\phi(\mathbf{r}_i) = \phi(\mathbf{r}_i + L)$ for $i = x, y, z$) the wave numbers are quantized,

$$k_i = \frac{2\pi n_i}{L} \quad i = x, y, z \quad n_i = 0, \pm 1, \pm 2, \dots \quad (3.55)$$

A state can therefore be characterized by the quantum numbers n_x , n_y , and n_z as well as the spin quantum number σ . The energy of such a state, independent of the spin, can be written as

$$\epsilon_{n_x, n_y, n_z} = \frac{\hbar^2}{2m} \left(k_x^2 + k_y^2 + k_z^2 \right) = \frac{\hbar^2}{2m} \left(\frac{2\pi}{L} \right)^2 \left(n_x^2 + n_y^2 + n_z^2 \right). \quad (3.56)$$

Now that the single-particle orbits are established, a particular basis consisting of these orbits can be chosen such that all states are included up to a closed shell. This basis is then filled with electrons until a closed Fermi level is obtained. Additionally, only the unpolarized case, in which all orbitals are occupied with one spin-up and one spin-down electron, will be considered here. For this spherical-type level structure, the number of electrons required for closed shells increases quickly. For example, the first six shells contain 2, 14, 38, 54, 66 and 114 states, respectively.

A finite number of electrons A in a finite box of volume Ω naturally leads to the characterization of an infinite system by its number density density $\rho = A/\Omega$. The average

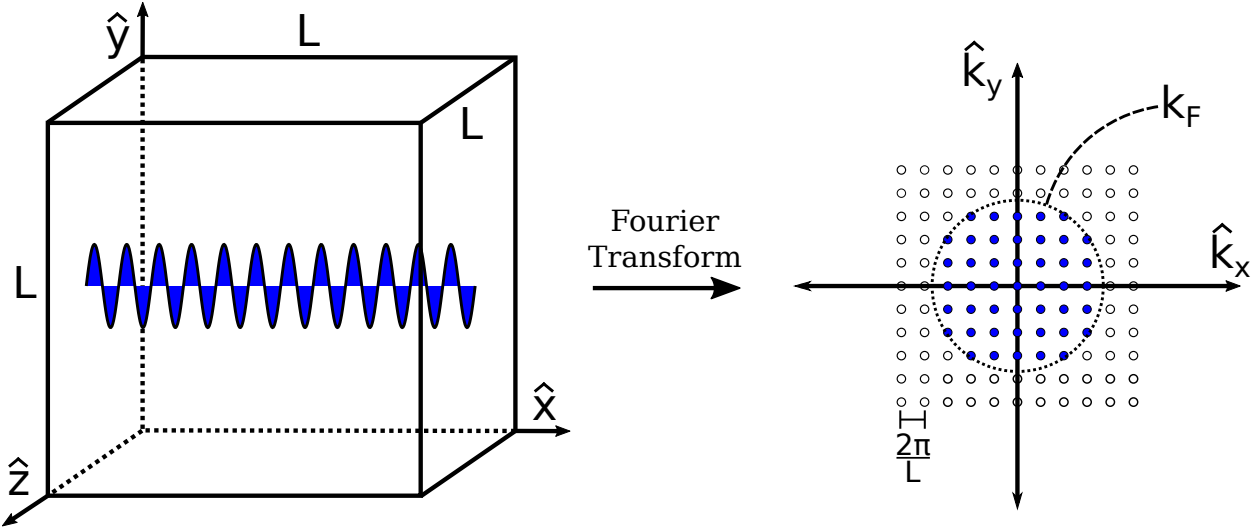


Figure 3.4: Visualization of the Fourier transform of a finite box. This transformation characterizes the construction of the single-particle basis for infinite matter, mapping plane waves in coordinate space onto finitely-spaced points in momentum space.

inter-electron distance, or *Wigner-Seitz radius*, is defined as

$$\frac{4}{3}\pi r_s^3 = \frac{1}{\rho}, \quad r_s = \left(\frac{3}{4\pi\rho}\right)^{1/3}. \quad (3.57)$$

In practice, these calculations are defined by the total number of shells included in the basis, the number of electrons, and the Wigner-Seitz radius, usually given in units of the Bohr radius, $r_b = \frac{\hbar}{mc\alpha}$, where c is the speed of light and α is the fine-structure constant.

The last ingredient to this many-body calculation is the interaction between the electrons, the well-known Coulomb force. Using atomic units, where the elementary charge $e = 1$ and the Coulomb constant $\frac{1}{4\pi\epsilon_0} = 1$, this potential is simply

$$V(\mathbf{r}_1, \mathbf{r}_2) = \frac{1}{|\mathbf{r}_1 - \mathbf{r}_2|}. \quad (3.58)$$

As mentioned in chapter 2, this potential can be utilized in second-quantization by computing

antisymmetrized integrals over the basis states. In this case, the integrals have the form,

$${}^{(2)}H_{rs}^{pq} \equiv \int d\mathbf{r}_1 d\mathbf{r}_2 \phi_{\mathbf{k}p\sigma_p}^*(\mathbf{r}_1) \phi_{\mathbf{k}q\sigma_q}^*(\mathbf{r}_2) \frac{1}{|\mathbf{r}_1 - \mathbf{r}_2|} [\phi_{\mathbf{k}r\sigma_r}(\mathbf{r}_1) \phi_{\mathbf{k}s\sigma_s}(\mathbf{r}_2) - \phi_{\mathbf{k}s\sigma_s}(\mathbf{r}_1) \phi_{\mathbf{k}r\sigma_r}(\mathbf{r}_2)]. \quad (3.59)$$

The symmetries of the Coulomb potential guarantee that the total linear momentum and total spin projection are conserved such that,

$$\mathbf{k}_p + \mathbf{k}_q = \mathbf{k}_r + \mathbf{k}_s \quad \text{and} \quad \sigma_p + \sigma_q = \sigma_r + \sigma_s. \quad (3.60)$$

The integral is relatively simple given the form of the basis functions. The result is given in terms of the momentum transfer, $\mathbf{q}_1 = \mathbf{k}_p - \mathbf{k}_r$ and $\mathbf{q}_2 = \mathbf{k}_p - \mathbf{k}_r$,

$${}^{(2)}H_{rs}^{pq} = \frac{4\pi\hbar c\alpha}{\Omega} \left[\frac{\delta_{\sigma_p\sigma_r}\delta_{\sigma_q\sigma_s}}{|\mathbf{q}_1|^2} - \frac{\delta_{\sigma_p\sigma_s}\delta_{\sigma_q\sigma_r}}{|\mathbf{q}_2|^2} \right] \quad (3.61)$$

The last preparation step before performing the coupled cluster algorithm is the Hartree-Fock transformation. As with the pairing model, the single-particle orbitals are already eigenfunctions of the Fock operator, in this case because the translational invariance of the plane wave basis functions ensure that the HF terms of the form ${}^{(2)}H_{qi}^{pi}$ vanish due to momentum conservation, see Eq. (2.5). Therefore, the HF transformation consists simply of redefining the single-particle energies while the two-body interaction is left unchanged.

$$\begin{aligned} \varepsilon_p &= \epsilon_{\mathbf{k}p} + \sum_i {}^{(2)}H_{pi}^{pi} \\ V_{rs}^{pq} &= {}^{(2)}H_{rs}^{pq} \end{aligned} \quad (3.62)$$

As mentioned above, in the plane-wave basis, any single excitation from the reference

state vanishes automatically due to momentum conservation so that $t_i^a = 0$. Therefore, it's necessary to include only double excitations (before adding triples, etc.). Therefore, calculations for the electron gas use the pseudo-linear form of the CCD equations (B.21) and an effective Hamiltonian that excludes single excitations in Eqns. (3.48)-(B.4). To explore the HEG equation-of-state, the total energy per electron can be calculated as a function of the Wigner-Seitz radius. In the limit $N, L \rightarrow \infty$, the plot in Fig. 3.5 represents

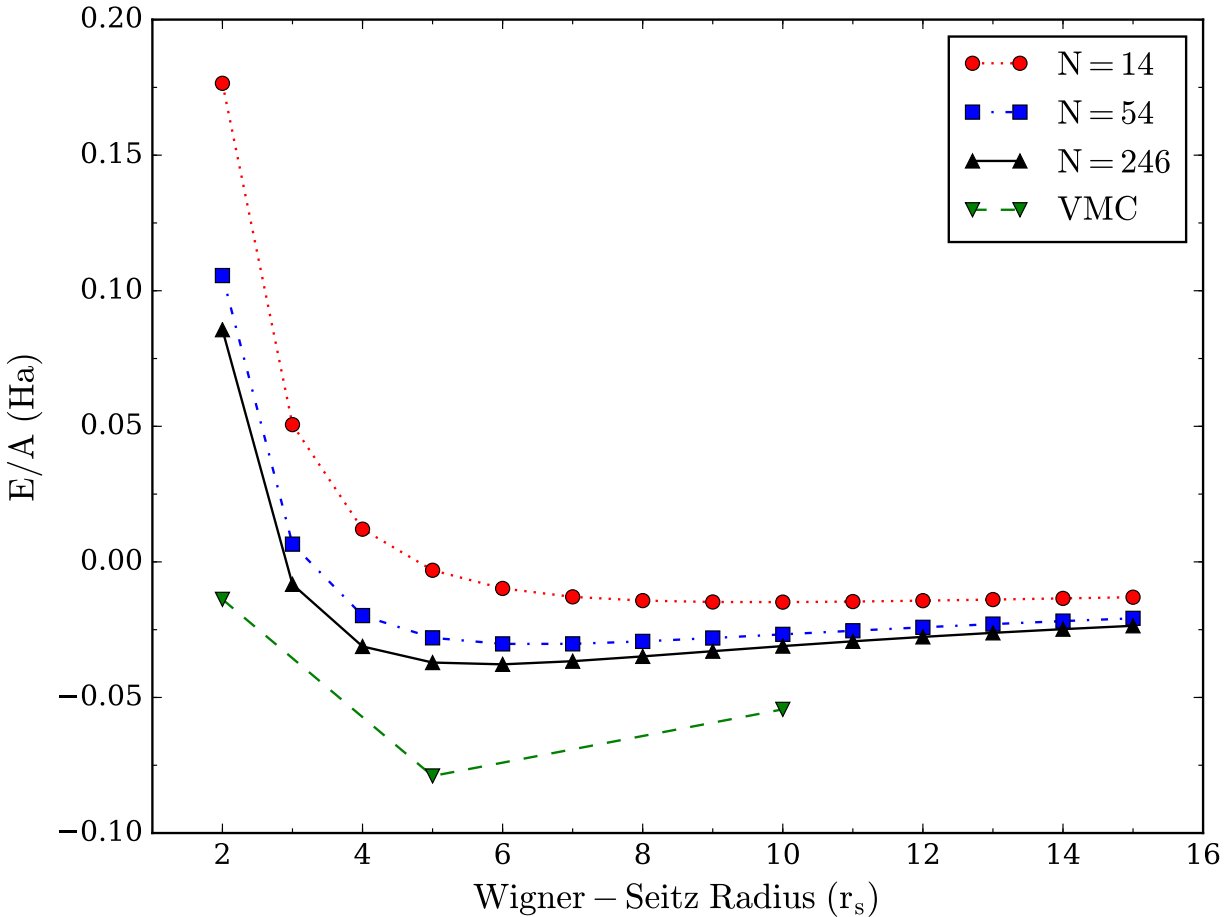


Figure 3.5: CCD energy per electron in Hartrees for the 3D homogeneous electron gas as function of the Wigner-Seitz radius in units of Bohr radii. The calculation used periodic boundary conditions and a basis with 25 shells, resulting in a total of 1238 single-particle states. Also plotted are the variational quantum Monte Carlo (VMC) results from [3].

the equation-of-state for a 3D electron gas at absolute zero. This curve can reveal many thermodynamic properties of the electron gas including the saturation density and saturation

energy, which occur at the lowest point on the curve. The CCD results are compared with the quasi-exact results from variational quantum Monte Carlo calculations from [3]. The discrepancies between the saturation energies from the two methods can be partially attributed to an insufficient basis size. However, even an appropriate extrapolation to an infinite basis won't be able to recover all of the required correlations, which suggests that CCSDT might be necessary. Regardless of the value to the saturation energy, these CCD results do qualitatively reproduce the saturation radius at $r_s \approx 5.0$.

3.6 Coupled Cluster for Finite Nuclei

The main purpose of this work is to calculate properties of atomic nuclei with coupled cluster theory. From a many-body perspective, the main process is computing the converged cluster amplitudes and thus the important correlations of the system. These amplitudes comprise the CC similarity transformation, which is versatile for constructing any effective operator, such as the Hamiltonian, that can act on the correlated system. Therefore, the first step in calculating beta-decay properties of nuclei is solving for the ground-state wave function of specific closed-shell nuclei.

3.6.1 Harmonic Oscillator Basis

Calculations of finite nuclei follow the basic structure of the algorithms used for the pairing model and the homogeneous electron gas, but they also differ in some significant ways. Like the other examples, the first step is to construct a proper single-particle basis and reference state. Because the nuclear Hamiltonian conserves angular momentum and parity, it's useful to construct orbits that are eigenfunctions of these operators. For a system with no external

potential, like the electron gas, this suggests a basis made of plane waves. However, plane waves do not represent the bound states of a nucleus very well. This property can be satisfied by introducing a fictitious external potential that mimics the mean field from the collection of nucleons. Some phenomenological potentials, like the Woods-Saxon potential, properly consider the resonance and continuum states of realistic nuclei in addition to the bound states. Many-body techniques discussed in this work have been applied to model spaces that include all three types of single-particle states [115, 116] with some success. However, for the many-body states considered in this work, it's sufficient to consider only bound single-particle states. Therefore, the nuclear basis will be constructed from the isotropic harmonic oscillator,

$$V(r) = \frac{1}{2}m\omega^2r^2. \quad (3.63)$$

An eigenstate of the harmonic oscillator potential is defined by its principal quantum number n and its orbital angular momentum quantum number l , which is denoted by the letters s, p, d, f... for the values $l = 0, 1, 2, 3\dots$ respectively. Because of spin-orbit terms in the nuclear Hamiltonian, the orbital angular momentum is coupled to a particle spin to a total angular momentum of $j = |\mathbf{l} + \mathbf{s}|$, which results in a degeneracy of $2j + 1$ for each orbit. This basis does not provide any simplification to eliminate single excitations, so CCSD will be used for all the following calculations. A schematic version of this single-particle basis is shown in Fig. 3.6. The shell structure of this basis is characterized by the energy quantum numbers, $e = 2n + l$, of the HO single-particle spectrum. This can be used to define the maximum-energy shell and the size of a HO basis with the parameter e_{\max} .

One issue with this construction, is that while the single-particle orbits are eigenstates of the angular momentum operator and localized to the external potential, they are not translationally invariant, which is required by the nuclear Hamiltonian. This means that there

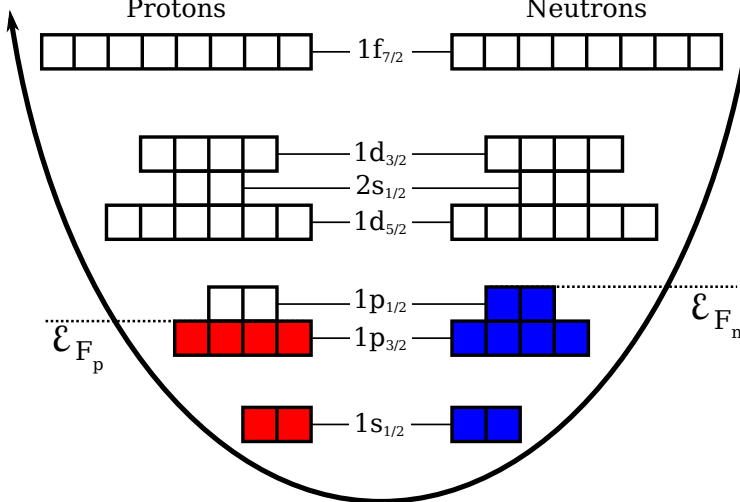


Figure 3.6: A schematic illustration of the harmonic oscillator basis used for calculations of nuclei. Shown is an example of a initial reference state for carbon-14, with 6 protons filled to the p3/2-subshell closure and 8 neutrons filled to the p1/2-shell closure. See text for details on the single-particle states.

is a fictitious center-of-mass kinetic energy which must be removed from the Hamiltonian.

The COM kinetic energy can be written as the sum of one- and two-body pieces,

$$\hat{T}_{\text{cm}} = \frac{\mathbf{P}_{\text{cm}}}{2mA} = \sum_{pq}^A \frac{\mathbf{p}_p \cdot \mathbf{p}_q}{2mA} = \sum_p^A \frac{\mathbf{p}_p^2}{2mA} + \sum_{p < q}^A \frac{\mathbf{p}_p \cdot \mathbf{p}_q}{mA}. \quad (3.64)$$

The one-body piece is just a scaled form of the original kinetic energy operator, and the two-body piece is given in a similar form to the original two-body Hamiltonian. Both can be integrated into matrix elements like Eq. (2.2),

$$\begin{aligned} {}^{(1)}T_q^p &\equiv \int d\mathbf{r}_1 \phi_p^*(\mathbf{r}_1) \frac{\mathbf{p}_1^2}{2mA} \phi_q(\mathbf{r}_1), \\ {}^{(2)}T_{rs}^{pq} &\equiv \int d\mathbf{r}_1 d\mathbf{r}_2 \phi_p^*(\mathbf{r}_1) \phi_q^*(\mathbf{r}_2) \frac{\mathbf{p}_1 \cdot \mathbf{p}_2}{mA} [\phi_r(\mathbf{r}_1) \phi_s(\mathbf{r}_2) - \phi_s(\mathbf{r}_1) \phi_r(\mathbf{r}_2)]. \end{aligned} \quad (3.65)$$

Subtracting the COM kinetic energy results in the *intrinsic* Hamiltonian for finite nuclear

systems,

$$\begin{aligned}\hat{H}_{\text{in}} = & \left(1 - \frac{1}{A}\right) \sum_{pq} {}^{(1)}T_q^p \hat{a}_p^\dagger \hat{a}_q + \frac{1}{4} \sum_{pqrs} \left({}^{(2)}H_{rs}^{pq} - {}^{(2)}T_{rs}^{pq} \right) \hat{a}_p^\dagger \hat{a}_q^\dagger \hat{a}_s \hat{a}_r \\ & + \frac{1}{36} \sum_{pqrsu} {}^{(3)}H_{stu}^{pqr} \hat{a}_p^\dagger \hat{a}_q^\dagger \hat{a}_r^\dagger \hat{a}_u \hat{a}_t \hat{a}_s + \dots,\end{aligned}\quad (3.66)$$

This form of the bare Hamiltonian (up to the three-body force) is used in the Hartree-Fock transformation. Then, after normal-ordering, the three-body piece is discarded, which is referred to as a NN+3N-induced interaction. The use of a localized external potential has further complications involving the COM wave function that are discussed in section 3.7.

A special property of this single-particle basis that can be exploited to reduce the computational complexity of the problem is the degeneracy of each orbital, due to the angular momentum projection of each single-particle state, $m_j = \{-j, -j+1, \dots, j-1, j\}$. According to the Wigner-Eckart theorem [117, 118], the geometrical component of a wave function, dependent on its projection m_j , can be isolated as a Clebsch-Gordon coefficient. Because these coefficients have compact summation rules, any diagram and corresponding sum can be written in terms of the j -orbitals instead of the single-particle m_j states, commonly known as J -scheme and M -scheme, respectively. Calculations in J -scheme require complicated angular momentum coupling, detailed in appendix D, but involve roughly an order of magnitude fewer states compared with an M -scheme calculation in the same model space.

3.6.2 The Nuclear Interaction

Perhaps the most important component in nuclear structure calculations, and also perhaps the most easily overlooked component from a many-body perspective, is the nuclear Hamiltonian. Further complicated by the composite nature of protons and neutrons, bound by

gluon exchange within the nucleon, the inter-nucleon interaction is a residual force of virtual pion exchanges and other, more exotic processes. Early *ab initio* calculations avoided this complexity by using phenomenological interactions, tuned to reproduce certain properties of a nucleus. These phenomenological forces were effectively used for calculations using shell-model CI and density-functional theory, but were restricted by the conditions of the fitted parameters.

These problems, along with the success of quantum field theories in high-energy physics, motivated the effort to describe the inter-nucleon interaction in terms of the underlying theory of the strong force, quantum chromodynamics (QCD) [119, 120]. However, while calculations of nuclei in terms of their constituent quarks using lattice QCD have made some progress with increases in computing power, they have been confined to few nucleon systems [121]. The problem is finding a way to express the high-energy QCD interactions as low-energy forces between nucleons. Such a problem, containing two vastly different scales, can be rewritten as an effective theory.

Chiral effective field theory (χ EFT), which exploits the large difference in scales between the low-energy regime of nuclear physics and the high-energy regime of QCD, is built from a general Lagrangian consistent with the broken chiral symmetry of QCD [23, 4]. This broken symmetry, a consequence of non-zero quark masses, results in several hadronic structures including protons, neutrons, and mesons, the lightest of which is the pion, $m_\pi \approx 140\text{MeV}/c^2$ [122]. This can be exploited by systematically writing a Lagrangian as the sum of pion exchanges of increasing order. Additional contact interactions, which represent exchanges of heavier mesons, are also included and must be fit to low-energy nuclear data. The hierarchy of χ EFT terms, which contain 3N and higher many-body forces, are ordered by power counting the expansion term (m_π/Λ), where Λ is an energy cutoff between the low- and high-energy

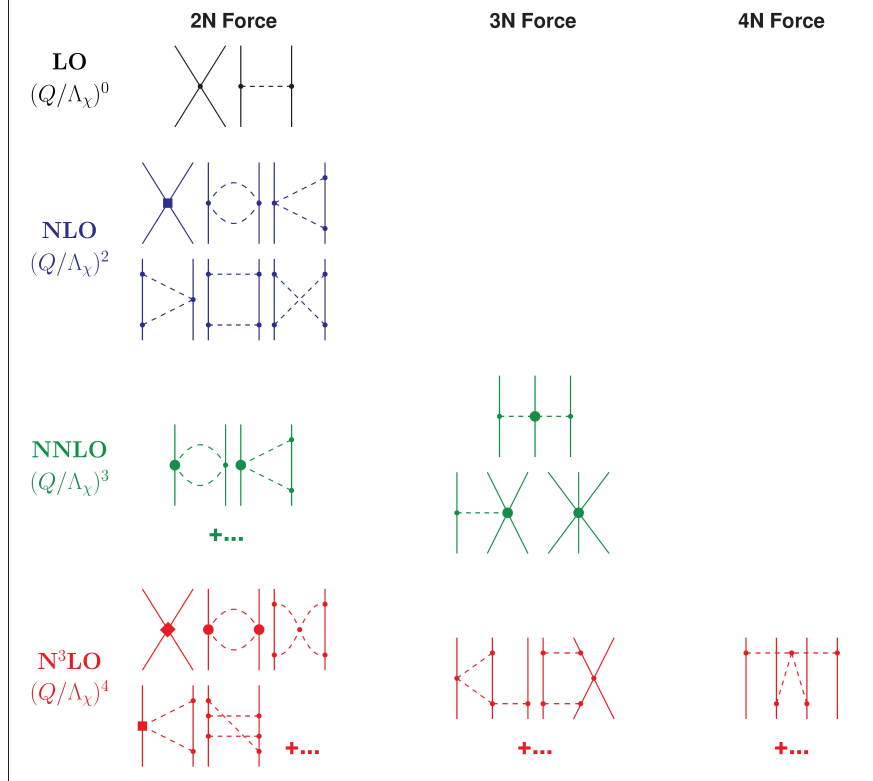


Figure 3.7: Diagrammatic form of the chiral EFT expansion up to N^3LO . The solid lines represent nucleons and the dashed lines represent pions. The different vertices represent higher-order interactions. Figure taken from [4].

scales, and is shown up to N^3LO in Fig. 3.7.

This work exclusively employs the NN force of the N^3LO interaction from Entem and Machleidt with a cutoff of $\Lambda = 500$ MeV [123]. For most calculations, this interaction is coupled with the N^2LO 3N interaction from Navrátil with a cutoff of $\Lambda = 400$ MeV [124]. This NN+3N(400) interaction is successful at reproducing low- and medium-mass nuclei, but begins to overbind beyond the *sd*-shell. As mentioned in the introduction, these bare Hamiltonians exhibit strong repulsion at short ranges among high-momentum states. Therefore to soften the interaction, the similarity renormalization group method is used to integrate high-momentum modes out of the interaction while preserving observables [25, 26].

3.6.3 Ground-State Results for Nuclei

The main object of this section is to demonstrate the validity of all the ingredients which have been discussed so far: the harmonic oscillator basis, the NN+3N(400) chiral interaction, and the J -scheme CCSD algorithm. To accomplish this, calculations for different nuclei will be compared to the corresponding experimental values. Additionally, results for different input parameters will be presented to verify that the observables are independent of non-physical variables. Once again, all results are computed with a HF-optimized basis, see section 2.5.

First, the ground-state energies should be independent of the SRG cutoff parameter λ_{SRG} . While the SRG evolution should preserve any observables, the renormalization process induces 3N and higher-body forces which can be missed by truncations of the many-body method in both the cluster amplitudes and the Hamiltonian. The trade-off here is that larger cutoff parameters produce interactions that contain higher-momentum components, which reduce a system's convergence properties, but induce fewer many-body forces, so that systems can be accurately described with fewer correlations. Conversely, a smaller cutoff parameter means that solutions can be more easily converged, but it also requires a many-body method that includes more correlations or higher-order forces [125]. To show this effect, the ground state for oxygen-16 is shown for different cutoff parameters and for both the NN and NN+3N-induced interactions. Accounting for both the small dependence on the SRG cutoff parameter and the minor inaccuracies from the truncations made to the cluster operator and the Hamiltonian, the rest of this work will use the NN+3N(400)-induced interaction with an SRG cutoff parameter of $\lambda_{\text{SRG}} = 2.0 \text{ fm}^{-1}$.

Next, any nuclear observables calculated with this framework should be independent of the fictitious confining potential. This can be verified by showing the ground-state energies of various nuclei as a function of the underlying harmonic oscillator energy, $\hbar\omega$. Convergence

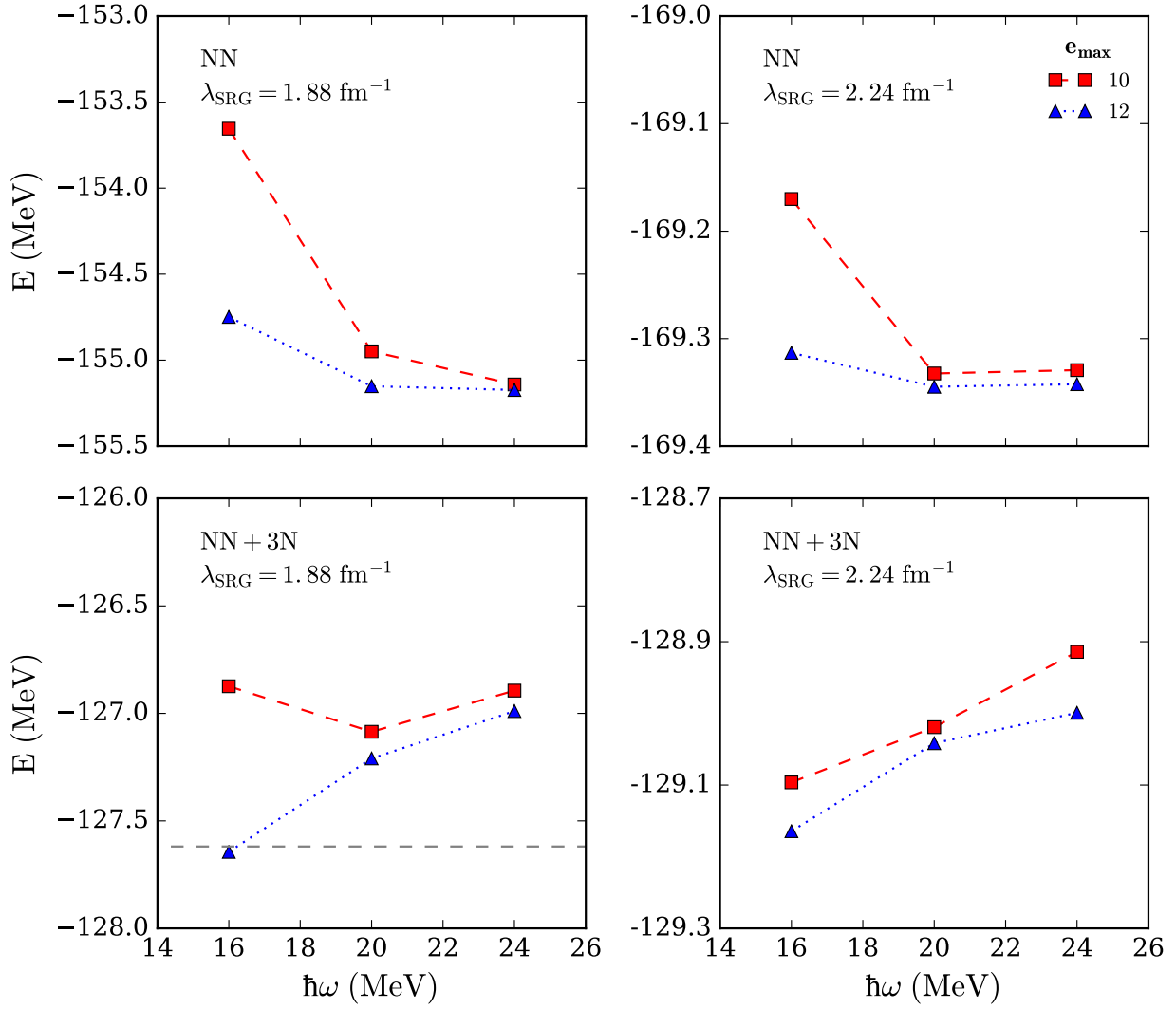


Figure 3.8: Ground-state energies for ^{16}O for the EM N³LO NN only interaction and with the added 3N interaction from Navrátil, both SRG softened with $\lambda_{\text{SRG}} = 1.88, 2.24 \text{ fm}^{-1}$. The energies are plotted for $e_{\text{max}} = 10, 12$. The most obvious difference is between the NN and NN+3N calculations, showing the importance of including 3N forces. The differences between the cutoff parameters are resolved within $\sim 1\%$ with the inclusion of 3N forces and can be rectified further by including additional correlations or full 3N forces. The experimental binding energy is shown with the grey dashed line.

is reached by increasing the size of the model space until the resulting curve is flat. Figure 3.9 shows the convergence for the *doubly-magic*, $N = Z$ nuclei, ^4He , ^{16}O , ^{20}Ca , and ^{56}Ni , where both protons and neutrons fill the same major shell closure. All the results converge to a variance of $< 1\%$ at $e_{\text{max}} = 12$ for intermediate values of $\hbar\omega$. While a larger model

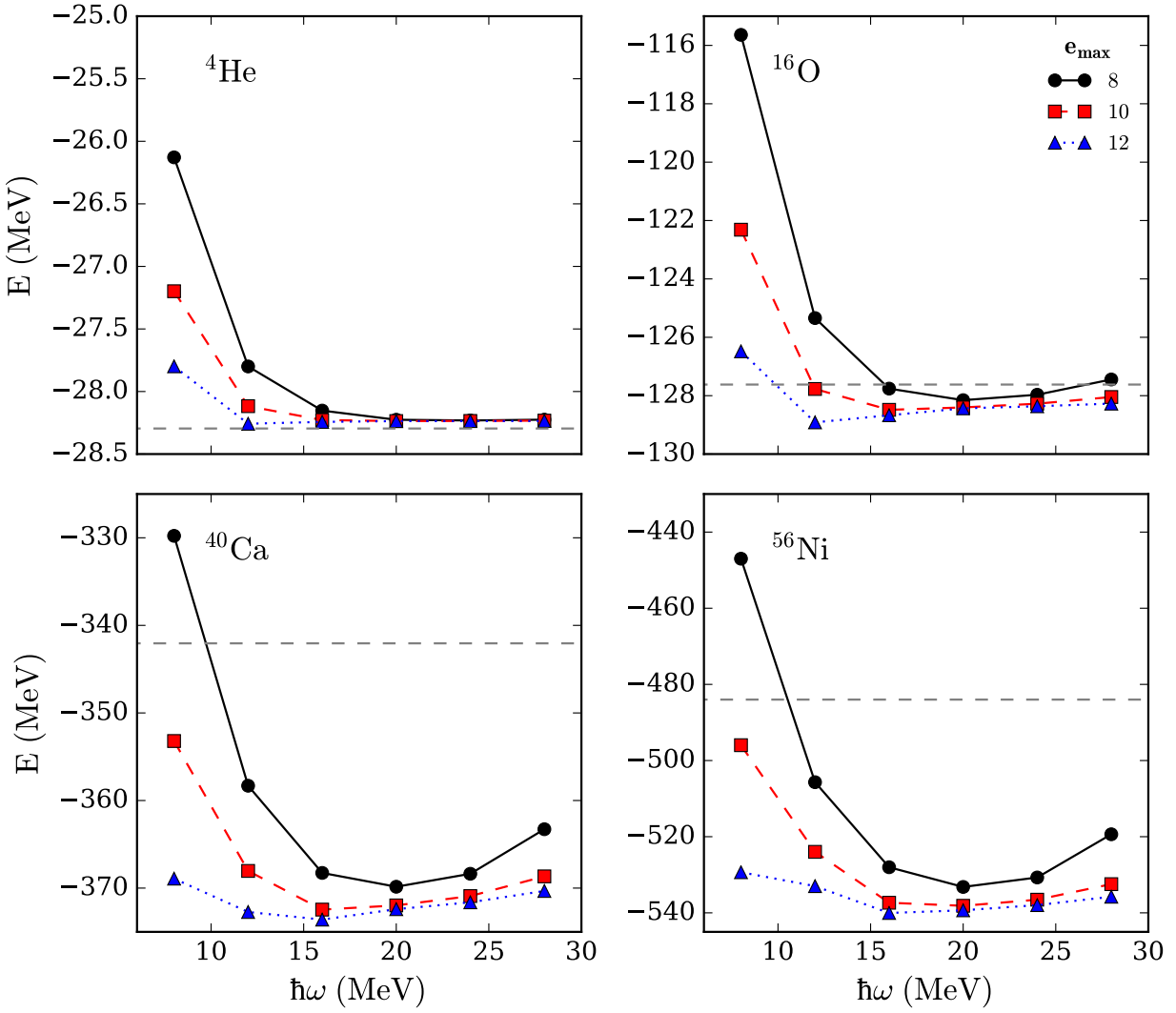


Figure 3.9: Ground-state energies for doubly magic nuclei as a function of the harmonic oscillator energy $\hbar\omega$ with the NN+3N(400) interaction, SRG softened with $\lambda_{\text{SRG}} = 2\text{fm}^{-1}$. The energies are plotted for $e_{\max} = 8, 10, 12$, showing the convergence as the model space increases. The results are independent of the underlying oscillator frequency to $\sim 1\%$ for $e_{\max} = 12$. The grey dashed line is the experimental binding energy. The overbinding of this interaction becomes apparent as the system size increases.

space is always desirable, this level of variance justifies the use of $e_{\max} = 12$ for post-CC calculations. Additionally, these results show the limitations of the NN+3N(400) interaction, as overbinding increases with the system size, where the ground-state energies of ${}^{20}\text{Ca}$ and ${}^{56}\text{Ni}$ differ from their experimental binding energies by $\sim 8\%$ and $\sim 13\%$, respectively.

The ground-state results are also shown for singly-magic nuclei, where either the protons

or neutrons fill a sub-shell closure. This has the potential complication of a vanishing energy gap between the hole and particle states, like the picture in Fig. 3.6, which causes undefined behavior in the CC algorithm (see section 3.4). However, the subshell orbitals repel each other when transformed during the Hartree-Fock algorithm [126], so these systems are valid in some cases. The ground-state energies for ^{14}C , ^{22}O , and ^{34}Si are plotted as a function of the underlying oscillator potential in Fig. 3.10. The smaller energy gap involved in these systems results in stronger excitations missed by the CCSD approximation, causing further deviations from the experimental values.

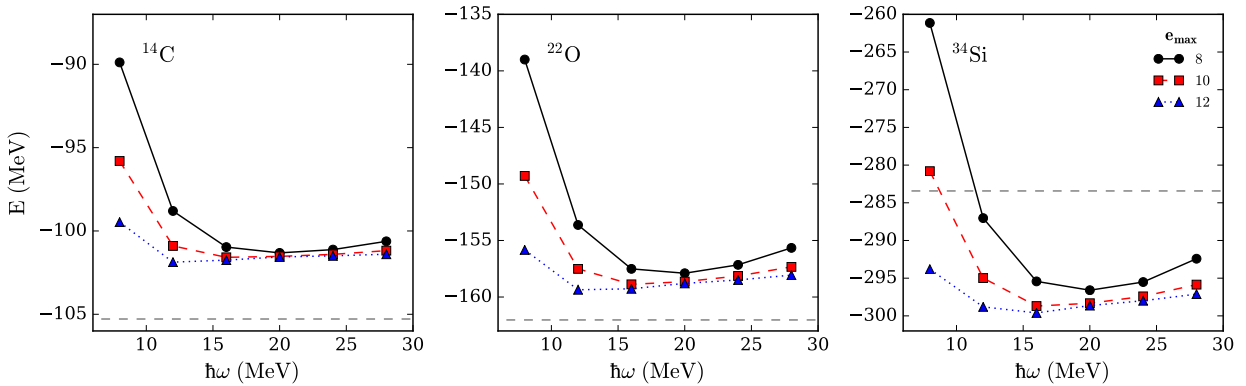


Figure 3.10: Ground-state energies for singly magic nuclei as a function of the harmonic oscillator energy $\hbar\omega$ with the NN+3N(400) interaction, SRG softened with $\lambda_{\text{SRG}} = 2\text{fm}^{-1}$. The energies are plotted for different e_{max} . The results are independent of the underlying oscillator frequency to $\sim 1\%$ for $e_{\text{max}} = 12$. The grey dashed line is the experimental binding energy. These results underbind with respect to their doubly-magic counterparts in Fig. 3.9.

3.7 Ground-State Center-of-Mass Factorization

While an intrinsic Hamiltonian can be built by removing the center-of-mass (COM) kinetic energy, Eq. (3.66), there is still an inconsistency between the translational invariance of the underlying harmonic oscillator basis and translationally-invariant nuclear many-body states [127, 128]. This inconsistency can materialize in certain calculations in the form of spurious,

non-physical states.

Of course, this problem can be avoided by using more complicated basis states that obey translational invariance, such as the use of Jacobi coordinates, but such methods are limited to few-body problems [129, 130]. Another possible solution is to use the harmonic oscillator basis in an untruncated space of Slater determinants up to a certain harmonic oscillator shell. Known as the N_{max} space, this treatment can be successfully applied within no-core shell model calculations [28]. However, the factorial scaling of this method restricts its use to light nuclei. It can be shown that in the N_{max} space, the eigenstates of the intrinsic Hamiltonian are also eigenstates of the COM Hamiltonian, and any state perfectly factorizes into a COM component and a translationally-invariant, intrinsic component,

$$|\Psi\rangle = |\Psi_{\text{in}}\rangle |\Psi_{\text{cm}}\rangle. \quad (3.67)$$

This factorization results in a compound energy spectrum, where the intrinsic component of the spectrum is degenerate for each COM excitation. Therefore, the intrinsic spectrum can be recovered by offsetting the COM Hamiltonian by the corresponding excitation energies, such that the COM energies vanish, $E_{\text{cm}} = 0$. However, with truncated methods like CCSD, this factorization is not guaranteed, and COM energies, no longer eigenenergies of the COM Hamiltonian, can take on values $E_{\text{cm}} \neq 0$. In this case, the intrinsic spectrum is contaminated with nonphysical, *spurious* states.

Because the specific form is irrelevant [131], the shifted COM Hamiltonian can be assumed to take the form of a harmonic trap with a oscillator strength of $\hbar\tilde{\omega}$, not necessarily equal to the oscillator strength of the underlying basis $\hbar\tilde{\omega}$,

$$\hat{H}_{\text{cm}}(\tilde{\omega}) = \frac{\mathbf{P}_{\text{cm}}^2}{2mA} + \frac{1}{2}mA\tilde{\omega}^2\mathbf{R}_{\text{cm}} - \frac{3}{2}\hbar\tilde{\omega}, \quad (3.68)$$

offset by the ground-state energy, $\frac{3}{2}\hbar\tilde{\omega}$. In the N_{\max} space, the factorization in Eq. (3.67) occurs regardless of $\hbar\tilde{\omega}$, while in truncated methods like CCSD, the COM oscillator strength is a free parameter which can be used to probe the level of COM contamination. If a frequency exists such that $E_{\text{cm}}(\tilde{\omega}) \approx 0$, then the wave function is approximately factorized, and the COM wave function is in its ground state [132, 133].

The COM energy, E_{cm} , can be calculated by using a version of the Hellmann-Feynman theorem by adding the COM Hamiltonian as a perturbation and computing the difference quotient [134, 135],

$$E_{\text{cm}}(\tilde{\omega}) \equiv \langle \Psi | \hat{H}_{\text{cm}} | \Psi \rangle \approx \frac{1}{2\delta} \left(\langle \Psi | \hat{H} + \delta \hat{H}_{\text{cm}}(\tilde{\omega}) | \Psi \rangle - \langle \Psi | \hat{H} - \delta \hat{H}_{\text{cm}}(\tilde{\omega}) | \Psi \rangle \right). \quad (3.69)$$

Because the operator \mathbf{R}_{cm} depends only on the underlying single-particle basis regardless of the COM oscillator frequency, it can be rewritten in terms of \hat{H}_{cm} to find the relationship between ω and $\tilde{\omega}$,

$$\frac{1}{\tilde{\omega}^2} \left(\hat{H}_{\text{cm}}(\tilde{\omega}) - \hat{T}_{\text{cm}} + \frac{3}{2}\hbar\tilde{\omega} \right) = \frac{1}{\omega^2} \left(\hat{H}_{\text{cm}}(\omega) - \hat{T}_{\text{cm}} + \frac{3}{2}\hbar\omega \right). \quad (3.70)$$

Using the known value $\langle \Psi | \hat{T}_{\text{cm}} | \Psi \rangle = \frac{3}{4}\hbar\tilde{\omega}$ and the requirement that $E_{\text{cm}}(\tilde{\omega}) = 0$ gives the following relation that relates the COM oscillator frequency to the underlying basis frequency,

$$\hbar\tilde{\omega} = \hbar\omega + \frac{2}{3}E_{\text{cm}}(\omega) \pm \sqrt{\left(\frac{2}{3}E_{\text{cm}}(\omega)\right)^2 + \frac{4}{3}\hbar\omega E_{\text{cm}}(\omega)}. \quad (3.71)$$

The ground-state COM energies are plotted for ^{16}O and ^{40}Ca using the COM Hamiltonian with two different oscillator strengths in Fig. 3.11: that of the underlying basis, $\hbar\omega$, and one of the two solutions to Eq. (3.71), $\hbar\tilde{\omega}_{\pm}$. Of the two $\hbar\tilde{\omega}_{\pm}$, which are shown as the

solutions to Eq. (3.71) in the inset, one typically results in a large COM energy while the other vanishes, which is plotted. Because the COM energies approximately vanish regardless of the underlying basis frequency, the COM wave function is in its ground state and approximately factorized from the intrinsic nuclear wave function.

Unfortunately, when intrinsic states are coupled to COM excited-states, they can contaminate the spectrum of intrinsic states that are coupled to the COM ground-state. These spurious states can be essentially removed from the ground-state spectrum with the Lawson-Gloeckner method [128]. When the proper COM oscillator strength is chosen such that the COM ground-state energy vanishes, the COM Hamiltonian can be added to the intrinsic Hamiltonian at an arbitrarily large scale, β , without changing the ground-state spectrum,

$$\hat{H}_{\text{in}} \rightarrow \hat{H}_{\text{in}} + \beta \hat{H}_{\text{cm}}. \quad (3.72)$$

When β is arbitrarily large, eigenenergies of intrinsic states coupled to COM excited states will increase by the COM energy quanta, $\beta \hbar \tilde{\omega}$, such that they are removed from the range of low-lying states of interest. The method will be used to remove spurious states from the spectra of open-shell states in section 4.

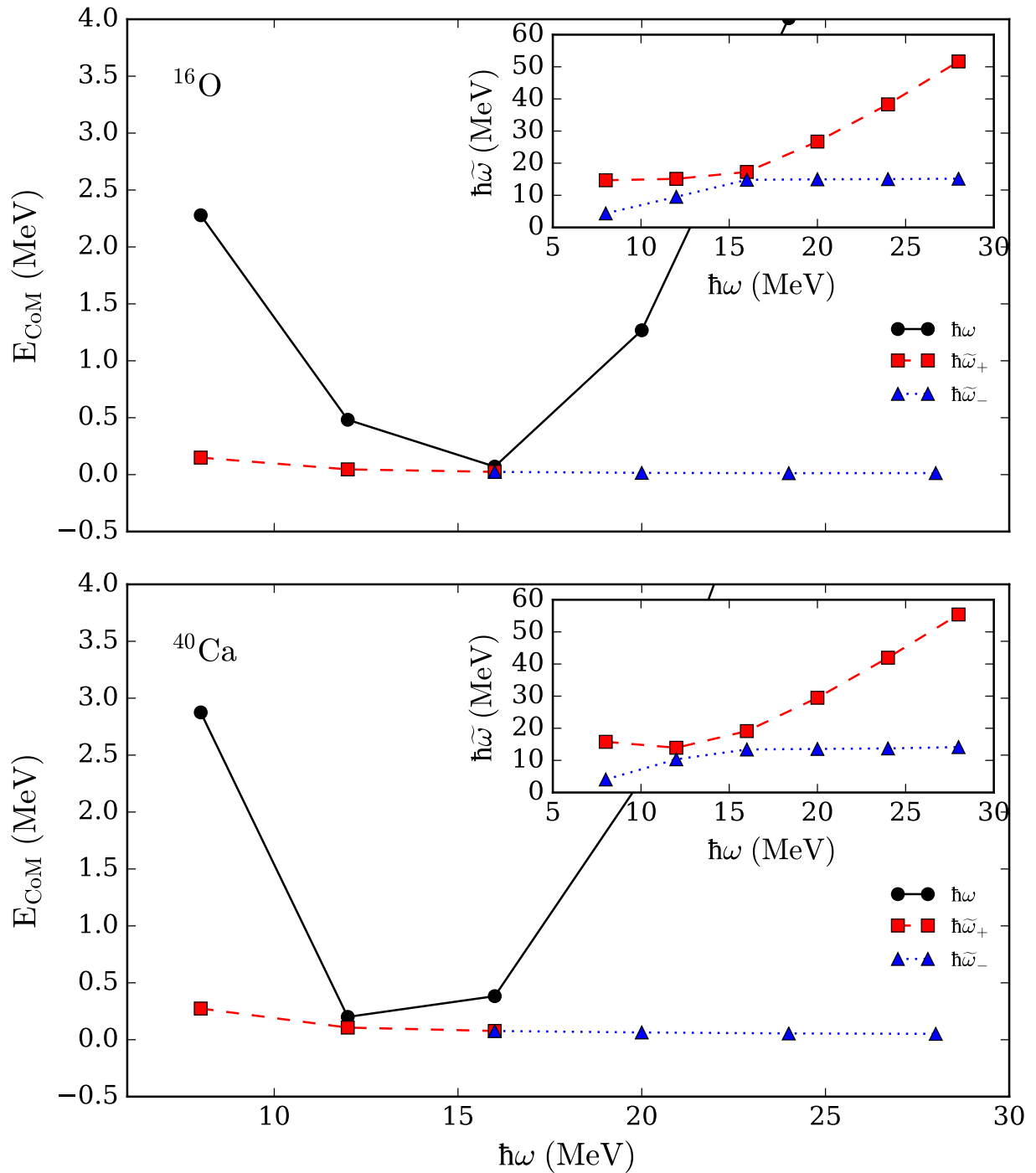


Figure 3.11: Ground-state COM energies, Eq. (3.68), for ^{16}O and ^{40}Ca at various harmonic oscillator frequencies with the NN+3N(400)-induced interaction with $\lambda_{\text{SRG}} = 2.0 \text{ fm}^{-1}$ at $e_{\text{max}} = 12$. Using the proper COM oscillator frequencies shows the approximate factorization of Eq. (3.67).

Chapter 4

Equation-of-Motion Method

Once the ground state energy and the effective Hamiltonian have been calculated, any further properties of the ground state can be calculated using the correlated wave function written as an expansion of Slater determinants in the form of Eqn. (3.1). However, many of the most interesting processes in nuclear physics involve excited-state properties. Additionally, because the coupled cluster method requires a doubly closed-shell reference state, most topics in nuclear physics that can benefit from an *ab initio* description are unreachable with the standard coupled cluster approach alone.

These restrictions motivate a class of techniques known as the *equation-of-motion* (EOM) methods [136]. Applied with the CC effective Hamiltonian, the *equation-of-motion coupled cluster* (EOM-CC) method begins with a standard CC calculation of a closed-shell ground state. Then, EOM *target states* are built onto the correlated ground-state wave function in the same way that CI states were built from the reference state, Eqn. (2.48). Unfortunately, because the CCSD similarity transformation only decouples the ground state from 1p-1h and 2p-2h excitations, these target states are still coupled to each other. Therefore, capturing the relevant correlations to describe EOM states involves a CI-like diagonalization of the effective Hamiltonian.

4.1 Equation-of-Motion States

The CC equations-of-motion states are built by applying a particular type of excitation operator to the correlated ground-state wave function in the same way that the correlated ground-state wave function was built by applying the exponential cluster operator to the reference state,

$$|\Psi_\mu\rangle = \hat{R}_\mu |\Psi\rangle = \hat{R}_\mu e^{\hat{T}} |\Phi_0\rangle. \quad (4.1)$$

The EOM excitation operator can be written as a linear combination of strings composed of particle creation operators and hole annihilation operators in increasing order, $\hat{R}_\mu = {}^{(0)}\hat{R}_\mu + {}^{(1)}\hat{R}_\mu + {}^{(2)}\hat{R}_\mu + \dots$. The form of these strings is determined by the structure of the desired target state. For example, excited states maintain the particle number of the reference state and ground state so that the constituent operator strings are $k p - k h$ operators. The A -particle excited-state EOM operator \hat{R}_μ^A is,

$$\hat{R}_\mu^A = {}^\mu r_0 + \sum_{ai} {}^\mu r_i^a \left\{ \hat{a}_a^\dagger \hat{a}_i \right\} + \frac{1}{4} \sum_{abij} {}^\mu r_{ij}^{ab} \left\{ \hat{a}_a^\dagger \hat{a}_b^\dagger \hat{a}_j \hat{a}_i \right\} + \dots, \quad (4.2)$$

where ${}^{(0)}\hat{R}_\mu = {}^\mu r_0$ represents the ground-state component of an excited state with the same conserved quantum numbers and the matrix elements, ${}^\mu r_i^a, {}^\mu r_{ij}^{ab}, \dots$, are the normal-ordered components of \hat{R}_μ .

In addition to excited states, particle-attached (PA) states can be reached by applying strings of the form p, pph, ppphh, etc. to the ground state. These operator strings increase the number of particles by one and gives the *particle-attached equation-of-motion* PA-EOM

operator $\hat{R}_\mu^{A+1} = {}^{(1)}\hat{R}_\mu^{A+1} + {}^{(2)}\hat{R}_\mu^{A+1} + \dots$,

$$\hat{R}_\mu^{A+1} = \sum_a {}^\mu r^a \left\{ \hat{a}_a^\dagger \right\} + \frac{1}{2} \sum_{abi} {}^\mu r_i^{ab} \left\{ \hat{a}_a^\dagger \hat{a}_b^\dagger \hat{a}_i \right\} + \dots \quad (4.3)$$

Lastly, particle-removed (PR) states can be reached by applying strings of the form $h, hhp, hhpp,$ etc. to the ground state. These operator strings decrease the number of particles by one and give the *particle-removed equation-of-motion* PR-EOM operator $\hat{R}_\mu^{A-1} = {}^{(1)}\hat{R}_\mu^{A-1} + {}^{(2)}\hat{R}_\mu^{A-1} + \dots$,

$$\hat{R}_\mu^{A-1} = \sum_i {}^\mu r_i \left\{ \hat{a}_i \right\} + \frac{1}{2} \sum_{a ij} {}^\mu r_{ij}^a \left\{ \hat{a}_a^\dagger \hat{a}_j^\dagger \hat{a}_i \right\} + \dots \quad (4.4)$$

With these target states, the Schrödinger equation can be written by applying the Hamiltonian to Eq. (4.1),

$$\begin{aligned} \hat{H}|\Psi_\mu\rangle &= E_\mu |\Psi_\mu\rangle, \\ \hat{H}\hat{R}_\mu e^{\hat{T}}|\Phi_0\rangle &= E_\mu \hat{R}_\mu e^{\hat{T}}|\Phi_0\rangle. \end{aligned} \quad (4.5)$$

This equation can be written in terms of the effective Hamiltonian by multiplying with the operator $e^{-\hat{T}}$,

$$e^{-\hat{T}} \hat{H}\hat{R}_\mu e^{\hat{T}}|\Phi_0\rangle = E_\mu e^{-\hat{T}} \hat{R}_\mu e^{\hat{T}}|\Phi_0\rangle. \quad (4.6)$$

Because both \hat{R}_μ and \hat{T} are excitation operators, containing only particle creation operators and hole annihilation operators, no nonzero contractions can occur between them (see section 2.4). This means that the order of the two operators is inconsequential such that they commute with each other ($\hat{R}_\mu \hat{T} = \hat{T} \hat{R}_\mu$), which is also true for the exponential cluster operator ($\hat{R}_\mu e^{\hat{T}} = e^{\hat{T}} \hat{R}_\mu$). This property can be used to rewrite Eq. (4.6) in terms of the

effective Hamiltonian,

$$\begin{aligned} e^{-\hat{T}} \hat{H} e^{\hat{T}} \hat{R}_\mu |\Phi_0\rangle &= E_\mu e^{-\hat{T}} e^{\hat{T}} \hat{R}_\mu |\Phi_0\rangle \\ \bar{H} \hat{R}_\mu |\Phi_0\rangle &= E_\mu \hat{R}_\mu |\Phi_0\rangle. \end{aligned} \quad (4.7)$$

Using the normal-ordered Hamiltonian, the equation can be rewritten as,

$$\bar{H}_N \hat{R}_\mu |\Phi_0\rangle = \Delta E_\mu \hat{R}_\mu |\Phi_0\rangle. \quad (4.8)$$

Up to this point, extending the CC method from the ground state to excited and open-shell states amounts to an energy eigenvalue problem involving the normal-ordered effective Hamiltonian and the EOM excitation operators \hat{R}_μ . The signature component of EOM methods is reached by multiplying the normal-ordered ground-state Schrödinger equation, Eq. (2.4), with \hat{R}_μ and subtracting the result from Eq. (4.8),

$$\left(\bar{H}_N \hat{R}_\mu - \hat{R}_\mu \bar{H}_N \right) |\Phi_0\rangle = (\Delta E_\mu - \Delta E) \hat{R}_\mu |\Phi_0\rangle. \quad (4.9)$$

The right-hand side of this equation can be rewritten as the commutator $[\bar{H}_N, \hat{R}_\mu]$ and the energy difference can be defined as $\omega_\mu \equiv \Delta E_\mu - \Delta E$ so that the fundamental EOM equation is,

$$[\bar{H}_N, \hat{R}_\mu] |\Phi_0\rangle = \omega_\mu \hat{R}_\mu |\Phi_0\rangle. \quad (4.10)$$

The name *equation-of-motion* refers to the resemblance of this equation with the commutator-based Heisenberg representation of quantum mechanics. The objective behind this formulation is to reduce the dependence of EOM states on the ground state by removing common terms between them. This reduction is accomplished by noticing that, like the commutator

between \bar{H}_N and \hat{R}_μ , the commutator between uncontracted terms of $[\bar{H}_N, \hat{R}_\mu]$ vanishes. This simplifies the commutator in Eq. (4.11) to only connected terms just as the effective Hamiltonian was simplified in Eq. (3.8),

$$\left(\bar{H}_N \hat{R}_\mu \right)_c | \Phi_0 \rangle = \omega_\mu \hat{R}_\mu | \Phi_0 \rangle. \quad (4.11)$$

Equation (4.6) constitutes a generalized eigenvalue problem which solves for the components of the EOM operator, ${}^\mu r$, and the energy difference, ω_μ . If only the energy of excited or open shell states are required, solving this equation is sufficient for such a task. However, computing properties of EOM states requires the Hermitian conjugate of the EOM operator \hat{R}_μ^\dagger , and as encountered before, the non-Hermiticity of the effective Hamiltonian complicates this effort.

4.2 Dual Solutions

Because the CC effective Hamiltonian is non-Hermitian ($\bar{H}_N^\dagger \neq \bar{H}_N$), the eigenvalue problem in Eq. (4.8) has a corresponding left-eigenvalue problem,

$$\langle \Phi_0 | \hat{L}_\mu \bar{H}_N = \langle \Phi_0 | \hat{L}_\mu \Delta E_\mu. \quad (4.12)$$

The operators \hat{L}_μ are de-excitation operators analogous to the corresponding right operators \hat{R}_μ . The left EOM operator for particle-attached states has the form,

$$\hat{L}_\mu^{A+1} = \sum_a {}^\mu l_a \{ \hat{a}_a \} + \frac{1}{2} \sum_{abi} {}^\mu l_{ab}^i \left\{ \hat{a}_i^\dagger \hat{a}_b \hat{a} \right\} + \dots, \quad (4.13)$$

and the left EOM operator for particle-removed states has the form,

$$\hat{L}_\mu^{A-1} = \sum_i {}^\mu l^i \left\{ \hat{a}_i^\dagger \right\} + \frac{1}{2} \sum_{aij} {}^\mu l_a^{ij} \left\{ \hat{a}_i^\dagger \hat{a}_j^\dagger \hat{a}_a \right\} + \dots . \quad (4.14)$$

Again, the matrix elements ${}^\mu l$ are the normal-ordered components of \hat{L}_μ and map to a corresponding ${}^\mu r$. Because there is not a corresponding left eigenvalue problem for the ground state in the form of Eq. (2.4), the EOM eigenvalue problem for \hat{L}_μ cannot be reduced to the form of Eq. (4.11). This amounts to calculating additional non-contracted terms between the Hamiltonian and the left EOM state and computing the energy difference directly from $\omega_\mu \equiv \Delta E_\mu - \Delta E$.

The corresponding right and left EOM operators form a bi-orthogonal basis such that,

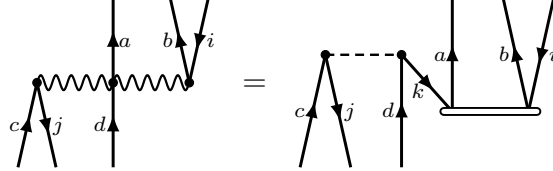
$$\langle \Phi_0 | \hat{L}_\mu \hat{R}_\nu | \Phi_0 \rangle = \delta_{\mu\nu}. \quad (4.15)$$

When this condition is fulfilled, any scaling of the right and left solutions by the factors α and $1/\alpha$, respectively, also fulfills the condition. Therefore, because the normalization of each solution is not determined uniquely, both solutions must be used when computing properties of EOM states. This is accomplished by applying the bi-orthogonal solutions as the identity operator,

$$\hat{1} = \sum_\mu \hat{R}_\mu | \Phi_0 \rangle \langle \Phi_0 | \hat{L}_\mu. \quad (4.16)$$

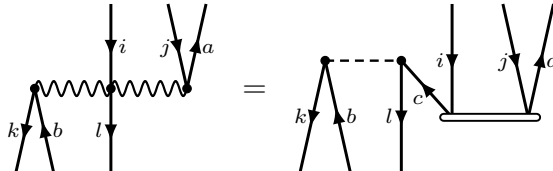
4.2.1 Induced Three-Body Interaction

Before solving the EOM equations, it's beneficial to introduce relevant three-body effective Hamiltonian terms which will be used in Eqs. (4.11) and (4.12). While the original three-body Hamiltonian was only used for the normal-ordered zero- and one-body pieces, the CC similarity transformation induces higher-body interactions from contractions between the Hamiltonian and the cluster operators, see Eq. (3.8). In the CCSD approximation, the four-body interaction is the highest-order term, generated from the contraction of the Hamiltonian with the term $\frac{1}{2}\hat{T}_1^2$. Fortunately, the PA-EOM-CCSD and PR-EOM-CCSD methods only include certain three-body interactions, which are shown below. The effective hpphpp three-body interaction can couple two particle-attached operators of the form $\mu r_i^{ab} \left\{ \hat{a}_a^\dagger \hat{a}_b^\dagger \hat{a}_i \right\}$ and is generated from a term of the form $\hat{V}\hat{T}_2$,



$$X_{jcd}^{iab} = - \sum_k V_{cd}^{jk} t_{ki}^{ab}. \quad (4.17)$$

Likewise, the effective hhphhp three-body interaction couples two particle-removed operators of the form $\mu r_{ij}^a \left\{ \hat{a}_a^\dagger \hat{a}_j \hat{a}_i \right\}$,



$$X_{ijb}^{kla} = \sum_k V_{cd}^{jk} t_{ki}^{ab}. \quad (4.18)$$

Because the pphpph structure in Eq. (4.17) scales as $\mathcal{O}(n_h^2 n_p^4)$, it can quickly overtake a calculation's memory allocation. Therefore, these structures are never actually built. Instead, the different components are summed as special intermediates when they are needed during PA-EOM-CC or PR-EOM-CC calculations.

4.3 Solving the EOM equations

At this point, after solving for the CC ground-state wave function with a truncated cluster operator, a full accounting of the remaining many-body correlations would scale factorially like the full CI method, see section 2.6 and Fig. 2.3. Therefore it's necessary to truncate the EOM operators with the assumptions that the lower-order excitations will dominate the EOM states. In this work, the particle-attached and particle-removed operators are truncated at the 2p-1h and 1p-2h levels, respectively, which is referred to as the EOM(2) truncation. Like other effective *ab initio* methods, this approximation can be systematically improved by including higher-order terms. For the PA-EOM(2) method, the EOM operators have the form,

$$\begin{aligned}\hat{R}_\mu^{A+1} &= \sum_a {}^\mu r^a \left\{ \hat{a}_a^\dagger \right\} + \frac{1}{2} \sum_{abi} {}^\mu r_i^{ab} \left\{ \hat{a}_a^\dagger \hat{a}_b^\dagger \hat{a}_i \right\} \quad \text{and} \\ \hat{L}_\mu^{A+1} &= \sum_a {}^\mu l_a \left\{ \hat{a}_a \right\} + \frac{1}{2} \sum_{abi} {}^\mu l_{ab}^i \left\{ \hat{a}_i^\dagger \hat{a}_b \hat{a} \right\}.\end{aligned}\quad (4.19)$$

Likewise, the PR-EOM(2) method, the EOM operators have the form,

$$\begin{aligned}\hat{R}_\mu^{A-1} &= \sum_i {}^\mu r_i \{\hat{a}_i\} + \frac{1}{2} \sum_{a i j} {}^\mu r_{i j}^a \left\{ \hat{a}_a^\dagger \hat{a}_j \hat{a}_i \right\} \quad \text{and} \\ \hat{L}_\mu^{A-1} &= \sum_i {}^\mu l^i \left\{ \hat{a}_i^\dagger \right\} + \frac{1}{2} \sum_{a i j} {}^\mu l_a^{i j} \left\{ \hat{a}_i^\dagger \hat{a}_j^\dagger \hat{a}_a \right\}.\end{aligned}\quad (4.20)$$

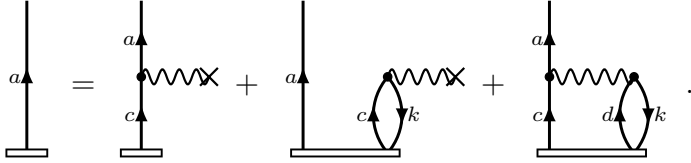
The EOM matrix eigenvalue equation can be solved in a computationally practical way with power-iteration methods. Traditionally, the Lanczos algorithm is used to produce the lowest energy eigenvalues and their corresponding eigenvectors from a Hermitian matrix [137]. In this case, with a non-Hermitian matrix, the generalized Arnoldi algorithm [138] is used instead. These methods remove the need to build the entire matrix, $\langle \Phi_0 | \hat{L}_\mu \bar{H}_N \hat{R}_\mu | \Phi_0 \rangle$, to be diagonalized, instead relying on matrix-vector products performed as a step in an iterative process. In this work the iterative procedure was implemented with the numerical software library ARPACK [139]. The matrix is simply the effective normal-ordered Hamiltonian \bar{H}_N and the vectors are EOM operators. Like the coupled cluster equations, this matrix-vector product is best computed with diagrammatic techniques and are shown below.

The matrix-vector product for the right eigenvalue problem of the PA-EOM(2) method consists of two components which can be seen clearly by left-multiplying Eq. (4.11) with the particle-attached bra states, $\langle \Phi^a |$ and $\langle \Phi_i^{ab} |$, respectively. This has the effect of projecting out the corresponding components ${}^\mu r$,

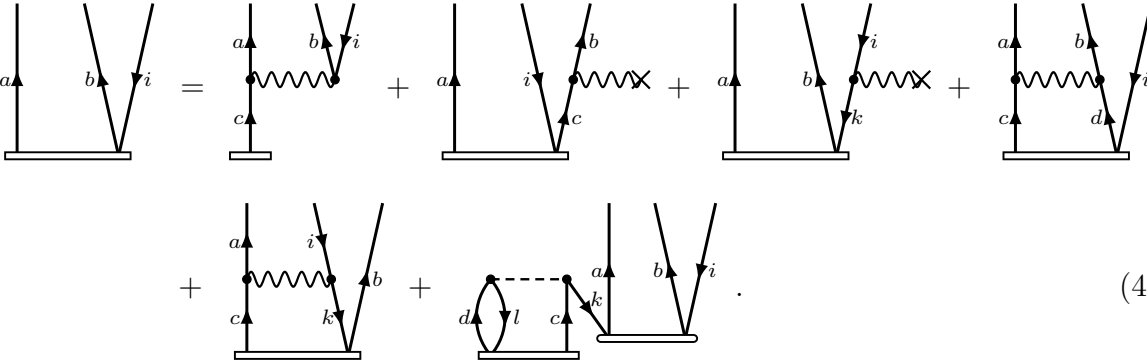
$$\langle \Phi^a | \left(\bar{H}_N \hat{R}_\mu \right)_c | \Phi_0 \rangle = \omega_\mu {}^\mu r^a, \quad (4.21)$$

$$\langle \Phi_i^{ab} | \left(\bar{H}_N \hat{R}_\mu \right)_c | \Phi_0 \rangle = \omega_\mu {}^\mu r_i^{ab}. \quad (4.22)$$

Like the coupled-cluster equations, the EOM equations are best derived with diagrammatic techniques. For these purposes, the right EOM excitation operators are depicted by the vertex type  . Equation (4.21) generates the following expressions and corresponding diagrams, suppressing the state identifier μ for clarity,

$$\omega r^a = \sum_c X_c^a r^c + \sum_{kc} X_c^k r_k^{ac} + \frac{1}{2} \sum_{kcd} X_{cd}^{ak} r_k^{cd}$$

(4.23)

The corresponding expressions and diagrams for Eq. (4.22) are,

$$\begin{aligned} \omega r_i^{ab} &= \sum_c X_{ci}^{ab} r^c + \hat{P}(ab) \sum_c X_c^b r_i^{ac} - \sum_k X_i^k r_k^{ab} + \frac{1}{2} \sum_{cd} X_{cd}^{ab} r_i^{cd} \\ &\quad - \hat{P}(ab) \sum_{kc} X_{ci}^{ak} r_k^{cb} - \frac{1}{2} \sum_{klcd} V_{cd}^{kl} t_{ki}^{ab} r_l^{cd} \end{aligned}$$

(4.24)

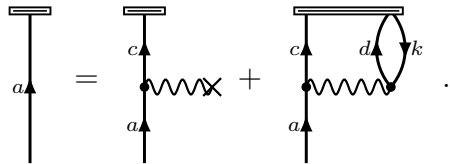
The vector-matrix product for the left eigenvalue problem of the PA-EOM(2) method also consists of two components achieved in a similar fashion by right-multiplying Eq. (4.12) with the particle-attached ket states, $\langle \Phi^a |$ and $\langle \Phi_i^{ab} |$, respectively, which has the effect of

projecting out the corresponding components ${}^\mu l$,

$$\langle \Phi_0 | \hat{L}_\mu \bar{H}_N | \Phi^a \rangle = \Delta E_\mu {}^\mu l_a, \quad (4.25)$$

$$\langle \Phi_0 | \hat{L}_\mu \bar{H}_N | \Phi_i^{ab} \rangle = \Delta E_\mu {}^\mu l_{ab}^i. \quad (4.26)$$

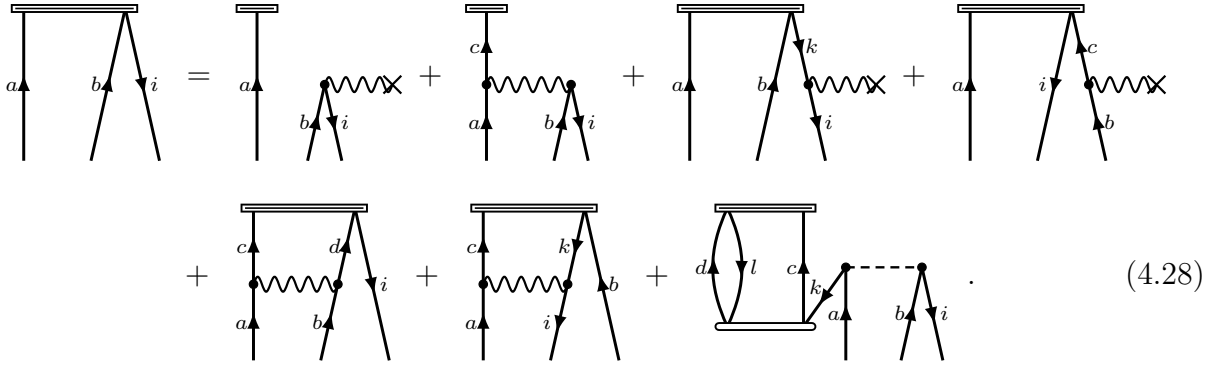
Because Eqns. (4.25) and (4.26) do not use commutators between \bar{H}_N and \hat{L}_μ , the diagrams which describe these equations include disconnected diagrams and corresponding expressions with matrix elements that share no indices. For these diagrams, the left EOM de-excitation operators are depicted by the vertex type . Equation (4.25) generates the following expressions and diagrams, again suppressing the state identifier μ ,

$$El_a = \sum_c l_c X_a^c + \frac{1}{2} \sum_{kcd} l_{cd}^k X_{ak}^{cd}$$

(4.27)

The corresponding expressions and diagrams for Eq. (4.26) are,

$$El_{ab}^i = \hat{P}(ab) l_a X_b^i + \sum_c l_c X_{ab}^{ci} - \sum_k l_{ab}^k X_k^i + \hat{P}(ab) \sum_c l_{ac}^i X_b^c$$

$$+ \frac{1}{2} \sum_{cd} l_{cd}^i X_{ab}^{cd} - \hat{P}(ab) \sum_{kc} l_{cb}^k X_{ak}^{ci} - \frac{1}{2} \sum_{klcd} l_{cd}^l V_{ab}^{ki} t_{kl}^{cd}$$



The particle-removed equations are generated in exactly the same way. The matrix-vector product for the right eigenvalue problem of the PR-EOM(2) method consists of two components corresponding to the particle-removed bra states, $\langle \Phi_i |$ and $\langle \Phi_{ij}^a |$, respectively,

$$\langle \Phi_i | \left(\bar{H}_N \hat{R}_\mu \right)_c | \Phi_0 \rangle = \omega_\mu^\mu r_i, \quad (4.29)$$

$$\langle \Phi_{ij}^a | \left(\bar{H}_N \hat{R}_\mu \right)_c | \Phi_0 \rangle = \omega_\mu^\mu r_{ij}^a. \quad (4.30)$$

Equation (4.29) generates the following expressions and diagrams,

$$\omega r_i = - \sum_k X_i^k r_k + \sum_{kc} X_c^k r_{ik}^c - \frac{1}{2} \sum_{klc} X_{ic}^{kl} r_{kl}^c$$

The corresponding expressions and diagrams for Eq. (4.30) are,

$$\begin{aligned}
\omega_k r_{ij}^a &= - \sum_k X_{ij}^{ka} r_k - \hat{P}(ij) \sum_k X_j^k r_{ik}^a + \sum_c X_c^a r_{ij}^c + \frac{1}{2} \sum_{kl} X_{ij}^{kl} r_{kl}^a \\
&\quad - \hat{P}(ij) \sum_{kc} X_{ci}^{ak} r_{kj}^c - \frac{1}{2} \sum_{klcd} V_{cd}^{kl} t_{ij}^{ca} r_{kl}^d
\end{aligned}$$

Finally, the vector-matrix product for the left eigenvalue problem of the PA-EOM(2) method consists of two components which correspond with the particle-removed ket states, $\langle \Phi_i |$ and $\langle \Phi_{ij}^a |$, respectively,

$$\langle \Phi_0 | \hat{L}_\mu \bar{H}_N | \Phi_i \rangle = \Delta E_\mu^\mu l^i, \quad (4.33)$$

$$\langle \Phi_0 | \hat{L}_\mu \bar{H}_N | \Phi_{ij}^a \rangle = \Delta E_\mu^\mu l_a^{ij}. \quad (4.34)$$

Again, Eqns. (4.33) and (4.34) do not remove disconnected diagrams with commutators

between \bar{H}_N and \hat{L}_μ . Equation (4.33) generates the following expressions and diagrams,

$$El^i = - \sum_k l^k X_k^i - \frac{1}{2} \sum_{klc} l_c^{kl} X_{kl}^{ic}$$
(4.35)

The corresponding expressions and diagrams for Eq. (4.34) are,

$$\begin{aligned} E_k l_a^{ij} &= \hat{P}(ij) l^i X_a^j - \sum_k l^k X_{ka}^{ij} + \sum_c l_c^{ij} X_a^c - \hat{P}(ij) \sum_k l_a^{ik} X_k^j \\ &\quad + \frac{1}{2} \sum_{cd} l_a^{kl} X_{kl}^{ij} - \hat{P}(ij) \sum_{kc} l_c^{kj} X_{ak}^{ci} - \frac{1}{2} \sum_{klcd} l_d^{kl} V_{ca}^{ij} t_{kl}^{cd} \end{aligned}$$
(4.36)

These expressions must be computed for every iteration of the Arnoldi algorithm and contain expensive sums that can benefit from the techniques of section 3.4. The major difference in this case is that while the cluster operators and the Hamiltonian are scalar operators that define the conserved quantum numbers of a symmetry channel, see section 3.4.1, the EOM operators are tensor operators that carry their own quantum numbers and can change the symmetry of the reference state to that of the target state.

4.4 EOM-CC for 2D Quantum Dots

To examine some properties of the EOM-CC method, it's useful to focus on the results from the two-dimensional quantum dot. This system, also known as an “artificial atom”, consists of A electrons confined within a 2D harmonic oscillator and subject to the inter-electron Coulomb force. These nanoscale structures are easily tunable which makes them relevant for probing many different quantum phenomena in experiments and theoretical models [140, 141, 142], and because the quantum dot shell structure is similar to those of atomic nuclei, they provide a useful system to quantify the impact of quantum effects at different levels of correlation [143].

4.4.1 Quantum Dot Formalism

The circular quantum dot system is characterized by a harmonic-oscillator potential of the form $V(r) = m\omega^2 r^2/2$, where ω is its angular frequency, r is the radial distance from the center, and m is the electron mass. The single-particle states can be constructed as eigenfunctions of the 2D quantum harmonic oscillator,

$$\left(\frac{-\hbar^2}{2m} \nabla^2 + \frac{1}{2} m\omega^2 r^2 \right) \phi_{nm\ell\sigma}(\mathbf{r}) = \epsilon_{nm\ell} \phi_{nm\ell\sigma}(\mathbf{r}). \quad (4.37)$$

These states are characterized by a radial quantum number n , a spin quantum number σ , and because this systems conserves orbital angular momentum, a corresponding angular momentum projection number, m_ℓ . The energy of each single-particle state $\phi_{nm\ell\sigma}(\mathbf{r})$, independent of the spin quantum projection, is given by,

$$\epsilon_{nm\ell} \equiv (2n + |m_\ell| + 1)\omega. \quad (4.38)$$

In addition to the spin projection σ , they are degenerate with respect to the *shell index* k ,

$$k \equiv 2n + |m_\ell|, \quad (4.39)$$

which labels each shell from zero with a total number of shells, K . The shell structure is illustrated in Fig. 4.1.

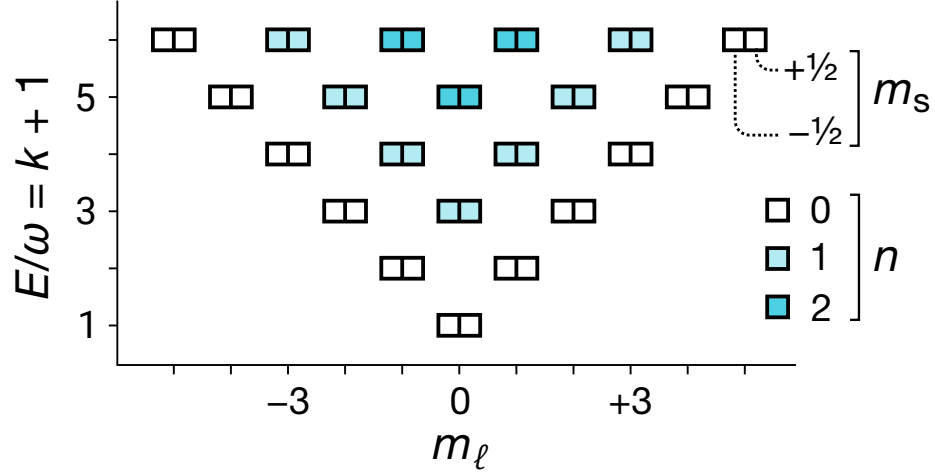


Figure 4.1: The 42 lowest single-particle states (the first 5 shells) in the 2D harmonic oscillator basis. Each box represents a single-particle state arranged by m_ℓ , m_s , and energy, and the up/down arrows indicate the spin of the states. Within each column, the principal quantum number n increases as one traverses upward.

The specific form of these basis states can be solved with the cylindrically symmetric Fock–Darwin states F_{nm_ℓ} , which conserve the orbital angular momentum projection $\hat{L}_z \equiv -i\frac{\partial}{\partial\varphi}$. Apart from their spin component, the states are defined as [144],

$$F_{nm_\ell}(\rho, \varphi) \equiv \sqrt{\omega} R_{n|m_\ell|}(\sqrt{\omega}\rho) \times \frac{1}{\sqrt{2\pi}} e^{im_\ell\varphi}, \quad \text{where} \quad (4.40)$$

$$R_{nm}(\varrho) \equiv \sqrt{\frac{2 \times n!}{(n+m)!}} e^{-\varrho^2/2} \varrho^m L_n^{(m)}(\varrho^2)$$

and $L_n^{(\alpha)}$ denotes the generalized Laguerre polynomial [145] of degree n and parameter α .

Like the homogeneous electron gas, (see section 3.5), the electrons in the quantum dot interact with each other through the standard Coulomb interaction, $V(\mathbf{r}_1, \mathbf{r}_2) = 1/|\mathbf{r}_1 - \mathbf{r}_2|$, which is expressed in atomic units where $m = c = e = (4\pi\epsilon_0)^{-1} = 1$. With the form of the single-particle wave functions, the second-quantized form of the two-body interaction can be analytically calculated,

$${}^{(2)}H_{rs}^{pq} \equiv \int d\mathbf{r}_1 d\mathbf{r}_2 \phi_p^*(\mathbf{r}_1)\phi_q^*(\mathbf{r}_2) \frac{1}{|\mathbf{r}_1 - \mathbf{r}_2|} [\phi_r(\mathbf{r}_1)\phi_s(\mathbf{r}_2) - \phi_s(\mathbf{r}_1)\phi_r(\mathbf{r}_2)], \quad (4.41)$$

where $\phi_p(\mathbf{r})$ is shorthand for $\phi_{n_p m_{\ell_p} \sigma_p}(\mathbf{r})$.

With these ingredients in hand, the ground state energy, as well as particle-attached and particle-removed energies, can be calculated for different values of the oscillator frequency, ω , and the number of shells, K .

4.4.2 Quantum Dot Results

Here, CC results are shown along with results from the in-medium similarity renormalization group (IM-SRG) method, and quasi-degenerate perturbation theory (QDPT) [146]. As for all calculations in this work, each method applies a Hartree-Fock transformation of the basis states from Eq. (4.37) before employing the primary many-body method. Before analyzing the EOM results, the ground state energies calculated using CCSD and IM-SRG(2) are shown in Fig. 4.2. Also included are results from Møller-Plesset perturbation theory to second order (MP2), DMC [147], and full CI [148] for comparison where available.

With respect to the number of shells, both IM-SRG(2) and CCSD appear to converge slightly faster than second order perturbation theory (MP2), mainly due to the presence of higher order corrections in IM-SRG(2) and CCSD. However, the main conclusion that

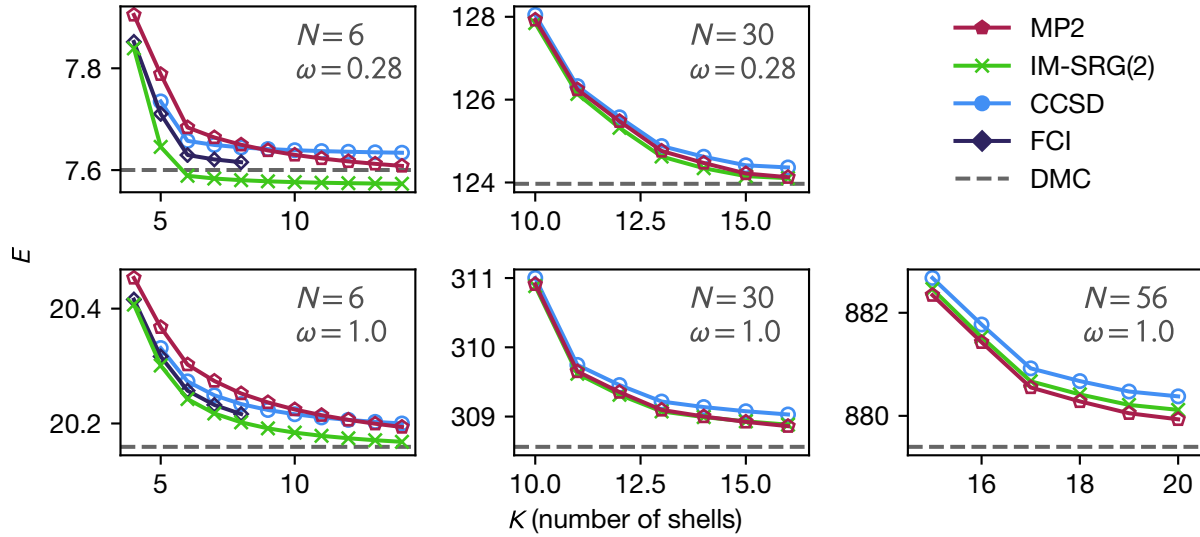


Figure 4.2: Ground state energy (in Hartrees) of quantum dots with N particles and an oscillator frequency of ω calculated with several different methods.

can be reached from Fig. 4.2 is the overall convergence between vastly different methods, a hallmark of properly-treated *ab initio* methods.

Additionally, the results for addition and removal energy calculations are summarized in Fig. 4.3 and Fig. 4.4 respectively. Not only do these results reaffirm the validity of the CCSD method amongst other *ab initio* methods, they also provide benchmark calculations for the following CC-EOM calculations of open-shell finite nuclei.

4.5 Quality of EOM Solutions

Applying the CC similarity transformation to the Hamiltonian implicitly re-sums contributions from higher order excitations beyond the EOM(2)-CC truncation (3p-2h, 4p-3h, ... for PA-EOM and 2p-3h, 3p-4h, ... for PR-EOM) into the lower-order excitations which comprise the EOM(2)-CC operators (1p-0h, 2p-1h, ... for PA-EOM and 0p-1h, 1p-2h, ... for PR-EOM). This means that EOM states are weighted towards few-body excitations when

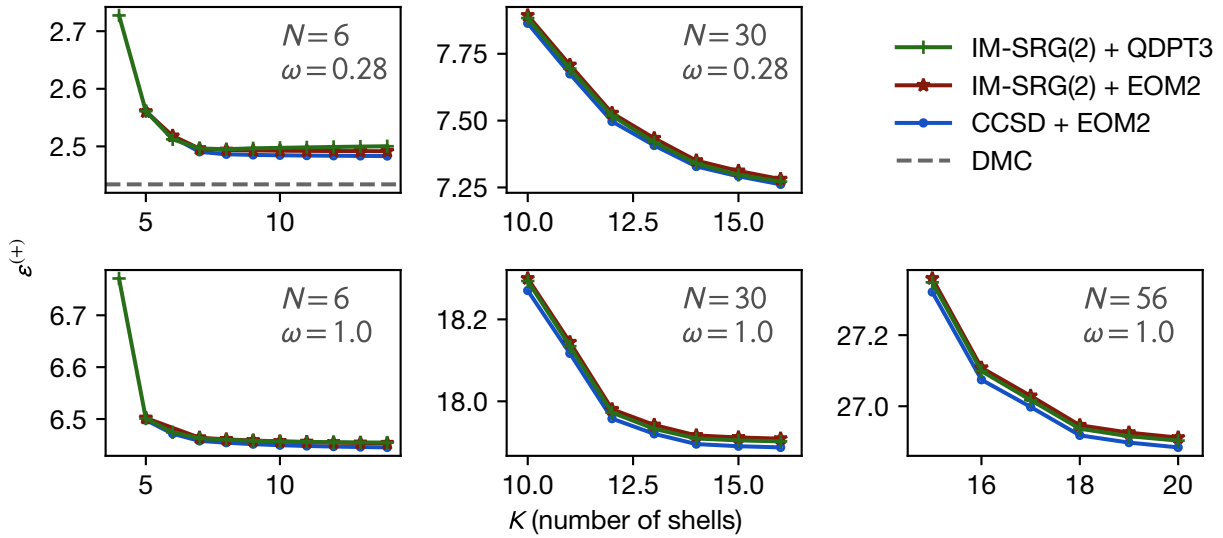


Figure 4.3: Particle-attached energy (in Hartrees) of quantum dots with N particles and an oscillator frequency of ω calculated with several different methods.

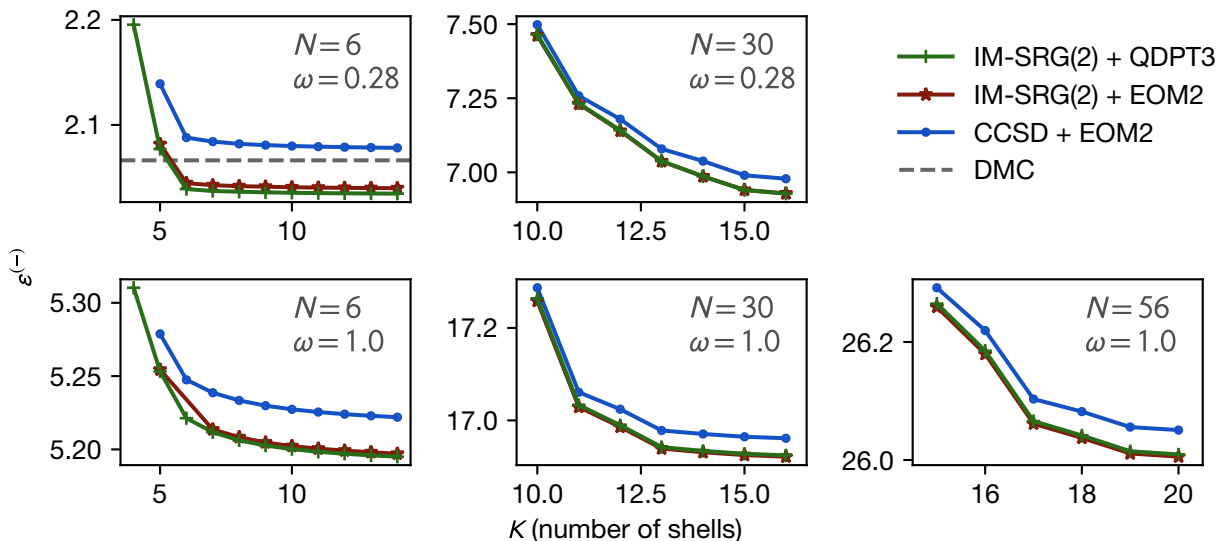


Figure 4.4: Particle-removed energy (in Hartrees) of quantum dots with N particles and an oscillator frequency of ω calculated with several different methods.

compared to the corresponding state calculated with the CI method and the bare Hamiltonian.

Despite this improvement on the corresponding CI method, the EOM(2) truncation of Eqs. (4.3) and (4.3) is not guaranteed to capture the primary components of certain collective states. Therefore, the quality of the solution can be judged by measuring the amount of overlap between the EOM solution and 1p-0h states for PA-EOM or 0p-1h states for PR-EOM. This overlap can be computed with partial norms,

$$n_{\text{1-particle}} = \sqrt{\sum_a \langle \Phi^a | \hat{R}_\mu | \Phi_0 \rangle \langle \Phi_0 | \hat{L}_\mu | \Phi^a \rangle} = \sqrt{\sum_a |r^a l_a|}, \quad (4.42)$$

$$n_{\text{1-hole}} = \sqrt{\sum_i \langle \Phi_i | \hat{R}_\mu | \Phi_0 \rangle \langle \Phi_0 | \hat{L}_\mu | \Phi_i \rangle} = \sqrt{\sum_i |r_i l^i|}. \quad (4.43)$$

If the single-particle overlap is small, the state is dominated by higher-order excitations and requires a less-restricted truncation in order to describe it properly, which can be accomplished directly or perturbatively [149, 52]. On the other hand, large single-particle partial norms indicate that the EOM truncation is reasonable for the relevant state.

Figure 4.5 shows this relationship using the difference between EOM-CC and full CI energies for quantum dot particle-attached and particle-removed states, $\Delta E/E$, as function of the single-particle overlap. The energy difference with the exact FCI result grows as the single-particle character of the wave function shrinks. Therefore, care should be taken when encountering unphysical states with a small single-particle overlap.

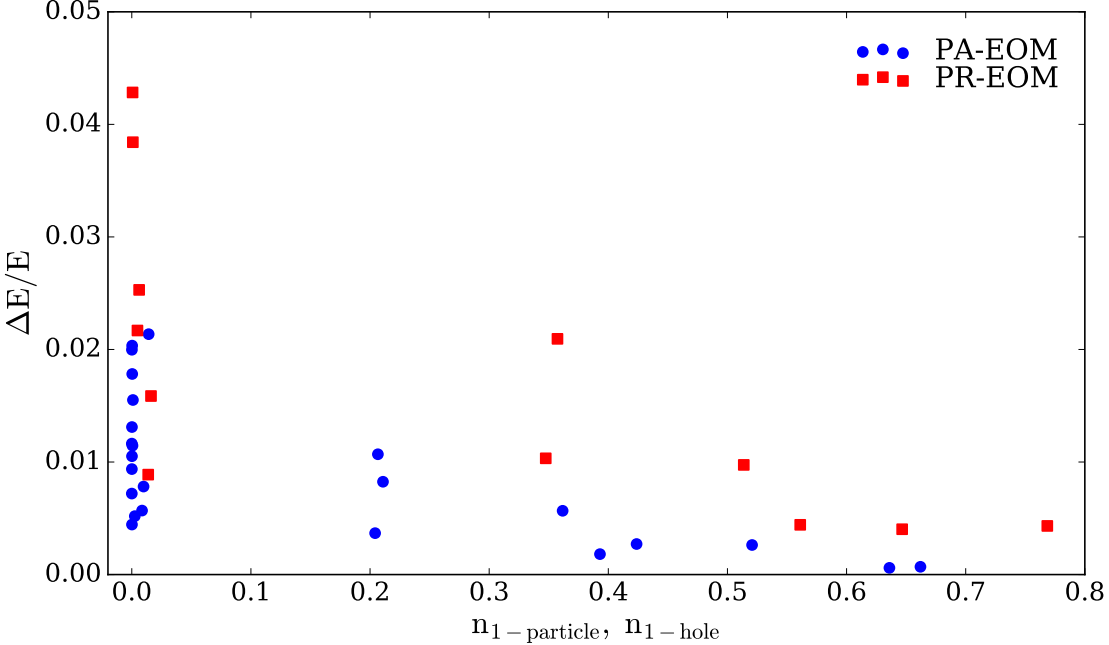


Figure 4.5: Energy difference of particle-attached and particle-removed states between the EOM-CC method and the exact FCI method for a quantum dot with various parameters plotted against the single-particle overlap of the FCI state, $n_{1\text{-particle}}$ or $n_{1\text{-hol}}$, see Eqs. (4.42) and (4.43). The strong correlation shows that the quality of EOM states can be judged by this metric.

4.6 EOM-CC for Finite Nuclei

Like its ground-state counterpart, the EOM extension to coupled cluster theory was first applied to nuclear systems [150, 151, 152]. However the progress was again halted by the non-perturbative nucleon-nucleon interaction, so again it quickly gained prominence in quantum chemistry [153, 18]. Since the introduction of SRG-softened chiral interactions, the EOM-CC method has been established as a powerful and reliable method for reaching open-shell systems and excited states [44, 50, 133, 154, 155]. This section shows results for the PA-EOM-CC and PR-EOM-CC methods calculated with the NN+3N(400) interaction, SRG softened with $\lambda_{\text{SRG}} = 2.0 \text{ fm}^{-1}$. The initial closed-shell calculations were performed for ^{16}O and ^{22}O .

The ground-state energies for particle-attached nuclei are shown in Fig. 4.6. Unlike

the ground states for closed-shell nuclei, which is uniquely determined, the particle-attached ground state must be identified as the state corresponding to the lowest eigenvalue of the converged solution. All the results are in close agreement with the experimental values while the subshell nuclei, ^{23}O and ^{23}F , are slightly underbound like their closed-shell counterpart, ^{16}O (see Fig. 3.10).

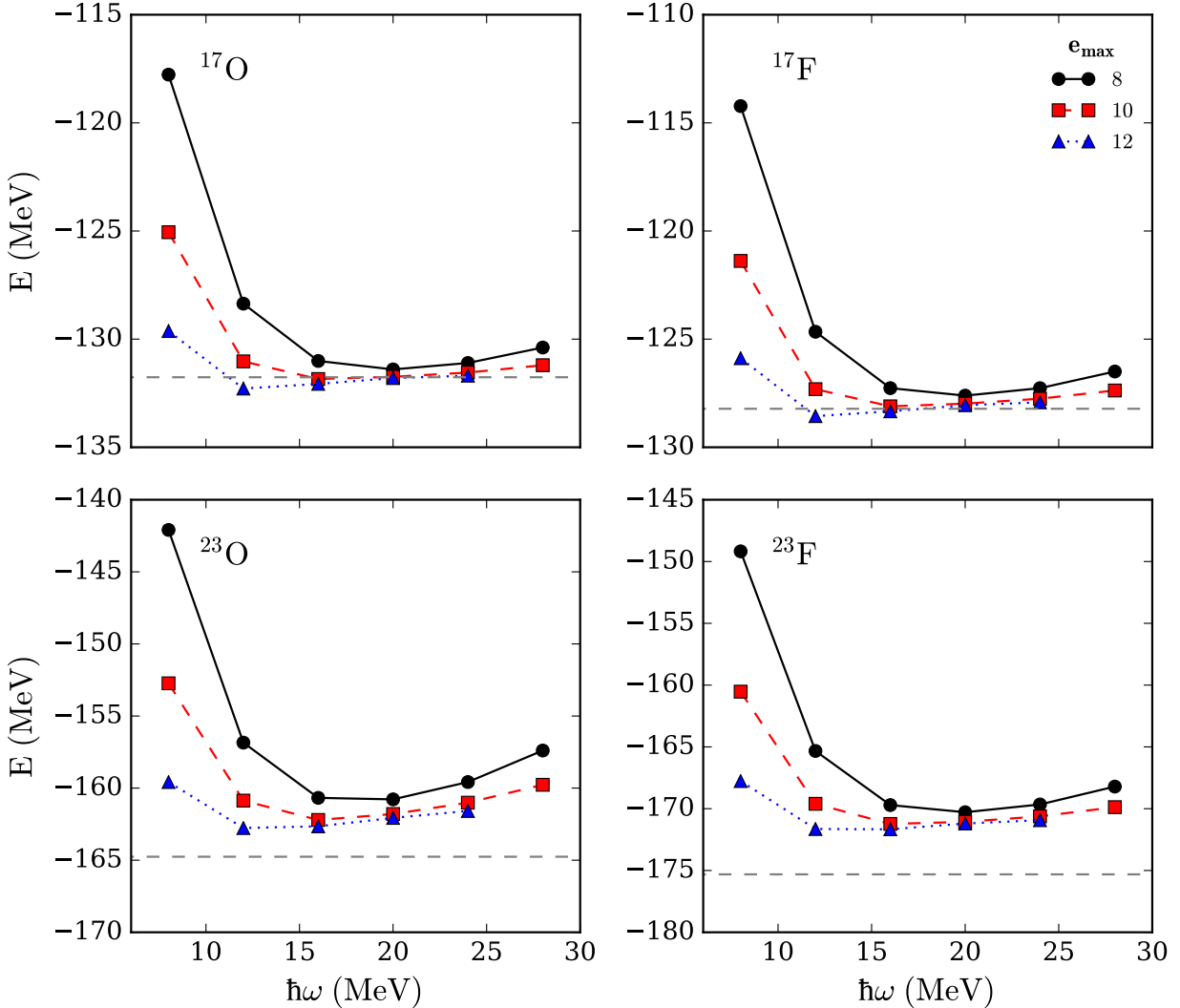


Figure 4.6: Ground-state energies for the particle-attached nuclei ^{17}O , ^{17}F , ^{23}O , and ^{23}F as a function of the harmonic oscillator energy $\hbar\omega$ with the NN+3N(400) interaction, SRG softened with $\lambda_{\text{SRG}} = 2\text{fm}^{-1}$. The energies are plotted for $e_{\max} = 8, 10, 12$, showing the convergence as the model space increases. The grey dashed line is the experimental binding energy.

The ground-state energies for particle-removed nuclei are shown in Fig. 4.7. These results follow the same pattern as the particle-attached states, converging to within $\sim 1\%$ at $e_{\max} = 12$ and overbinding for EOM states constructed from the ^{22}O ground state.

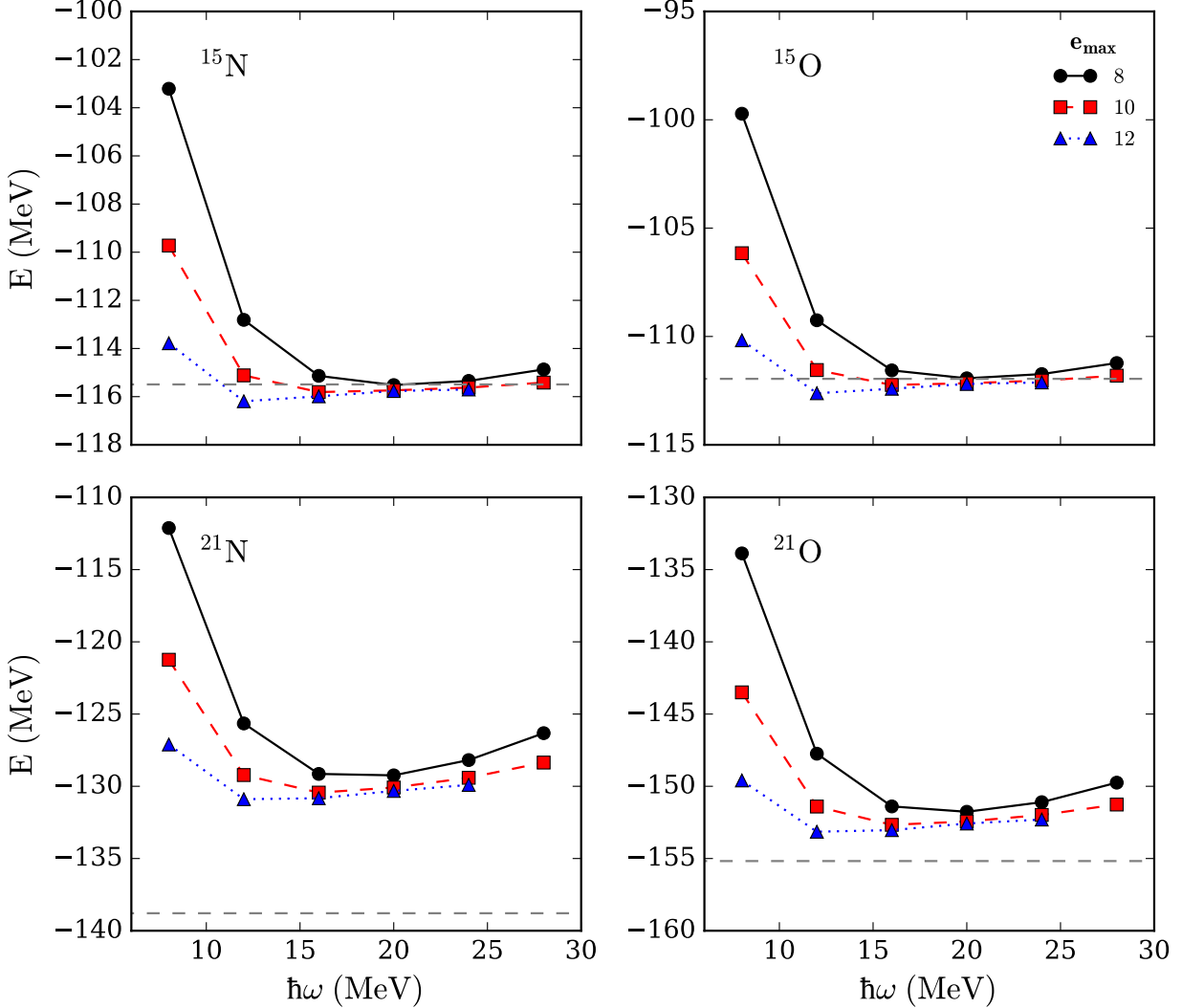


Figure 4.7: Ground-state energies for the particle-removed nuclei ^{15}N , ^{15}O , ^{21}N , and ^{21}O as a function of the harmonic oscillator energy $\hbar\omega$ with the NN+3N(400)-induced interaction, SRG softened with $\lambda_{\text{SRG}} = 2\text{fm}^{-1}$. The energies are plotted for $e_{\max} = 8, 10, 12$, showing the convergence as the model space increases. The grey dashed line is the experimental binding energy.

The problem of center-of-mass contamination discussed in section 3.7 extends to the EOM states as well. To ensure that the EOM wavefunction has been sufficiently factorized

from the COM wave function, an equivalent diagnostic to Fig. 3.11 can be performed. First, the ground-state COM energy is computed using Eq. (3.69) and the corresponding COM oscillator strength is obtained from Eq. (3.71). By using $A + 1$ particles for PA-EOM and $A - 1$ particles for PR-EOM in the intrinsic Hamiltonian, Eq. (3.66), the A -body problem is not properly treated. However, the approximate COM factorization for the $A + 1$ and $A - 1$ systems, according to Eq. (3.67), is reached when the COM energy vanishes at this new oscillator strength. The results from the COM diagnostic on the PA-EOM and PR-EOM states is shown in Fig. 4.8.

With the underlying COM oscillator strengths determined from Fig. 4.8, the excitation spectra of the corresponding open-shell nuclei can be treated with the Lawson-Gloeckner method [128] by artificially raising COM-coupled, spurious states out of the range of interest by adding the COM Hamiltonian to the intrinsic Hamiltonian, Eq. (3.72). The EOM low-lying excited states of ^{17}O and ^{17}F are shown in Fig. 4.9 with and without the Lawson-Gloeckner term. When the term is added, the spurious negative-parity states are removed from the lower portion of the spectra. The non-spurious states, $1/2^+$ and $3/2^+$, are not removed but do increase slightly due to the imperfect COM factorization.

While the experimental excited states of the particle-attached nuclei ^{23}O and ^{23}F are not well-known, the EOM states can be treated in an equivalent way to remove the negative-parity states in ^{23}O , shown in Fig. 4.10. The low-lying excited states of the particle-removed nuclei ^{15}N and ^{15}O are shown in Fig. 4.11 and those of ^{21}N and ^{21}O are shown in Fig. 4.12. These EOM-CC states can now be used to calculate properties of excited-states and open-shell systems. In particular, the transition amplitudes between neutron- and proton-attached states, or between neutron- and proton-removed states, describes the nuclear structure components of the corresponding beta-decay.

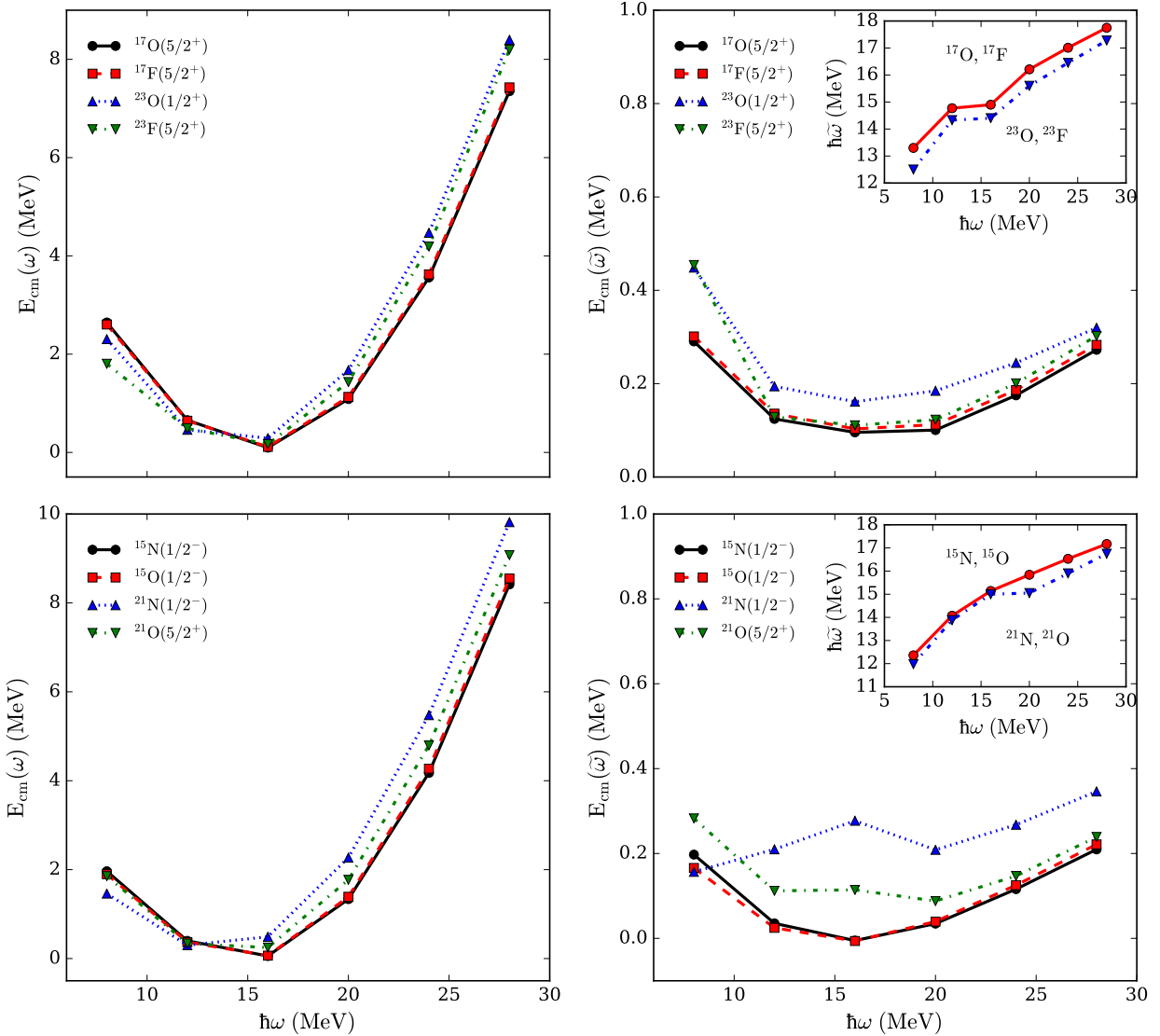


Figure 4.8: Ground-state COM energies, Eq. (3.68), for open-shell nuclei at varies harmonic oscillator frequencies with the NN+3N(400)-induced interaction with $\lambda_{SRG} = 2.0 \text{ fm}^{-1}$ at $e_{\max} = 12$. The top row shows the results for the particle-attached nuclei ^{17}O , ^{17}F , ^{23}O , and ^{23}F , and the bottom row shows the results for the particle-removed nuclei ^{15}N , ^{15}O , ^{21}N , and ^{21}O . The right column shows that the COM wave function practically vanishes according to Eq. (3.67).

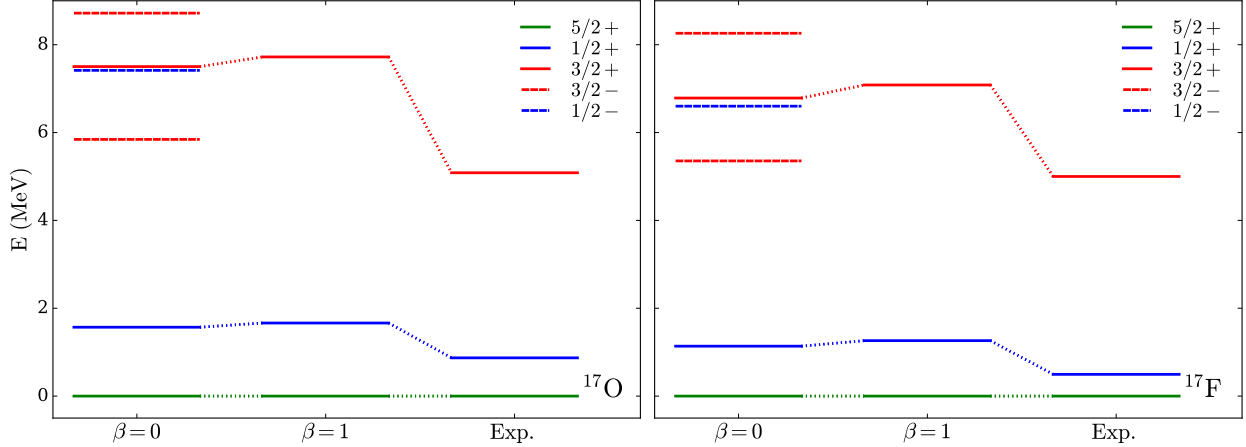


Figure 4.9: Low-lying PA-EOM states for ^{17}O and ^{17}F with and without a Lawson-Gloeckner term, along with the experimentally determined spectra. The negative-parity states are COM contaminants and are removed by artificially raising the COM excitation energy with the parameter β according to Eq. (3.72).

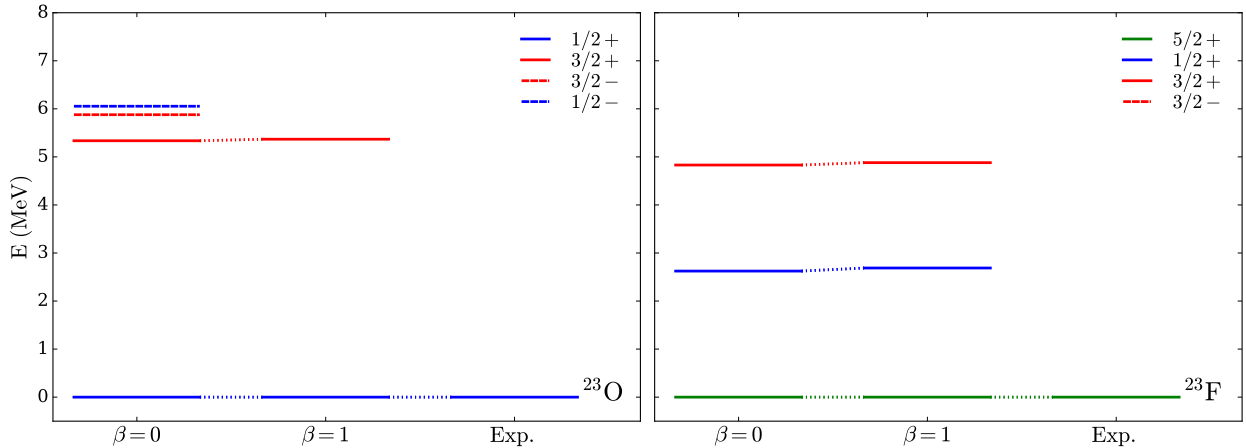


Figure 4.10: Low-lying PA-EOM states for ^{23}O and ^{23}F with and without a Lawson-Gloeckner term. The negative-parity states in ^{17}O are COM contaminants and are removed by artificially raising the COM excitation energy with the Lawson-Gloeckner method, Eq. (3.72). The excited states of these nuclei have not been experimentally determined.

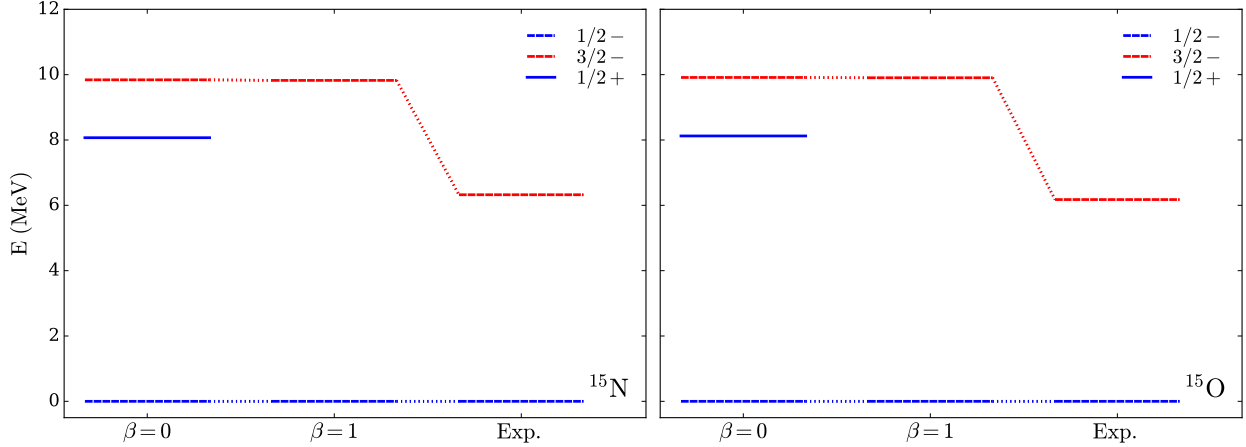


Figure 4.11: Low-lying PR-EOM states for ^{15}N and ^{15}O with and without a lawson-gloeckner term, and the experimentally determined spectra. The $1/2^+$ state is a COM contaminant and is removed by artificially raising the COM excitation energy with the parameter β according to Eq. (3.72).

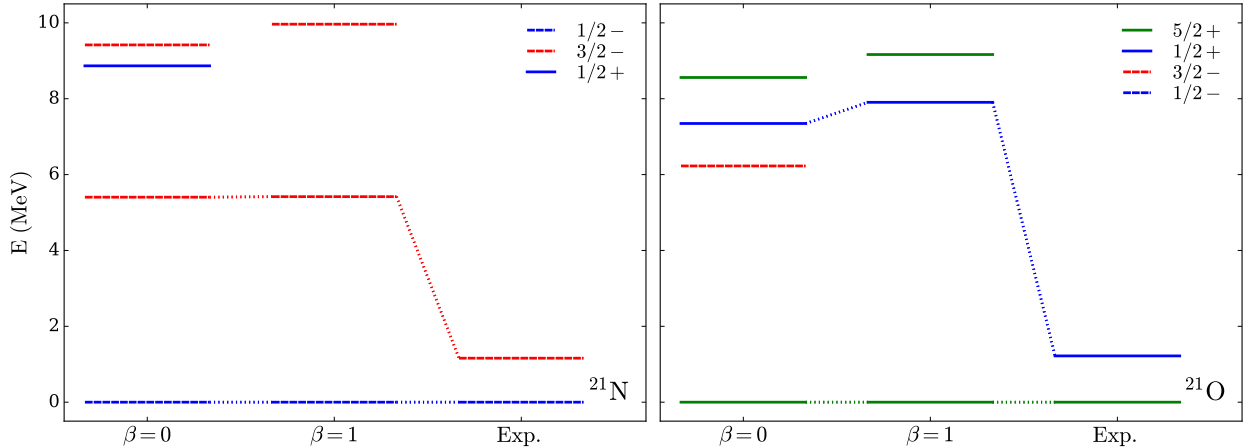


Figure 4.12: Low-lying PA-EOM states for ^{21}N and ^{21}O with and without a Lawson-Gloeckner term, Eq. (3.72), and the experimentally determined spectra. The negative-parity states in ^{17}O are COM contaminants and are removed by artificially raising the COM excitation energy. The excited states of these nuclei have not been experimentally determined.

Chapter 5

Beta-Decay Effective Operators

Now with the ability to calculate open-shell states, properties of and transitions between these states can be obtained. In particular, this chapter focuses on beta-decay transitions between two particle-attached states and between two particle-removed states. However, because these techniques are formulated in a general way, they can be applied to any type of one-body operator and any type of EOM-CC state. First, this chapter describes beta-decay processes in detail and the relevant operators are introduced. Then, these operators are used to construct effective coupled cluster operators that take important correlations from the ground-state wave function into account. Finally, the effective operators are applied to EOM-CC states to calculate transition amplitudes for the corresponding processes. These amplitudes can then be used to calculate observables like decay strengths and half-lives.

5.1 Beta-Decay Properties

Nuclear beta decay describes a class of radioactive decays of the atomic nucleus that result as a consequence of the weak interaction. These processes involve the exchange of a W boson which allows a quark within a proton or neutron to change type, thus converting a neutron to a proton or vice versa. Additionally, this conversion is accompanied by an electron-antineutrino or positron-neutrino pair which ensures the process conserves charge and lepton number. This work focuses on the three most common types of weak processes that occur within atomic nuclei: β^- decay, β^+ decay, and electron capture (EC). The first,

β^- decay, is the process whereby a down quark becomes an up quark, converting a neutron to a proton along with the creation of an electron, or β^- particle, and an antineutrino. Schematically, this decay can be written as,

$$\beta^- \text{ decay : } n \longrightarrow p + e^- + \bar{\nu}_e.$$

The corresponding mirror process is the β^+ decay, whereby an up quark becomes a down quark, converting a proton to a neutron with the creation of a positron, or β^+ particle, and a neutrino. This decay is represented by,

$$\beta^+ \text{ decay : } p \longrightarrow n + e^+ + \nu_e.$$

A closely related process is the electron capture, whereby an atomic electron interacts with an up quark of a proton via a W boson, causing the conversion to a down quark and the release of a neutrino. This process can be written as,

$$\text{Electron capture : } p + e^- \longrightarrow n + \nu_e.$$

These three processes are schematically represented in Fig. 5.1.

The decay Q -value is a measure of the net energy of these processes. In free space, only β^- decay has a positive Q -value and can occur spontaneously. However, within a nucleus, correlations between nucleons cause the relatively simple exchanges in Fig. 5.1 to take on more complicated, higher-order processes involving pion exchanges between different nucleons, see Fig. 5.2. This also has the effect of changing the energetics of the β^+ decay and electron-capture processes such that their Q -values are positive and can occur within certain

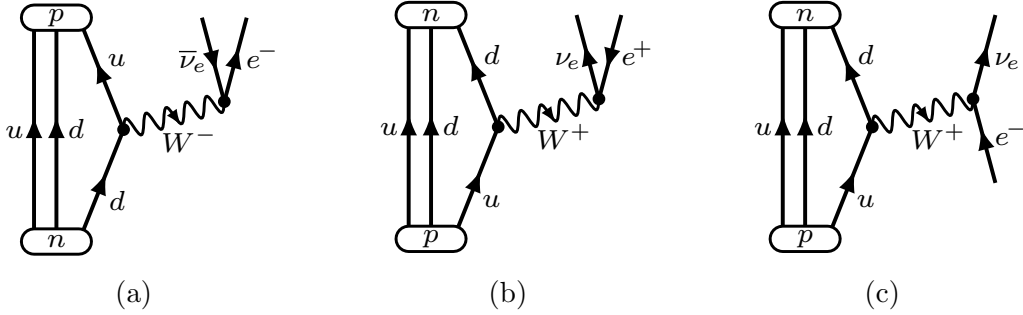


Figure 5.1: Schematic representations of the three free-space weak processes in this work: β^- decay (a), β^+ decay (b), and electron-capture (c). The coupling constant for the point interaction vertex is the weak-interaction coupling constant g_W .

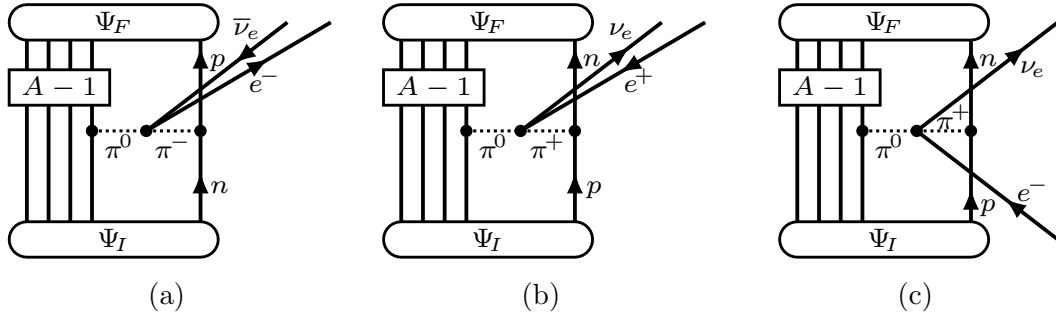


Figure 5.2: Schematic representations of a higher-order weak interactions involving pion-exchange that occur within a nucleus, for β^- decay (a), β^+ decay (b), and electron-capture (c). These processes are not included in the impulse approximation. The coupling constant for the point interaction vertex is the effective weak-interaction coupling constant G_F .

nuclei. However, these complicated processes can be approximated by assuming that the weak interaction occurs at very short length and time scales due to the large mass of the W boson, m_W . Known as the *impulse approximation*, this treatment of weak processes within nuclei ignores any nucleon-nucleon interactions involved in weak decays, instead treating a single nucleon as a spectator to the other nucleons during the weak interaction, shown in Fig. 5.3. In addition, this motivates the simplification of the W boson exchanges in Fig. 5.1, with coupling constant g_W , to a point interaction, shown in Figs. 5.3 and 5.2, with an effective coupling constant $G_F = \sqrt{2}g_W^2/8(m_W c^2)^2$ [156].

These beta-decay processes can be further characterized by the character of their angular momentum. *Allowed* beta decays involve an electron-antineutrino or positron-neutrino pair

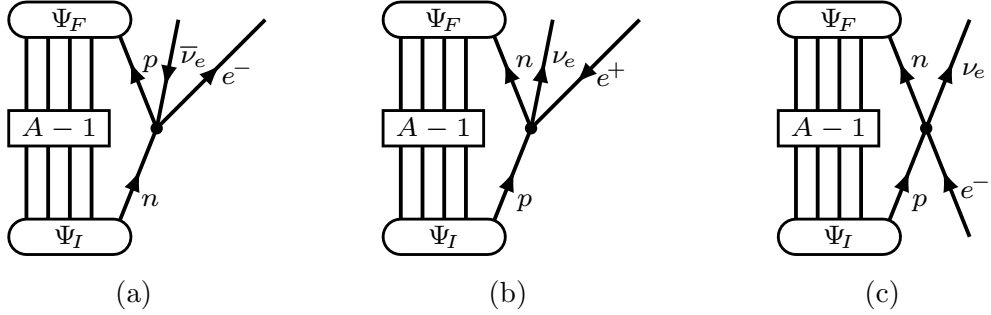


Figure 5.3: Schematic representations of the impulse approximations to the different weak processes within an A -body nucleus: β^- decay (a), β^+ decay (b), and electron-capture (c). The active nucleon doesn't interact with the initial and final nuclei during the weak process. The coupling constant for each interaction vertex is the weak-interaction coupling constant G_F .

with no angular momentum, $L = 0$. In this case, there can be no parity change between the initial and final nuclear states. Also, each pair of spin- $\frac{1}{2}$ leptons carries a coupled spin of either $S = 0$ or $S = 1$. Therefore, the initial and final nuclear states must have angular momenta that only differ by 0 or 1, ($\Delta J = 0, 1$). Additionally, parity must be conserved for these interactions. *Fermi transitions* (F) occur when the nuclear states are coupled to leptons with $S = 0$, and *Gamow-Teller transitions* (GT) occur when the lepton have a spin $S = 1$. The summary of these selection rules are shown in table 5.1. It should be

Decay Type	$\Delta J = J_F - J_I$	$\pi_F \pi_I$
Fermi	0	+1
Gamow-Teller	$1(J_F = 0 \text{ or } J_I = 0)$	+1
Gamow-Teller	$0, 1(J_F > 0 \text{ and } J_I > 0)$	+1

Table 5.1: Summary of the selection rules for allowed beta decays according to the angular momentum J and parity π of the initial (I) and final (F) states.

stated that while Gamow-Teller transitions can occur without a change in the nuclear spin ($\Delta J = 0$ for $J_F > 0$ and $J_I > 0$), the Gamow-Teller operator carries an angular momentum of $J = 1$.

The half-life of these processes $T_{1/2}$ can be calculated using a combination of both the

Fermi and Gamow-Teller type transitions in the form of their reduced transition amplitudes, B_F and B_{GT} , respectively,

$$B_F = \frac{g_V^2 |M_F|^2}{2J_i + 1} \quad B_{GT} = \frac{g_A^2 |M_{GT}|^2}{2J_i + 1}, \quad (5.1)$$

where J_i is the final state angular momentum. The factor g_V is the vector coupling constant, and its value can be shown to be exactly $g_V = 1.0$. The axial-vector coupling constant g_A has a free-space value of $g_A = -g_V$, but is altered within nuclei due to nucleon-nucleon correlations. The exact problem of how to treat the value of the axial-vector constant has been a widely studied topic for decades [157, 158, 159, 160], but this work will use the value $g_A/g_V = 1.261(8)$ [161]. The transition matrix elements M_F and M_{GT} are measures of the overlap integral between the initial and final nuclear states for the different transitions and will be discussed in the next section. Inserting these reduced transition amplitudes into the standard result from time-dependent perturbation theory gives the decay half-life,

$$T_{1/2} = \frac{f}{K_0 (B_F + B_{GT})}. \quad (5.2)$$

The factor f represents a phase-space integral over the final nuclear and lepton states and depends on the decay Q-value. The factor K_0 encodes the relevant constants involved,

$$K_0 = \frac{2\pi^3 \hbar^7 \ln 2}{m_e^5 c^4 G_F^2} \approx 6147 \text{ s}, \quad (5.3)$$

where m_e is the electron mass, and G_F is the effective coupling constant. The next section describes the process of improving upon the impulse approximation by using coupled cluster theory to include higher-body interactions with the CC similarity transformation.

5.2 Coupled Cluster Effective Operators

The main step in calculating dynamic properties within an *ab initio* framework is to calculate the transition matrix elements of the relevant operator between two correlated many-body states. In the cases considered in this thesis, the correlated many-body states are given by right and left expansions for the PA-EOM(2) and PR-EOM(2) operators in Eqs. (4.3) and (4.3), respectively. Beta-decay properties are computed with the Fermi and Gamow-Teller operators which are one-body operators that change a neutron to a proton or vice versa and carry the quantum numbers that correspond to the rules in table 5.1.

In the impulse approximation, the Fermi operator, which has no spin component, is simply equivalent to the isospin raising operator for the β^- Fermi transition, which changes a neutron to a proton, or the lowering operator for the β^+ transition, which changes a proton to a neutron,

$$\hat{O}_{F^\mp} = \sum_{pq} \langle p \| \hat{\tau}_\pm \| q \rangle \left\{ \hat{a}_p^\dagger \hat{a}_q \right\}. \quad (5.4)$$

The reduced matrix element, see appendix D, $\langle p \| \hat{\tau}_\pm \| q \rangle$, is given by, see [162],

$$\langle p \| \hat{\tau}_\pm \| q \rangle = \sqrt{2j_p + 1} \delta_{npnq} \delta_{lplq} \delta_{jpjq} \delta_{tp tq \pm 1}, \quad (5.5)$$

where the quantum numbers n and l can refer to the quantum numbers of any spherical basis, such as the harmonic oscillator basis, and t is the states isosping projection. Similarly, the Gamow-Teller operator also includes the isospin raising/lowering operator in addition to the spin operator $\hat{\sigma}$,

$$\hat{O}_{GT^\mp} = \sum_{pq} \langle p \| \hat{\sigma} \hat{\tau}_\pm \| q \rangle \left\{ \hat{a}_p^\dagger \hat{a}_q \right\}. \quad (5.6)$$

Here, the reduced matrix element, $\langle p \| \hat{\sigma} \hat{\tau}_\pm \| q \rangle$, is also given by, see [162],

$$\langle p \| \hat{\sigma} \hat{\tau}_\pm \| q \rangle = \sqrt{6(2j_p + 1)(2j_q + 1)} \left\{ \begin{array}{ccc} \frac{1}{2} & \frac{1}{2} & 1 \\ j_q & j_p & l_p \end{array} \right\} (-1)^{l_p + j_p + \frac{3}{2}} \delta_{npnq} \delta_{lpjq} \delta_{tp tq \pm 1}. \quad (5.7)$$

These operators can now be used to calculate the transition matrix elements in Eq. (5.1) by applying them between an initial state, $|\Psi_i\rangle$, and a final state, $\langle\Psi_f|$. The Fermi reduced transition amplitude is,

$$M_F = \langle \Psi_f \| \hat{O}_{F^\mp} \| \Psi_i \rangle = \delta_{J_f J_i} \sum_{pq} \langle p \| \hat{\tau}_\pm \| q \rangle \langle \Psi_f \| \left\{ \hat{a}_p^\dagger \hat{a}_q \right\} \| \Psi_i \rangle. \quad (5.8)$$

Similarly, the Gamow-Teller reduced transition amplitude is,

$$M_{GT} = \langle \Psi_f \| \hat{O}_{GT^\mp} \| \Psi_i \rangle = \sum_{pq} \langle p \| \hat{\sigma} \hat{\tau}_\pm \| q \rangle \langle \Psi_f \| \left\{ \hat{a}_p^\dagger \hat{a}_q \right\} \| \Psi_i \rangle. \quad (5.9)$$

Within the coupled cluster framework, the initial and final states take the form of PA-EOM or PR-EOM states given generically in Eq. (4.1). According to Eqs. (4.7) and (4.12), the left and right eigenstates of the bare Hamiltonian can be given by $\langle \Psi_f | = \langle \Phi_0 | \hat{L}_f e^{-\hat{T}}$ and $|\Psi_i\rangle = e^{\hat{T}} \hat{R}_i |\Phi_0\rangle$. Inserting these EOM states into Eqs. (5.8) and (5.9), gives,

$$M_F = \delta_{J_f J_i} \sum_{pq} \langle p \| \hat{\tau}_\pm \| q \rangle \langle \Phi_0 \| \hat{L}_f e^{-\hat{T}} \left\{ \hat{a}_p^\dagger \hat{a}_q \right\} e^{\hat{T}} \hat{R}_i \| \Phi_0 \rangle. \quad (5.10)$$

Similarly, the Gamow-Teller matrix element becomes,

$$M_{GT} = \sum_{pq} \langle p \| \hat{\sigma} \hat{\tau}_\pm \| q \rangle \langle \Phi_0 \| \hat{L}_f e^{-\hat{T}} \left\{ \hat{a}_p^\dagger \hat{a}_q \right\} e^{\hat{T}} \hat{R}_i \| \Phi_0 \rangle. \quad (5.11)$$

The resemblance of these equations to Eq. (3.6) motivates the construction of an effective

operator, ${}^\lambda\bar{O}$. The Fermi and Gamow-Teller effective operators have the form,

$$\bar{O}_{F\mp} = \sum_{pq} \langle p \| \hat{\tau}_\pm \| q \rangle e^{-\hat{T}} \left\{ \hat{a}_p^\dagger \hat{a}_q \right\} e^{\hat{T}}, \quad (5.12)$$

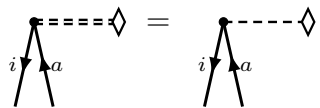
$$\bar{O}_{GT\mp} = \sum_{pq} \langle p \| \hat{\sigma} \hat{\tau}_\pm \| q \rangle e^{-\hat{T}} \left\{ \hat{a}_p^\dagger \hat{a}_q \right\} e^{\hat{T}}. \quad (5.13)$$

The similarity-transformed component, $e^{-\hat{T}} \left\{ \hat{a}_p^\dagger \hat{a}_q \right\} e^{\hat{T}}$, is known as the *one-body density matrix*. Using the Baker-Campbell-Housedorf expansion like Eq. (3.7) and the reduction to connected diagrams like Eq. (3.8), the one-body density matrix can be reduced to the form,

$$e^{-\hat{T}} \left\{ \hat{a}_p^\dagger \hat{a}_q \right\} e^{\hat{T}} = \left(\left\{ \hat{a}_p^\dagger \hat{a}_q \right\} e^{\hat{T}} \right)_c. \quad (5.14)$$

The effective operators are best calculated using diagrammatic techniques like those used for the effective Hamiltonian. In this case, the bare one-body operators are depicted by the vertex type  while the effective one- and two-body operators are depicted by  and , respectively.

The one-body beta-decay operators can be split into hp, hh, pp, and ph components which are analogous to the one-body components of the effective Hamiltonian, see appendix B. The hp component has no connected terms in Eq. (5.14), and so it is unchanged by the similarity transformation,



$${}^\lambda\bar{O}_a^i = {}^\lambda O_a^i. \quad (5.15)$$

The pp component is augmented by single excitations from the reference state. This component's diagrammatic and algebraic expressions are,

$$\lambda \bar{O}_b^a = \lambda O_b^a - \sum_k \lambda \bar{O}_b^k t_k^a. \quad (5.16)$$

Similarly, the hh component is also augmented by single excitations from the reference state,

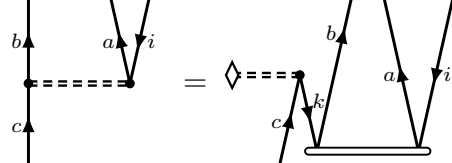
$$\lambda \bar{O}_j^i = \lambda O_j^i + \sum_c \lambda \bar{O}_c^i t_j^c. \quad (5.17)$$

The ph component of the effective beta-decay operator includes effects from single and double excitations from the reference state. The diagrammatic and algebraic expressions for this component are,

$$\lambda \bar{O}_i^a = \lambda O_i^a + \sum_c \lambda \bar{O}_c^a t_i^c - \sum_k \lambda \bar{O}_i^k t_k^a + \sum_{kc} \lambda \bar{O}_c^k t_{ik}^{ac}. \quad (5.18)$$

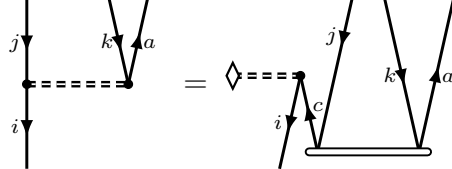
Like the higher-body interactions induced by the CC similarity transformation, two-body effective operators are induced from the one-body bare beta-decay operator. Calculating properties using PA-EOM(2) and PR-EOM(2) states requires only two components of the

effective two-body operator. The pphp component is the results of double excitations from the reference state and is given by the following diagram and the corresponding expression,



$$\lambda \bar{O}_{ic}^{ab} = - \sum_k \lambda \bar{O}_c^k t_{ik}^{ab}. \quad (5.19)$$

Similarly, the hphh component is represented by the following diagram and its corresponding algebraic expression,



$$\lambda \bar{O}_{jk}^{ia} = \sum_c \lambda \bar{O}_c^i t_{jk}^{ca}. \quad (5.20)$$

After constructing the effective operators, the reduced transition amplitudes in Eq. (5.1) can be calculated. Because of the ambiguity in the bi-orthonormalization discussed in section 4.2, the square-norm of the matrix elements, $|M|^2$, must be written using both the left and right solutions for each of the initial and final states. Expanded in terms of the EOM states, these reduced amplitudes for the Fermi and Gamow-Teller operators become,

$$B_F = \frac{g_V^2}{2J_i + 1} \delta_{J_f J_i} \sum_f \langle \Phi_0 | \hat{L}_i \bar{O}_{F^\pm} \hat{R}_f | \Phi_0 \rangle \langle \Phi_0 | \hat{L}_f \bar{O}_{F^\mp} \hat{R}_i | \Phi_0 \rangle, \quad (5.21)$$

$$B_{GT} = \frac{g_A^2}{2J_i + 1} \sum_f \langle \Phi_0 | \hat{L}_i \bar{O}_{GT^\pm} \hat{R}_f | \Phi_0 \rangle \langle \Phi_0 | \hat{L}_f \bar{O}_{GT^\mp} \hat{R}_i | \Phi_0 \rangle. \quad (5.22)$$

Using the machinery developed in this thesis and the techniques discussed in this chapter,

the calculated half-lives of various nuclei will be presented in an upcoming paper.

Chapter 6

Conclusions and Perspectives

6.1 Summary and Conclusions

Accurate *ab initio* calculations of beta-decay transition amplitudes are necessary for answering many open questions from a wide range of areas in modern physics from nucleosynthesis to fundamental symmetries. The accuracy and scope needed to answer such questions necessitate a technique that is widely applicable, systematically improvable, and scalable to large systems. In this thesis, we have developed the formalism for and achieved the application of techniques based on coupled cluster theory that fulfill these requirements.

The large and versatile program that implements these techniques can be used for many different fermionic systems including the homogeneous electron gas, quantum dots, and finite nuclei. Because of the program's modular form, additional systems like neutron drops, infinite nuclear matter, and atomic systems can easily be added in subsequent updates. Importantly, we extended the single-determinant coupled-cluster method to open-shell systems using the equation-of-motion method which grants a broader reach across the nuclear chart. Also, we added the crucial ability to perform calculations with and without three-body forces which ensures accurate results. Also modular, these components of the program can be easily extended to higher-order EOM approximations, two-particle-attached and two-particle-removed EOM states, and the inclusion of full three-body forces. Lastly, we've implemented the ability to construct any effective one-body operator and calculate the corresponding

observables using ground and excited EOM states. In future iterations of this code, higher-order effective operators, like those required for double-beta-decay experiments, can also be implemented. Also, these higher-order operators can be constructed from two-body chiral weak currents and used to investigate the quenching of the axial vector coupling constant.

In addition to developing and implementing these various techniques, we performed calculations at each step to verify the results. In particular, we provided a proof of principle by comparing our results with those from other *ab initio* methods for various different systems. Also, we calculated ground-state energies as well as particle-attached and particle-removed spectra for various light nuclei, focusing mainly on the oxygen chain. In future publications, this machinery will be extended up the nuclear chart to heavier nuclei and out to the limits of stability to calculate beta-decay properties of nuclei around ^{78}Ni and ^{100}Sn , which are important to future experiments at FRIB. For example, consistent beta-decay lifetime calculations from *ab initio* methods will be invaluable for astrophysical simulations of different nucleosynthesis processes.

APPENDICES

Appendix A

CCSD Diagrams

The following diagrams and their corresponding algebraic expressions comprise the different contributions to the CCSD cluster amplitudes *without* directly building the effective Hamiltonian, \bar{H} . The boxed diagrams are automatically zero in a Hartree-Fock basis. The contributions to the CCSD singles equation, (3.10), are given by Eqs. (A.1)-(A.8).

$$\begin{aligned} \hat{f}_N \hat{t}_1 |\Phi_0\rangle_c &= \boxed{\text{Diagram}} + \text{Diagram} + \text{Diagram} \\ &= [f_i^a] - \sum_k f_i^k t_k^a + \sum_c f_c^a t_i^c \end{aligned} \quad (\text{A.1})$$

$$\begin{aligned} \hat{V}_N \hat{t}_1 |\Phi_0\rangle_c &= \text{Diagram} \\ &= - \sum_{kc} V_{ic}^{ka} t_k^c \end{aligned} \quad (\text{A.2})$$

$$\begin{aligned}
\hat{f}_N \hat{t}_2 |\Phi_0\rangle_c &= \text{Diagram} \\
&= \sum_{[kc]} f_c^k t_{ki}^{ac} \quad (\text{A.3})
\end{aligned}$$

$$\begin{aligned}
\hat{V}_N \hat{t}_2 |\Phi_0\rangle_c &= \text{Diagram} + \text{Diagram} \\
&= \frac{1}{2} \sum_{kcd} V_{cd}^{ka} t_{ki}^{cd} + \frac{1}{2} \sum_{klc} V_{ic}^{kl} t_{kl}^{ca} \quad (\text{A.4})
\end{aligned}$$

$$\begin{aligned}
\hat{f}_N \hat{t}_1^2 |\Phi_0\rangle_c &= \text{Diagram} \\
&= \sum_{[kcd]} \hat{f}_d^l t_l^a t_i^d \quad (\text{A.5})
\end{aligned}$$

$$\begin{aligned}
\hat{V}_N \hat{t}_1^2 |\Phi_0\rangle_c &= \text{Diagram} + \text{Diagram} \\
&= \sum_{kcd} V_{cd}^{ka} t_k^c t_i^d + \sum_{klc} V_{ic}^{kl} t_k^c t_l^a \quad (\text{A.6})
\end{aligned}$$

$$\begin{aligned}
\hat{V}_N \hat{t}_1 \hat{t}_2 |\Phi_0\rangle_c &= \text{Diagram 1} + \text{Diagram 2} + \text{Diagram 3} \\
&= -\frac{1}{2} \sum_{klcd} V_{cd}^{kl} t_{ki}^{cd} t_l^a - \frac{1}{2} \sum_{klcd} V_{cd}^{kl} t_{kl}^{ca} t_i^d + \sum_{klcd} V_{cd}^{kl} t_{il}^{ad} t_k^c
\end{aligned} \tag{A.7}$$

$$\begin{aligned}
\hat{V}_N \hat{t}_1^3 |\Phi_0\rangle_c &= \text{Diagram 1} \\
&= - \sum_{klcd} V_{cd}^{kl} t_k^c t_i^d t_l^a
\end{aligned} \tag{A.8}$$

The contributions to the CCSD doubles equation, (3.10), are given by Eqs. (A.9)-(A.19).

$$\begin{aligned}
\hat{V}_N |\Phi_0\rangle_c &= \text{Diagram 1} \\
&= V_{ij}^{ab}
\end{aligned} \tag{A.9}$$

$$\begin{aligned}
\hat{f}_N \hat{t}_2 |\Phi_0\rangle_c &= \text{Diagram 1} + \text{Diagram 2} \\
&= \hat{P}(ab) \sum_c f_c^b t_{ij}^{ac} - \hat{P}(ij) \sum_k f_j^k t_{ik}^{ab}
\end{aligned} \tag{A.10}$$

$$\hat{V}_N \hat{t}_1 |\Phi_0\rangle_c = \begin{array}{c} \text{Diagram showing two terms:} \\ \text{Term 1: } \text{Two vertical lines } a \text{ and } b \text{ meet at a point } i. \text{ From } i, \text{ a dashed line } k \text{ goes down to a base.} \\ \text{Term 2: } \text{Two vertical lines } i \text{ and } j \text{ meet at a point } a. \text{ From } a, \text{ a dashed line } c \text{ goes down to a base.} \end{array} + \hat{P}(ab) \sum_k V_{ij}^{kb} t_k^a + \hat{P}(ij) \sum_c V_{cj}^{ab} t_i^c \quad (\text{A.11})$$

$$\hat{V}_N \hat{t}_2 |\Phi_0\rangle_c = \begin{array}{c} \text{Diagram showing three terms:} \\ \text{Term 1: } \text{Two vertical lines } a \text{ and } b \text{ meet at a point } i. \text{ From } i, \text{ a dashed line } l \text{ goes down to a point } j. \\ \text{Term 2: } \text{Two vertical lines } i \text{ and } j \text{ meet at a point } a. \text{ From } a, \text{ a dashed line } c \text{ goes down to a point } d. \\ \text{Term 3: } \text{Two vertical lines } a \text{ and } b \text{ meet at a point } i. \text{ From } i, \text{ a dashed line } k \text{ goes down to a point } c. \end{array} + \frac{1}{2} \sum_{kl} V_{ij}^{kl} t_{kl}^{ab} + \frac{1}{2} \sum_{cd} V_{cd}^{ab} t_{ij}^{cd} - \hat{P}(ij|ab) \sum_{kc} V_{ic}^{kb} t_{kj}^{ac} \quad (\text{A.12})$$

$$\hat{V}_N \hat{t}_1^2 |\Phi_0\rangle_c = \begin{array}{c} \text{Diagram showing three terms:} \\ \text{Term 1: } \text{Two vertical lines } a \text{ and } b \text{ meet at a point } i. \text{ From } i, \text{ a dashed line } l \text{ goes down to a point } j. \\ \text{Term 2: } \text{Two vertical lines } i \text{ and } j \text{ meet at a point } a. \text{ From } a, \text{ a dashed line } c \text{ goes down to a point } d. \\ \text{Term 3: } \text{Two vertical lines } a \text{ and } b \text{ meet at a point } i. \text{ From } i, \text{ a dashed line } k \text{ goes down to a point } c. \end{array} + \sum_{kl} V_{ij}^{kl} t_k^a t_l^b + \sum_{cd} V_{cd}^{ab} t_i^c t_j^d - \hat{P}(ij|ab) \sum_{kc} V_{ic}^{kb} t_k^a t_j^c \quad (\text{A.13})$$

$$\begin{aligned}
\hat{V}_N \hat{t}_2^2 |\Phi_0\rangle_c &= \text{Diagram 1} + \text{Diagram 2} + \text{Diagram 3} \\
&\quad + \text{Diagram 4} \\
&= \frac{1}{4} \sum_{klcd} V_{cd}^{kl} t_{kl}^{ab} t_{ij}^{cd} + \hat{P}(ab) \sum_{klcd} V_{cd}^{kl} t_{lj}^{ac} t_{ki}^{bd} - \hat{P}(ij) \frac{1}{2} \sum_{klcd} V_{cd}^{kl} t_{lj}^{ab} t_{ki}^{cd} \\
&\quad - \hat{P}(ab) \frac{1}{2} \sum_{klcd} V_{cd}^{kl} t_{ij}^{db} t_{kl}^{ca} \tag{A.14}
\end{aligned}$$

$$\begin{aligned}
\hat{f}_N \hat{t}_1 \hat{t}_2 |\Phi_0\rangle_c &= \boxed{\text{Diagram 5}} + \boxed{\text{Diagram 6}} \\
&= -[\hat{P}(ab) \sum_{kc} \bar{f}_c^k \bar{t}_k^a \bar{t}_{ij}^{cb}] - [\hat{P}(ij) \sum_{kc} \bar{f}_c^k \bar{t}_i^c \bar{t}_{kj}^{ab}] \tag{A.15}
\end{aligned}$$

$$\begin{aligned}
\hat{V}_N \hat{t}_1 \hat{t}_2 |\Phi_0\rangle_c &= \text{Diagram 1} + \text{Diagram 2} + \text{Diagram 3} \\
&\quad + \text{Diagram 4} + \text{Diagram 5} + \text{Diagram 6} \\
&= \hat{P}(ij|ab) \sum_{kcd} V_{cd}^{ka} t_{jk}^{bc} t_i^d - \hat{P}(ij|ab) \sum_{klc} V_{ci}^{kl} t_{jk}^{bc} t_l^a - \hat{P}(ab) \frac{1}{2} \sum_{kcd} V_{cd}^{kb} t_{ij}^{cd} t_k^a \\
&\quad + \hat{P}(ij) \frac{1}{2} \sum_{klc} V_{cj}^{kl} t_{kl}^{ab} t_i^c + \hat{P}(ab) \sum_{kcd} V_{cd}^{ka} t_k^c t_{ij}^{db} - \hat{P}(ij) \sum_{klc} V_{ci}^{kl} t_k^c t_{lj}^{ab} \quad (\text{A.16})
\end{aligned}$$

$$\begin{aligned}
\hat{V}_N \hat{t}_1^3 |\Phi_0\rangle_c &= \text{Diagram 7} + \text{Diagram 8} \\
&= -\hat{P}(ij|ab) \sum_{kcd} V_{cd}^{kb} t_k^a t_i^c t_j^d + \hat{P}(ij|ab) \sum_{klc} V_{cj}^{kl} t_i^c t_k^a t_l^b \quad (\text{A.17})
\end{aligned}$$

$$\begin{aligned}
\hat{V}_N \hat{t}_1^2 \hat{t}_2 |\Phi_0\rangle_c &= \text{Diagram 1} + \text{Diagram 2} + \text{Diagram 3} \\
&\quad + \text{Diagram 4} + \text{Diagram 5} \\
&= \frac{1}{2} \sum_{klcd} V_{cd}^{kl} t_{kl}^{ab} t_i^c t_j^d + \frac{1}{2} \sum_{klcd} V_{cd}^{kl} t_{ij}^{cd} t_k^a t_l^b + \hat{P}(ij|ab) \sum_{klcd} V_{cd}^{kl} t_{lj}^{ac} t_k^b t_i^d \\
&\quad - \hat{P}(ij) \frac{1}{2} \sum_{klcd} V_{cd}^{kl} t_{lj}^{ab} t_k^c t_i^d - \hat{P}(ab) \frac{1}{2} \sum_{klcd} V_{cd}^{kl} t_{ij}^{db} t_k^c t_l^a
\end{aligned} \tag{A.18}$$

$$\begin{aligned}
\hat{V}_N \hat{t}_1^4 |\Phi_0\rangle_c &= \text{Diagram 6} \\
&= \sum_{klcd} V_{cd}^{kl} t_k^a t_l^b t_i^c t_j^d
\end{aligned} \tag{A.19}$$

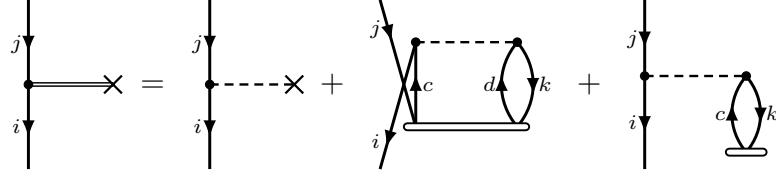
Appendix B

Effective Hamiltonian Diagrams

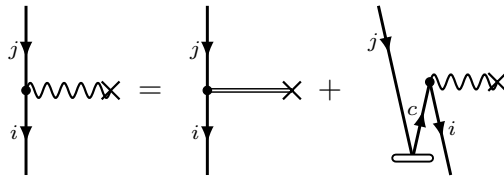
The following diagrams and their corresponding algebraic expressions comprise the different components of the CCSD effective Hamiltonian, \bar{H} . Because some components are used as intermediates to build other components, they must be built in the order written. Some intermediate components overcount some diagrams which motivates the need for further intermediates, denoted by X' , X'' , and X''' . The boxed diagrams are automatically zero in a Hartree-Fock basis. The one-body components to the CCSD effective Hamiltonian, Eq. (3.8), are given by Eqs. (B.1)-(B.4).

$$X_a^i = \boxed{f_a^i} + \sum_{kc} V_{ac}^{ik} t_k^c \quad (\text{B.1})$$

$$X_b^a = f_b^a - \frac{1}{2} \sum_{klc} V_{bc}^{kl} t_{kl}^{ac} + \sum_{kc} V_{cb}^{ka} t_k^c - \sum_k X_b^k t_k^a \quad (\text{B.2})$$

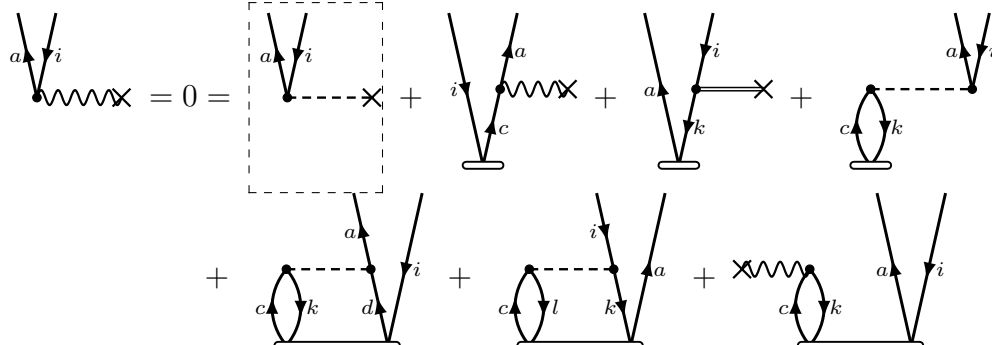


$$X_j'^i = f_j^i + \frac{1}{2} \sum_{kcd} V_{cd}^{ik} t_{jk}^{cd} + \sum_{kc} V_{jc}^{ik} t_k^c \quad (\text{B.3})$$



$$X_j^i = X_j'^i + \sum_c X_c^i t_j^c \quad (\text{B.4})$$

Once the one-body components have been constructed, the pseudo-linear form for the CCSD singles equation, Eq. (3.9), can be evaluated,



$$\begin{aligned} X_i^a = 0 &= [f_i^a] + \sum_c X_c^a t_i^c - \sum_k X_k'^i t_k^a + \sum_{kc} V_{ci}^{ka} t_k^c \\ &\quad + \frac{1}{2} \sum_{kcd} V_{cd}^{ka} t_{ki}^{cd} - \frac{1}{2} \sum_{klc} V_{ic}^{kl} t_{kl}^{ac} + \sum_{kc} X_c^k t_{ik}^{ac}. \end{aligned} \quad (\text{B.5})$$

During a CC iteration, it's possible to use these updated singles amplitudes \hat{T}_1 when evaluating the doubles amplitudes \hat{T}_2 in the same iteration, which can accelerate the convergence.

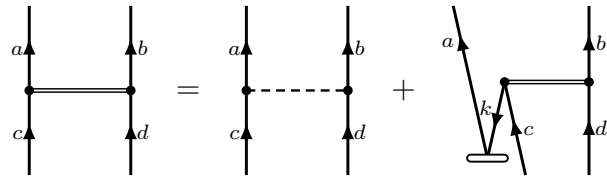
The two-body components to the CCSD effective Hamiltonian, Eq. (3.8), are given by Eqs. (B.6)-(B.20).

$$X'_{bc}^{ia} = V_{bc}^{ia} - \frac{1}{2} \sum_k V_{bc}^{ik} t_k^a \quad (B.6)$$

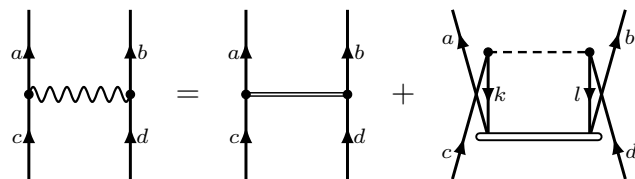
$$X_{bc}^{ia} = V_{bc}^{ia} - \sum_k V_{bc}^{ik} t_k^a \quad (B.7)$$

$$X'_{ka}^{ij} = V_{ka}^{ij} + \frac{1}{2} \sum_c V_{cat}^{ij} t_k^c \quad (B.8)$$

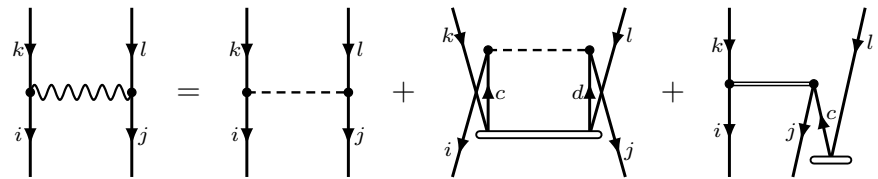
$$X_{ka}^{ij} = V_{ka}^{ij} + \sum_c V_{cat}^{ij} t_k^c \quad (B.9)$$



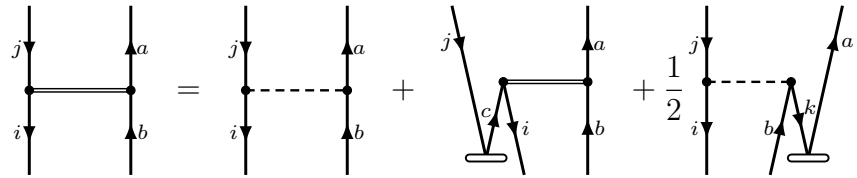
$$X'_{cd}^{ab} = V_{cd}^{ab} - \hat{P}(ab) \sum_k X'_{cd}^{kb} t_k^a \quad (\text{B.10})$$



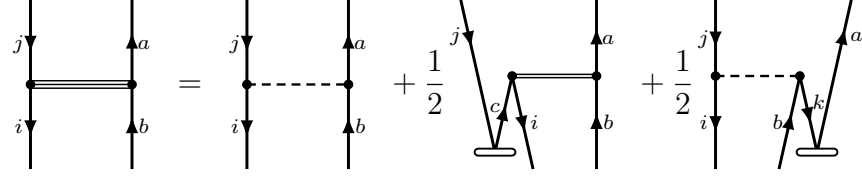
$$X_{cd}^{ab} = X'_{cd}^{ab} + \frac{1}{2} \sum_{kl} V_{cd}^{kl} t_{kl}^{ab} \quad (\text{B.11})$$



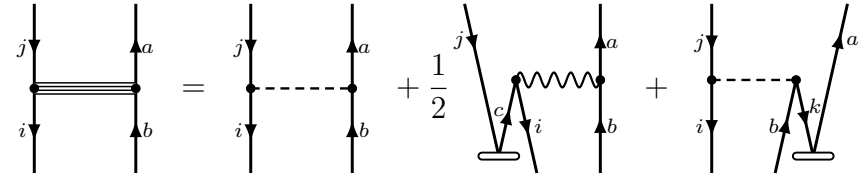
$$X_{kl}^{ij} = V_{kl}^{ij} + \frac{1}{2} \sum_{cd} V_{cd}^{ij} t_{kl}^{cd} + \hat{P}(kl) \sum_c X'_{kc}^{ij} t_l^c \quad (\text{B.12})$$



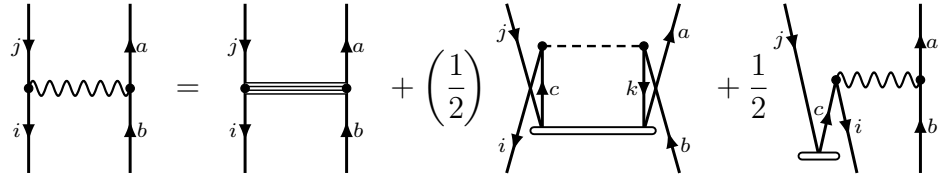
$$X_{jb}^{ia} = V_{jb}^{ia} + \sum_c X_{cb}^{ia} t_j^c - \frac{1}{2} \sum_k V_{jb}^{ik} t_k^a \quad (\text{B.13})$$



$$X''^{ia}_{jb} = V_{jb}^{ia} + \frac{1}{2} \sum_c X_{cb}^{ia} t_j^c - \frac{1}{2} \sum_k V_{jb}^{ik} t_k^a \quad (\text{B.14})$$

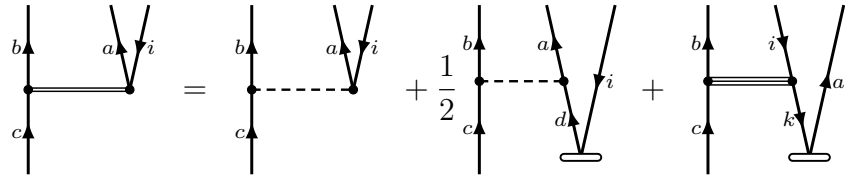


$$X'''^{ia}_{jb} = V_{jb}^{ia} + \frac{1}{2} \sum_c X_{cb}^{ia} t_j^c - \sum_k V_{jb}^{ik} t_k^a \quad (\text{B.15})$$

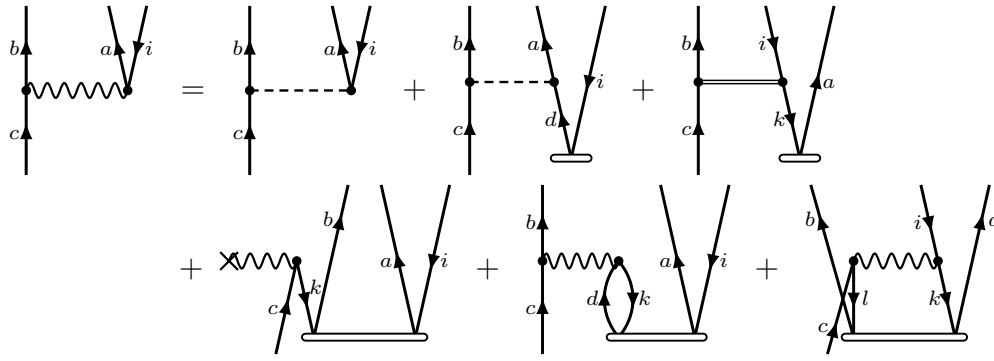


$$X_{jb}^{ia} = X'''^{ia}_{jb} - \left(\frac{1}{2}\right) \sum_{kc} V_{cb}^{ik} t_{jk}^{ca} + \frac{1}{2} \sum_c X_{cb}^{ia} t_j^c \quad (\text{B.16})$$

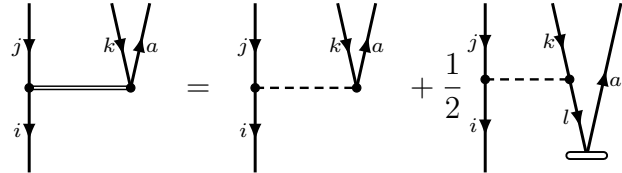
The factor of $\left(\frac{1}{2}\right)$ is applied when solving the CCSD equations but omitted when applying the effective Hamiltonian in post-CC methods.



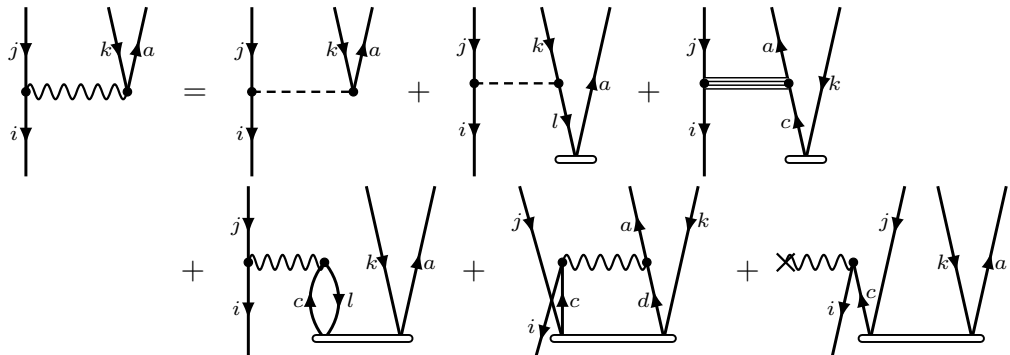
$$X'_{ic}^{ab} = V_{ic}^{ab} + \frac{1}{2} \sum_d V_{dc}^{ab} t_i^d - \hat{P}(ab) \sum_k X''_{ic}^{kb} t_k^a \quad (\text{B.17})$$



$$\begin{aligned}
 X_{ic}^{ab} = & V_{ic}^{ab} + \sum_d V_{dc}^{ab} t_i^d - \hat{P}(ab) \sum_k X'_{ic}^{kb} t_k^a \\
 & - \sum_k X_c^k t_{ik}^{ab} + \hat{P}(ab) \sum_{kd} X_{dc}^{kb} t_{ik}^{ad} + \frac{1}{2} \sum_{kl} X_{ic}^{kl} t_{kl}^{ab}
 \end{aligned} \tag{B.18}$$



$$X_{jk}^{ia} = V_{jk}^{ia} - \frac{1}{2} \sum_l V_{jk}^{il} t_l^a \tag{B.19}$$



$$\begin{aligned}
 X_{jk}^{ia} = & V_{jk}^{ia} - \sum_l V_{jk}^{il} t_l^a + \hat{P}(jk) \sum_c X'''_{jc}^{ia} t_k^c \\
 & + \hat{P}(jk) \sum_{lc} X_{jc}^{il} t_{lk}^{ca} + \frac{1}{2} \sum_{cd} X_{cd}^{ia} t_{jk}^{cd} + \sum_c X_c^i t_{jk}^{ca}
 \end{aligned} \tag{B.20}$$

$$= 0 =$$

$$+ \times \text{ (diagram with a wavy line between a and b, and a dashed line between i and j)} + \times \text{ (diagram with a wavy line between a and b, and a solid line between i and j)} + \times \text{ (diagram with a wavy line between a and b, and a solid line between i and j)} +$$

$$+ \text{ (diagram with a horizontal line between a and b, and a wavy line between i and j)} + \text{ (diagram with a wavy line between a and b, and a horizontal line between i and j)} + \text{ (diagram with a wavy line between a and b, and a horizontal line between i and j)} + \text{ (diagram with a horizontal line between a and b, and a wavy line between i and j)} + \text{ (diagram with a horizontal line between a and b, and a wavy line between i and j)}$$

$$X_{ij}^{ab} = 0 = V_{ij}^{ab} + \hat{P}(ab) \sum_c X_c^a t_{ij}^{cb} - \hat{P}(ij) \sum_k X_i^k t_{kj}^{ab}$$

$$+ \frac{1}{2} \sum_{cd} X'_{cd}^{ab} t_{ij}^{cd} + \frac{1}{2} \sum_{kl} X_{ij}^{kl} t_{kl}^{ab} - \hat{P}(ab|ij) \sum_{kc} X_{ic}^{kb} t_{kj}^{ac} - \hat{P}(ab) \sum_k X'_{ij}^{kb} t_k^a + \hat{P}(ij) \sum_c X'_{ic}^{ab} t_j^c$$
(B.21)

Appendix C

Computational Implementation

The sums involved in building the CC effective Hamiltonian, solving the CC equations, solving the EOM-CC equations, and building effective operators can all be reformulated as matrix-matrix multiplications and thus performed with efficient LAPACK and BLAS routines. To take advantage of this efficiency, the various cluster amplitudes and matrix elements must be grouped into structures with similar index organization so that summed indices map to the same states and matrix elements. An additional benefit to these structures is that angular-momentum-coupling coefficients are automatically removed by summing over Clebsch-Gordon coefficients, see chapter D.

Symmetry Channels

Each matrix structure is separated into different symmetry channels for different permutations of its indices. The channels are denoted as $\Sigma_{\vec{\xi}}$, where $\vec{\xi}$ represents the relevant quantum numbers of a certain channel. There are four different channel types that are relevant for the structures used in this work.

The direct two-body channel categorizes the vector sum of two single-particle-state quantum numbers, $\Sigma_{\vec{\xi}_1}$,

$$\vec{\xi}_{pq} = \vec{\xi}_p + \vec{\xi}_q \quad \longrightarrow \quad |pq\rangle \in \Sigma_{\vec{\xi}_1=\vec{\xi}_{pq}}. \quad (\text{C.1})$$

The cross two-body channel categorizes the vector difference of two single-particle-state

quantum numbers or, equivalently, the vector sum of a single-particle state and a time-reversed single-particle state, $\Sigma_{\vec{\xi}_2}$,

$$\vec{\xi}_{p\bar{q}} = \vec{\xi}_p - \vec{\xi}_q = \vec{\xi}_p + \vec{\xi}_{\bar{q}} \quad \longrightarrow \quad |p\bar{q}\rangle \in \Sigma_{\vec{\xi}_2}. \quad (\text{C.2})$$

The one-body channel categorizes single-particle states by their vector quantum numbers,

$$\Sigma_{\vec{\xi}_3},$$

$$\vec{\xi}_p \quad \longrightarrow \quad |p\rangle \in \Sigma_{\vec{\xi}_3}. \quad (\text{C.3})$$

The cross three-body state categorizes the vector difference between the quantum numbers of a direct two-body state and a single-particle state or, equivalently, the vector sum of the quantum numbers of a two-body direct state and a time-reversed single-particle state, $\Sigma_{\vec{\xi}_3}$,

$$\vec{\xi}_{pq\bar{r}} = \vec{\xi}_p + \vec{\xi}_q - \vec{\xi}_{\bar{r}} = \vec{\xi}_p + \vec{\xi}_q + \vec{\xi}_{\bar{r}} \quad \longrightarrow \quad |pq\bar{r}\rangle \in \Sigma_{\vec{\xi}_3=\vec{\xi}_{pq\bar{r}}}$$

Channel-Partitioned Structures

Different matrix structures are indexed by their channel type: 1 for direct channels, 2 for cross channels, and 3 for one-/three-body channels. For matrices with more than one structure of the same type, there is an additional index that depends on the specific permutation involved.

For a one-body operator $A_q^p \left\{ \hat{a}_p^\dagger \hat{a}_q \right\}$, there is a direct-channel matrix element and a

cross-channel matrix element,

$$\mathbf{A}_1 = A_q^p, \quad \mathbf{A}_2 = A^{p\bar{q}}. \quad (\text{C.5})$$

For a two-body operator $A_{rs}^{pq} \left\{ \hat{a}_p^\dagger \hat{a}_q^\dagger \hat{a}_s \hat{a}_r \right\}$, there is a direct-channel matrix element, four cross-channel matrix elements, and four one-channel matrix elements,

$$\begin{aligned} \mathbf{A}_1 &= A_{rs}^{pq}, \\ \mathbf{A}_{21} &= A_{r\bar{q}}^{p\bar{s}}, \quad \mathbf{A}_{22} = A_{s\bar{p}}^{q\bar{r}}, \quad \mathbf{A}_{23} = A_{s\bar{q}}^{p\bar{r}}, \quad \mathbf{A}_{24} = A_{r\bar{p}}^{q\bar{s}}, \\ \mathbf{A}_{31} &= A_{rs\bar{q}}^p, \quad \mathbf{A}_{32} = A_{rs\bar{p}}^q, \quad \mathbf{A}_{33} = A_r^{pq\bar{s}}, \quad \mathbf{A}_{34} = A_s^{pq\bar{r}}. \end{aligned} \quad (\text{C.6})$$

For an EOM operator of the form $A_r^{pq} \left\{ \hat{a}_p^\dagger \hat{a}_q^\dagger \hat{a}_r \right\}$, there is a direct-channel matrix element, a one-channel matrix element, and two cross-channel matrix elements,

$$\begin{aligned} \mathbf{A}_1 &= A_r^{pq}, \quad \mathbf{A}_3 = A^{pq\bar{r}}, \\ \mathbf{A}_{21} &= A_{r\bar{q}}^p, \quad \mathbf{A}_{22} = A_{r\bar{p}}^q. \end{aligned} \quad (\text{C.7})$$

EOM operators of the form $A_{qr}^p \left\{ \hat{a}_p^\dagger \hat{a}_r \hat{a}_q \right\}$ have similar structures,

$$\begin{aligned} \mathbf{A}_1 &= A_{qr}^p, \quad \mathbf{A}_3 = A_{qr\bar{p}}, \\ \mathbf{A}_{21} &= A_q^{p\bar{r}}, \quad \mathbf{A}_{22} = A_r^{p\bar{q}}. \end{aligned} \quad (\text{C.8})$$

$$\text{Matrix Form of } \bar{H} = \left(\hat{H}_N e^{\hat{T}} \right)_c$$

$$X_a^i = \lceil f_a^i \rceil + V_{c\bar{k}}^{i\bar{a}} t^{c\bar{k}} \\ \mathbf{X}_2^{hp} \leftarrow \lceil \mathbf{f}_2^{hp} \rceil + \mathbf{V}_{23}^{hhpp} \cdot \mathbf{t}_2 \quad (\text{C.9})$$

$$X_b^a = f_b^a - \frac{1}{2} t_{kl\bar{c}}^a V_b^{kl\bar{c}} + V_{c\bar{k}}^{a\bar{b}} t^{c\bar{k}} - t_k^a X_b^k \\ \mathbf{X}_3^{pp} \leftarrow -\frac{1}{2} \mathbf{t}_{31} \cdot \mathbf{V}_{33}^{hhpp} - \mathbf{t}_3 \cdot \mathbf{X}_3^{hp} \\ \mathbf{X}_2^{pp} \leftarrow \mathbf{f}_2^{pp} + \mathbf{V}_{24}^{hPPP} \cdot \mathbf{t}_2 \quad (\text{C.10})$$

$$X_j'^i = f_j^i + \frac{1}{2} V_{cd\bar{k}}^i t_j^{cd\bar{k}} + V_{c\bar{k}}^{i\bar{j}} t^{c\bar{k}} \\ \mathbf{X}'_3^{hh} \leftarrow \frac{1}{2} \mathbf{V}_{31}^{hhpp} \cdot \mathbf{t}_{33} \\ \mathbf{X}'_2^{hh} \leftarrow \mathbf{f}_2^{hh} + \mathbf{V}_{23}^{hhhp} \cdot \mathbf{t}_2 \quad (\text{C.11})$$

$$X_j^i = f_j^i + \frac{1}{2} V_{cd\bar{k}}^i t_j^{cd\bar{k}} + V_{c\bar{k}}^{i\bar{j}} t^{c\bar{k}} + X_c^i t_j^c \\ \mathbf{X}_3^{hh} \leftarrow \frac{1}{2} \mathbf{V}_{31}^{hhpp} \cdot \mathbf{t}_{33} + \mathbf{X}_3^{hp} \cdot \mathbf{t}_3 \\ \mathbf{X}'_2^{hh} \leftarrow \mathbf{f}_2^{hh} + \mathbf{V}_{23}^{hhhp} \cdot \mathbf{t}_2 \quad (\text{C.12})$$

$$\begin{aligned}
X_i^a &= \lceil f_i^a \rceil + X_c^a t_i^c - t_k^a X_i'^k - V_{ck}^{a\bar{i}} t^{c\bar{k}} + \frac{1}{2} V_{cd\bar{k}}^a t_i^{cd\bar{k}} - \frac{1}{2} t_{kl\bar{c}}^a V_i^{kl\bar{c}} + t_{k\bar{c}}^{a\bar{i}} X^{k\bar{c}} \\
\mathbf{X}_3^{ph} &\leftarrow \mathbf{X}_3^{pp} \cdot \mathbf{t}_3 - \mathbf{t}_3 \cdot \mathbf{X}_3'^{hh} + \frac{1}{2} \mathbf{V}_{32}^{hppp} \cdot \mathbf{t}_{34} - \frac{1}{2} \mathbf{t}_{31} \cdot \mathbf{V}_{33}^{hhhp} \\
\mathbf{X}_2^{ph} &\leftarrow \lceil \mathbf{f}_2^{ph} \rceil - \mathbf{V}_{22}^{hphp} \cdot \mathbf{t}_2 + \mathbf{t}_{23} \cdot \mathbf{X}_2^{hp}
\end{aligned} \tag{C.13}$$

$$\begin{aligned}
X_{bc}'^{ia} &= V_{bc}^{ia} - \frac{1}{2} t_k^a V_{bc\bar{i}}^k \\
\mathbf{X}_{32}'^{hppp} &\leftarrow \mathbf{V}_{32}^{hppp} - \frac{1}{2} \mathbf{t}_3 \cdot \mathbf{V}_{32}^{hhpp}
\end{aligned} \tag{C.14}$$

$$\begin{aligned}
X_{bc}^{ia} &= V_{bc}^{ia} - t_k^a V_{bc\bar{i}}^k \\
\mathbf{X}_{32}^{hppp} &\leftarrow \mathbf{V}_{32}^{hppp} - \mathbf{t}_3 \cdot \mathbf{V}_{32}^{hhpp}
\end{aligned} \tag{C.15}$$

$$\begin{aligned}
X_{ka}^{ij} &= V_{ka}^{ij} + \frac{1}{2} V_c^{ij\bar{a}} t_k^c \\
\mathbf{X}_{33}^{hhhp} &\leftarrow \mathbf{V}_{ka}^{ij} + \frac{1}{2} \mathbf{V}_{33}^{hhpp} \cdot \mathbf{t}_3
\end{aligned} \tag{C.16}$$

$$\begin{aligned}
X_{ka}^{ij} &= V_{ka}^{ij} + V_c^{ij\bar{a}} t_k^c \\
\mathbf{X}_{33}^{hhhp} &\leftarrow \mathbf{V}_{ka}^{ij} + \mathbf{V}_{33}^{hhpp} \cdot \mathbf{t}_3
\end{aligned} \tag{C.17}$$

$$\begin{aligned}
X'_{cd}^{ab} &= V_{cd}^{ab} - \hat{P}(ab) t_k^a X'_{cd\bar{b}}^{lk} \\
\mathbf{X}'_1^{pppp} &\leftarrow \mathbf{V}_1^{pppp} \\
\mathbf{X}'_{3(2)}^{pppp} &\leftarrow \mp \mathbf{t}_3 \cdot \mathbf{X}'_{31}^{hppp}
\end{aligned} \tag{C.18}$$

$$\begin{aligned}
X_{cd}^{ab} &= X'_{cd}^{ab} + \frac{1}{2} t_{kl}^{ab} V_{cd}^{kl} \\
\mathbf{X}_1^{pppp} &\leftarrow \mathbf{X}'_1^{pppp} + \frac{1}{2} \mathbf{t}_1 \cdot \mathbf{V}_1^{happ}
\end{aligned} \tag{C.19}$$

$$\begin{aligned}
X_{kl}^{ij} &= V_{kl}^{ij} + \frac{1}{2} V_{cd}^{ij} t_{kl}^{cd} + \hat{P}(kl) X_c^{ij\bar{k}} t_l^c \\
\mathbf{X}_1^{hhhh} &\leftarrow \mathbf{V}_1^{hhhh} + \frac{1}{2} \mathbf{V}_1^{happ} \cdot \mathbf{t}_1 \\
\mathbf{X}_{3(4)}^{hhhh} &\leftarrow \mp \mathbf{X}'_{34}^{hhhp} \cdot \mathbf{t}_3
\end{aligned} \tag{C.20}$$

$$\begin{aligned}
X_{jb}^{ia} &= V_{jb}^{ia} + X_c^{i\bar{a}\bar{b}} t_j^c - \frac{1}{2} t_k^a V_{j\bar{b}\bar{i}}^k \\
\mathbf{X}'_{21}^{hphp} &\leftarrow \mathbf{V}_{21}^{hphp} \\
\mathbf{X}'_{33}^{hphp} &\leftarrow \mathbf{X}'_{33}^{hphp} \cdot \mathbf{t}_3 \\
\mathbf{X}'_{32}^{hphp} &\leftarrow -\frac{1}{2} \mathbf{t}_3 \cdot \mathbf{V}_{32}^{happ}
\end{aligned} \tag{C.21}$$

$$\begin{aligned}
X''_{j\bar{b}}^{ia} &= V_{j\bar{b}}^{ia} + \frac{1}{2} X_c'^{i\bar{a}\bar{b}} t_j^c - \frac{1}{2} t_k^a V_{j\bar{b}\bar{a}}^k \\
\mathbf{X}''_{2_1}^{hphp} &\leftarrow \mathbf{V}_{2_1}^{hphp} \\
\mathbf{X}''_{3_3}^{hphp} &\leftarrow \frac{1}{2} \mathbf{X}'_{3_3}^{hppp} \cdot \mathbf{t}_3 \\
\mathbf{X}''_{3_2}^{hphp} &\leftarrow -\frac{1}{2} \mathbf{t}_3 \cdot \mathbf{V}_{3_2}^{hhhp} \tag{C.22}
\end{aligned}$$

$$\begin{aligned}
X'''_{j\bar{b}}^{ia} &= V_{j\bar{b}}^{ia} + \frac{1}{2} X_c'^{i\bar{a}\bar{b}} t_j^c - t_k^a V_{j\bar{b}\bar{a}}^k \\
\mathbf{X}'''_{2_1}^{hphp} &\leftarrow \mathbf{V}_{2_1}^{hphp} \\
\mathbf{X}'''_{3_3}^{hphp} &\leftarrow \frac{1}{2} \mathbf{X}'_{3_3}^{hppp} \cdot \mathbf{t}_3 \\
\mathbf{X}'''_{3_2}^{hphp} &\leftarrow -\mathbf{t}_3 \cdot \mathbf{V}_{3_2}^{hhhp} \tag{C.23}
\end{aligned}$$

$$\begin{aligned}
X_{j\bar{b}}^{ia} &= V_{j\bar{b}}^{ia} + X_c'^{i\bar{a}\bar{b}} t_j^c - t_k^a V_{j\bar{b}\bar{a}}^k - \left(\frac{1}{2}\right) V_{c\bar{k}}^{i\bar{b}} t_{j\bar{a}}^{c\bar{k}} \\
\mathbf{X}_{2_1}^{hphp} &\leftarrow \mathbf{V}_{2_1}^{hphp} - \left(\frac{1}{2}\right) \mathbf{V}_{2_1}^{hhhp} \mathbf{t}_{2_1} \\
\mathbf{X}_{3_3}^{hphp} &\leftarrow \mathbf{X}_{3_3}^{hppp} \cdot \mathbf{t}_3 \\
\mathbf{X}_{3_2}^{hphp} &\leftarrow -\mathbf{t}_3 \cdot \mathbf{V}_{3_2}^{hhhp} \tag{C.24}
\end{aligned}$$

$$\begin{aligned}
X'_{ic}^{ab} &= V_{ic}^{ab} + \frac{1}{2} V_d^{ab\bar{c}} t_i^d - \hat{P}(ab) t_k^a X''_{ic\bar{b}}^{ik} \\
\mathbf{X}'_{3_3}^{pphp} &\leftarrow \mathbf{V}_{3_3}^{pphp} + \frac{1}{2} \mathbf{V}_{3_3}^{pppp} \cdot \mathbf{t}_3 \\
\mathbf{X}'_{3_{1(2)}}^{pphp} &\leftarrow \mp \mathbf{t}_3 \cdot \mathbf{X}''_{3_1}^{hphp} \tag{C.25}
\end{aligned}$$

$$\begin{aligned}
X_{ic}^{ab} &= V_{ic}^{ab} + V_d^{ab\bar{c}} \mathbf{t}_i^d - \hat{P}(ab) t_k^a X_{ic\bar{b}}'^k - t_k^{ab\bar{i}} X_c^k + \hat{P}(ab) t_{k\bar{d}}^{a\bar{i}} X_{c\bar{b}}^{k\bar{d}} + \frac{1}{2} t_{kl}^{ab} X_{ic}^{kl} \\
\mathbf{X}_{3_3}^{pphp} &\leftarrow \mathbf{V}_{3_3}^{pphp} + \mathbf{V}_{3_3}^{pppp} \cdot \mathbf{t}_3 \\
\mathbf{X}_{3_{1(2)}}^{pphp} &\leftarrow \mp \mathbf{t}_3 \cdot \mathbf{X}_{3_1}^{hphp} \\
\mathbf{X}_{3_4}^{pphp} &\leftarrow -\mathbf{t}_{3_4} \cdot \mathbf{X}_3^{hp} \\
\mathbf{X}_{2_{2(3)}}^{pphp} &\leftarrow \mp \mathbf{t}_{2_3} \cdot \mathbf{X}_{2_3}^{hphh} \\
\mathbf{X}_1^{pphp} &\leftarrow \frac{1}{2} \mathbf{t}_1 \cdot \mathbf{X}_1^{hhhp} \tag{C.26}
\end{aligned}$$

$$\begin{aligned}
X_{jk}'^{ia} &= V_{jk}^{ia} - \frac{1}{2} t_l^a V_{jk\bar{i}}^l \\
\mathbf{X}_{3_2}^{hphh} &\leftarrow \mathbf{V}_{3_2}^{hphh} - \frac{1}{2} \mathbf{t}_3 \cdot \mathbf{V}_{3_2}^{hhhh} \tag{C.27}
\end{aligned}$$

$$\begin{aligned}
X_{jk}^{ia} &= V_{jk}^{ia} - t_l^a V_{jk\bar{i}}^l + \hat{P}(jk) X_{c\bar{l}}'''^{ia\bar{j}} t_k^c + \hat{P}(jk) X_{c\bar{l}}^{i\bar{j}} t_{k\bar{a}}^{c\bar{l}} + \frac{1}{2} X_{cd}^{ia} t_{jk}^{cd} + X_{cd}^i t_{jk}^c \\
\mathbf{X}_{3_2}^{hphh} &\leftarrow \mathbf{V}_{3_2}^{hphh} - \mathbf{t}_3 \cdot \mathbf{V}_{3_2}^{hhhh} \\
\mathbf{X}_{3_{3(4)}}^{hphh} &\leftarrow \mp \mathbf{X}_{3_4}'''^{hphp} \cdot \mathbf{t}_3 \\
\mathbf{X}_{2_{1(3)}}^{hphh} &\leftarrow \mp \mathbf{X}_{2_3}^{hhhp} \cdot \mathbf{t}_{2_3} \\
\mathbf{X}_1^{hphh} &\leftarrow \frac{1}{2} \mathbf{X}_1^{hphh} \cdot \mathbf{t}_1 \\
\mathbf{X}_{3_1}^{hphh} &\leftarrow \mathbf{X}_3^{hp} \cdot \mathbf{t}_{3_1} \tag{C.28}
\end{aligned}$$

$$\begin{aligned}
X_{ij}^{ab} &= V_{ij}^{ab} + \hat{P}(ab) X_c^a t_{ij\bar{b}}^c - \hat{P}(ij) t_k^{ab\bar{j}} X_i^k + \frac{1}{2} X_{cd}^{tab} t_{ij}^{cd} + \frac{1}{2} t_{kl}^{ab} X_{ij}^{kl} \\
&\quad - \hat{P}(ab|ij) t_{k\bar{c}}^{a\bar{j}} X_{i\bar{b}}^{k\bar{c}} - \hat{P}(ab) t_k^a X_{ij\bar{b}}^{ik} + \hat{P}(ij) X_c'^{ab\bar{i}} t_j^c \\
\mathbf{X}_1^{pphh} &\leftarrow \mathbf{V}_1^{pphh} + \frac{1}{2} \mathbf{X}'_1^{pppp} \cdot \mathbf{t}_1 + \frac{1}{2} \mathbf{t}_1 \cdot \mathbf{X}_1^{hhhh} \\
\mathbf{X}_{3_{1(2)}}^{pphh} &\leftarrow \pm \mathbf{X}_3^{pp} \cdot \mathbf{t}_{3_1} \mp \mathbf{t}_3 \mathbf{X}'_{3_1}^{hpjh} \\
\mathbf{X}_{3_{3(4)}}^{pphh} &\leftarrow \mp \mathbf{t}_{3_3} \cdot \mathbf{X}_3^{hh} \pm \mathbf{X}'_{3_4}^{pphp} \mathbf{t}_3 \\
\mathbf{X}_{2_{1(2)}}^{pphh} &\leftarrow -\mathbf{t}_{2_1} \cdot \mathbf{X}_{2_1}^{hpjh} \\
\mathbf{X}_{2_{3(4)}}^{pphh} &\leftarrow \mathbf{t}_{2_1} \cdot \mathbf{X}_{2_1}^{hpjh}
\end{aligned} \tag{C.29}$$

Matrix Form of $\left(\bar{H}_N \hat{R}_\mu^{A+1} \right)_c = \omega_\mu \hat{R}_\mu^{A+1}$

$$\begin{aligned}
\omega_k r^a &= X_c^a r^c + r_{k\bar{c}}^a X^{k\bar{c}} - \frac{1}{2} X_{cd\bar{k}}^a r^{cd\bar{k}} \\
\omega_k \mathbf{r} &\leftarrow \mathbf{X}_3^{pp} \cdot \mathbf{r} + \mathbf{r}_{2_1} \cdot \mathbf{X}_2^{hp} - \frac{1}{2} \mathbf{X}_{3_2}^{hppp} \cdot \mathbf{r}_3
\end{aligned} \tag{C.30}$$

$$\begin{aligned}
\omega_k r_i^{ab} &= -X_c^{ab\bar{i}} r^c + \hat{P}(ab) X_c^b r_{i\bar{a}}^c - r_k^{ab} X_i^k + \frac{1}{2} X_{cd}^{ab} r_i^{cd} - \hat{P}(ab) r_{k\bar{c}}^b X_{i\bar{a}}^{k\bar{c}} - \frac{1}{2} t_k^{ab\bar{i}} V_{cd\bar{l}}^k r^{cd\bar{l}} \\
\omega_k \mathbf{r}_3 &\leftarrow -\mathbf{X}_{3_4}^{pphp} \cdot \mathbf{r} - \frac{1}{2} \mathbf{t}_{3_3} \cdot \mathbf{V}_{3_1}^{happ} \cdot \mathbf{r}_3 \\
\omega_k \mathbf{r}_{2_{1(2)}} &\leftarrow \mp \mathbf{X}_3^{pp} \cdot \mathbf{r}_{2_2} \pm \mathbf{r}_{2_2} \cdot \mathbf{X}_{2_1}^{hpjh} \\
\omega_k \mathbf{r}_1 &\leftarrow -\mathbf{r}_1 \cdot \mathbf{X}_3^{hh} + \frac{1}{2} \mathbf{X}_1^{pppp} \cdot \mathbf{r}_1
\end{aligned} \tag{C.31}$$

Matrix Form of $\hat{L}_\mu^{A+1} \bar{H}_N = E_\mu \hat{L}_\mu^{A+1}$

One main difference for the left eigenproblem is that the disconnected term is computed as an outer product rather than with matrix-matrix multiplication.

$$\begin{aligned} E_k l_a &= l_c X_a^c - \frac{1}{2} l_{cd\bar{k}} X_a^{cd\bar{k}} \\ E_k \mathbf{l} &\leftarrow \mathbf{l} \cdot \mathbf{X}_3^{pp} - \frac{1}{2} \mathbf{l}_3 \cdot \mathbf{X}_{3_4}^{pphp} \end{aligned} \quad (\text{C.32})$$

$$\begin{aligned} E_k l_{ab}^i &= \hat{P}(ab) l_a X^{i\bar{b}} - l_c X_{a\bar{b}}^c - X_k^i l_{ab}^k + \hat{P}(ab) l_c^{i\bar{a}} X_b^c + \frac{1}{2} l_{cd}^i X_{ab}^{cd} \\ &\quad - \hat{P}(ab) X_{k\bar{c}}^{i\bar{a}} l_b^{k\bar{c}} - \frac{1}{2} l_{cd\bar{l}} t_k^{cd\bar{l}} V_{a\bar{b}\bar{i}}^k \\ E_k l_3 &\leftarrow -\mathbf{l} \cdot \mathbf{X}_{3_2}^{happ} - \frac{1}{2} \mathbf{l}_3 \cdot \mathbf{t}_{3_3} \cdot \mathbf{V}_{3_1}^{hhpp} \\ E_k \mathbf{l}_{2_{1(2)}} &\leftarrow \pm \mathbf{l} \otimes \mathbf{X}_2^{hp} \mp \mathbf{l}_{2_2} \cdot \mathbf{X}_3^{pp} \pm \mathbf{X}_{2_1}^{hphp} \cdot \mathbf{l}_{2_2} \\ E_k \mathbf{l}_1 &\leftarrow -\mathbf{X}_3^{hh} \cdot \mathbf{l}_1 + \frac{1}{2} \mathbf{l}_1 \cdot \mathbf{X}_1^{pppp} \end{aligned} \quad (\text{C.33})$$

Matrix Form of $\left(\bar{H}_N \hat{R}_\mu^{A-1} \right)_c = \omega_\mu \hat{R}_\mu^{A-1}$

$$\begin{aligned} \omega_k r_i &= -r_k X_i^k + X_{c\bar{k}} r_i^{c\bar{k}} - \frac{1}{2} r_{kl\bar{c}} X_i^{kl\bar{c}} \\ \omega_k \mathbf{r} &\leftarrow -\mathbf{r} \cdot \mathbf{X}_3^{hh} + \mathbf{X}_{2'}^{hp} \cdot \mathbf{r}_{2_1} - \frac{1}{2} \mathbf{r}_3 \cdot \mathbf{X}_{3_3}^{hhhp} \end{aligned} \quad (\text{C.34})$$

$$\begin{aligned}
\omega_k r_{ij}^a &= -r_k X_{ij\bar{a}}^k - \hat{P}(ij) r_k^{a\bar{i}} X_j^k + X_c^a r_{ij}^c + \frac{1}{2} r_{kl}^a X_{ij}^{kl} - \hat{P}(ij) X_{c\bar{k}}^{a\bar{i}} r_j^{c\bar{k}} - \frac{1}{2} r_{kl\bar{d}} V_c^{kl\bar{d}} t_{ij\bar{a}}^c \\
\omega_k \mathbf{r}_3 &\leftarrow -\mathbf{r} \cdot \mathbf{X}_{31}^{hphh} - \frac{1}{2} \mathbf{r}_3 \cdot \mathbf{V}_{33}^{hhpp} \cdot \mathbf{t}_{31} \\
\omega_k \mathbf{r}_{2(2)} &\leftarrow \pm \mathbf{r}_{22} \cdot \mathbf{X}_3^{hh} \pm \mathbf{X}_{22}^{hphp} \cdot \mathbf{r}_{22} \\
\omega_k \mathbf{r}_1 &\leftarrow \mathbf{X}_3^{pp} \cdot \mathbf{r}_1 + \frac{1}{2} \mathbf{r}_1 \cdot \mathbf{X}_1^{hhhh}
\end{aligned} \tag{C.35}$$

Matrix Form of $\hat{L}_\mu^{A-1} \bar{H}_N = E_\mu \hat{L}_\mu^{A-1}$

Again, the disconnected term is computed as an outer product rather than with matrix-matrix multiplication.

$$\begin{aligned}
E_k l^i &= -X_k^i l^k - \frac{1}{2} X_{kl\bar{c}}^i l^{kl\bar{c}} \\
E_k \mathbf{l} &\leftarrow -\mathbf{X}_3^{HH} \cdot \mathbf{l} - \frac{1}{2} \mathbf{X}_{31}^{hphh} \cdot \mathbf{l}_3
\end{aligned} \tag{C.36}$$

$$\begin{aligned}
E_k l_a^{ij} &= \hat{P}(ij) l^i X_{a\bar{j}} - X_k^{ij\bar{a}} l^k + l_c^{ij} X_a^c - \hat{P}(ij) X_k^j l_{a\bar{i}}^k + \frac{1}{2} X_{kl}^{ij} l_a^{kl} \\
&\quad - \hat{P}(ij) l_{c\bar{k}}^j X_{a\bar{i}}^{c\bar{k}} - \frac{1}{2} V_c^{ij\bar{a}} t_{kl\bar{d}}^c l^{kl\bar{d}} \\
E_k l_3 &\leftarrow -\mathbf{X}_{33}^{hhhp} \cdot \mathbf{l} - \frac{1}{2} \mathbf{V}_{33}^{hhpp} \cdot \mathbf{t}_{31} \cdot \mathbf{l}_3 \\
E_k \mathbf{l}_{2(2)} &\leftarrow \pm \mathbf{l} \otimes \mathbf{X}_{2'}^{hp} \pm \mathbf{X}_3^{hh} \cdot \mathbf{l}_{22} \pm \mathbf{l}_{22} \cdot \mathbf{X}_{22}^{hphp} \\
E_k \mathbf{l}_1 &\leftarrow \mathbf{l}_1 \cdot \mathbf{X}_3^{pp} + \frac{1}{2} \mathbf{X}_1^{hhhh} \cdot \mathbf{l}_1
\end{aligned} \tag{C.37}$$

Appendix D

Angular Momentum Coupling

Before deriving useful equations for J-scheme angular momentum coupling, it's necessary to list some shorthand notations, definitions, and useful relationships:

$$\hat{p} \equiv \sqrt{2j_p + 1} \quad (\text{D.1})$$

$$\sum_{\{m\}} \equiv \text{sum over all } m \quad (\text{D.2})$$

Clebsch-Gordan coefficients:

$$\langle pq|J\rangle \equiv \langle j_p m_p; j_q m_q | JM \rangle \quad (\text{D.3})$$

$$\langle p\bar{q}|J\rangle \equiv \langle j_p, m_p; j_q, -m_q | JM \rangle (-1)^{(q-m_q)} \quad (\text{D.4})$$

$$\sum_{JM} \langle pq|J\rangle \langle p'q'|J\rangle = \delta_{m_p m_{p'}} \delta_{m_q m_{q'}} \quad (\text{D.5})$$

$$\sum_{m_p m_q} \langle pq|J\rangle \langle pq|J'\rangle = \delta_{JJ'} \delta_{MM'} \quad (\text{D.6})$$

$$(\text{D.7})$$

Clebsch-Gordan coefficient symmetries:

$$\langle j_p m_p; j_q m_q | JM \rangle = (-1)^{j_p + j_q - J} \langle j_p m_p; j_q m_q | JM \rangle \quad (\text{D.8})$$

$$= (-1)^{j_p + j_q - J} \langle j_q m_q; j_p m_p | JM \rangle \quad (\text{D.9})$$

$$= (-1)^{j_p - m_p} \frac{\hat{J}}{\hat{q}} \langle j_p m_p; J - M | j_q - m_q \rangle \quad (\text{D.10})$$

$$= (-1)^{j_q + m_q} \frac{\hat{J}}{\hat{p}} \langle J - M; j_q m_q | j_p - m_p \rangle \quad (\text{D.11})$$

$$= (-1)^{j_p - m_p} \frac{\hat{J}}{\hat{q}} \langle JM; j_p - m_p | j_q m_q \rangle \quad (\text{D.12})$$

$$= (-1)^{j_q + m_q} \frac{\hat{J}}{\hat{p}} \langle j_q - m_q; JM | j_p m_p \rangle \quad (\text{D.13})$$

Six-J symbols:

$$\begin{Bmatrix} p & q & r \\ s & t & u \end{Bmatrix} \equiv \begin{Bmatrix} j_p & j_q & j_r \\ j_s & j_t & j_u \end{Bmatrix} \quad (\text{D.14})$$

$$\sum_{j_3} \hat{j}_3^2 \begin{Bmatrix} j_1 & j_2 & j_3 \\ j_4 & j_5 & j_6 \end{Bmatrix} \begin{Bmatrix} j_1 & j_2 & j_3 \\ j_4 & j_5 & j'_6 \end{Bmatrix} = \frac{\delta_{j_6 j'_6}}{\hat{j}_3^2} \quad (\text{D.15})$$

$$\sum_{M'} \langle p\bar{s}|J' \rangle \langle r\bar{q}|J' \rangle = \hat{J}'^2 \sum_{JM} \begin{Bmatrix} p & q & J \\ r & s & J' \end{Bmatrix} \langle pq|J \rangle \langle rs|J \rangle \quad (\text{D.16})$$

$$\sum_M \langle pq|J \rangle \langle rs|J \rangle = \hat{J}^2 \sum_{J'M'} \begin{Bmatrix} p & q & J \\ r & s & J' \end{Bmatrix} \langle p\bar{s}|J' \rangle \langle r\bar{q}|J' \rangle \quad (\text{D.17})$$

Two-body, scalar J-scheme matrix elements ($\hat{T}, \hat{H}, \bar{H}$), in terms of M-scheme matrix

elements:

$$X_{rsJ}^{pqJ} = \sum_{\{m\}} X_{rm_r s m_s}^{pmpq m q} \langle pq|J\rangle \langle rs|J\rangle \quad (\text{D.18})$$

$$X_{r\bar{q}J'}^{p\bar{s}J'} = \sum_{\{m\}} X_{rm_r s m_s}^{pmpq m q} \langle p\bar{s}|J'\rangle \langle r\bar{q}|J'\rangle \quad (\text{D.19})$$

$$X_{rsJ\bar{q}}^p = \sum_{\{m\}} X_{rm_r s m_s}^{pmpq m q} \langle rs|J\rangle \langle J\bar{q}|p\rangle \quad (\text{D.20})$$

$$X_r^{pqJ\bar{s}} = \sum_{\{m\}} X_{rm_r s m_s}^{pmpq m q} \langle pq|J\rangle \langle J\bar{s}|r\rangle \quad (\text{D.21})$$

Two-body M-scheme matrix elements in terms of J-scheme, scalar matrix elements:

$$X_{rm_r s m_s}^{pmpq m q} = \sum_{JM} X_{rsJ}^{pqJ} \langle pq|J\rangle \langle rs|J\rangle \quad (\text{D.22})$$

$$= \sum_{J'M'} X_{r\bar{q}J'}^{p\bar{s}J'} \langle p\bar{s}|J'\rangle \langle r\bar{q}|J'\rangle \quad (\text{D.23})$$

$$= \sum_{JM} X_{rsJ\bar{q}}^p \langle rs|J\rangle \langle J\bar{q}|p\rangle \quad (\text{D.24})$$

$$= \sum_{JM} X_r^{pqJ\bar{s}} \langle pq|J\rangle \langle J\bar{s}|r\rangle \quad (\text{D.25})$$

To find the relationship between the scalar matrix elements of \hat{T} , \hat{H} , and \bar{H} with different couplings, the M-scheme expressions are written in terms of their different couplings, then the Clebsch-Gordon coefficients are reorganized using Eqs. (D.8)–(D.17) so that they have the same form. A few examples of this recoupling are shown below with the relevant equation used at each step. The shorthand $X \equiv X_{rm_r s m_s}^{pmpq m q}$ is used for clarity. The relationship

between X_{rsJ}^{pqJ} and $X_{r\bar{q}J'}^{p\bar{s}J'}$ is,

$$X_{rsJ}^{pqJ} = \sum_{M\{m\}} X \langle pq|J\rangle \langle rs|J\rangle = \sum_{J'M'\{m\}} X \hat{J}^2 \begin{Bmatrix} p & q & J \\ r & s & J' \end{Bmatrix} \langle p\bar{s}|J'\rangle \langle r\bar{q}|J'\rangle \quad (\text{D.17})$$

$$= \sum_J X_{r\bar{q}J'}^{p\bar{s}J'} \hat{J}^2 \begin{Bmatrix} p & q & J \\ r & s & J' \end{Bmatrix} \quad (\text{D.19}) \quad (\text{D.26})$$

As another example, the relationship between X_{rsJ}^{pqJ} and $X_{rsJ\bar{q}}^p$ is,

$$X_{rsJ}^{pqJ} = \sum_{\{m\}} X \langle pq|J\rangle \langle rs|J\rangle = \sum_{\{m\}} X \langle qp|J\rangle \langle rs|J\rangle (-1)^{jp+jq-J} \quad (\text{D.9})$$

$$= \sum_{\{m\}} X \frac{\hat{J}}{\hat{p}} \langle J\bar{q}|p\rangle \langle rs|J\rangle (-1)^{jp+jq-J} \quad (\text{D.12})$$

$$= X_{rsJ\bar{q}}^p \frac{\hat{J}}{\hat{p}} (-1)^{jp+jq-J} \quad (\text{D.19}) \quad (\text{D.27})$$

When sums are formulated in the terms of channel-partitioned matrices like those in sections 3.4.2 and C, the factors related to a structure's angular momentum coupling are automatically summed with the identity Eq. (D.6). To demonstrate this, an example is shown here. First, from the CCSD equations the sum in Eq. (3.44) is rewritten in terms of the J-scheme structures. The indices represent single-particle states in the M-scheme

expression but represent degenerate shells in J-scheme,

$$\begin{aligned}
& \frac{1}{2} \sum_{klcd} V_{cd}^{kl} t_{ij}^{db} t_{kl}^{ca} \longrightarrow \frac{1}{2} \sum_{\substack{klcd \\ J_1 J_2 J_3 \\ \{m\}}} t_{kl}^a J_{1\bar{c}} \langle kl | J_1 \rangle \langle J_1 \bar{c} | a \rangle V_d^{kl} J_2 \bar{c} \langle kl | J_2 \rangle \langle J_2 \bar{c} | d \rangle t_{ij}^d J_{3\bar{b}} \langle ij | J_3 \rangle \langle J_3 \bar{b} | d \rangle \\
&= \frac{1}{2} \sum_{\substack{klcd \\ J_1 J_2 J_3 \\ \{m\}}} t_{kl}^a J_{1\bar{c}} V_d^{kl} J_2 \bar{c} t_{ij}^d J_{3\bar{b}} \left[\sum_{m_k m_l} \langle kl | J_1 \rangle \langle kl | J_2 \rangle \right] \langle J_1 \bar{c} | a \rangle \langle J_2 \bar{c} | d \rangle \langle ij | J_3 \rangle \langle J_3 \bar{b} | d \rangle \\
&= \frac{1}{2} \sum_{\substack{klcd \\ J_1 J_2 J_3 \\ \{m\}}} t_{kl}^a J_{1\bar{c}} V_d^{kl} J_2 \bar{c} t_{ij}^d J_{3\bar{b}} \left[\delta_{J_1 J_2} \delta_{M_1 M_2} \right] \langle J_1 \bar{c} | a \rangle \langle J_2 \bar{c} | d \rangle \langle ij | J_3 \rangle \langle J_3 \bar{b} | d \rangle \\
&= \frac{1}{2} \sum_{\substack{klcd \\ J_1 J_3 \\ \{m\}}} t_{kl}^a J_{1\bar{c}} V_d^{kl} J_1 \bar{c} t_{ij}^d J_{3\bar{b}} \left[\sum_{M_1 m_c} \langle J_1 \bar{c} | a \rangle \langle J_1 \bar{c} | d \rangle \right] \langle ij | J_3 \rangle \langle J_3 \bar{b} | d \rangle \\
&= \frac{1}{2} \sum_{\substack{klcd \\ J_1 J_3 \\ \{m\}}} t_{kl}^a J_{1\bar{c}} V_d^{kl} J_1 \bar{c} t_{ij}^d J_{3\bar{b}} \left[\delta_{jajd} \delta_{mam_d} \right] \langle ij | J_3 \rangle \langle J_3 \bar{b} | d \rangle \\
&= \frac{1}{2} \sum_{\substack{klcd \\ J_1 J_3 \\ \{m\}}} t_{kl}^a J_{1\bar{c}} V_d^{kl} J_1 \bar{c} t_{ij}^d J_{3\bar{b}} \langle ij | J_3 \rangle \langle J_3 \bar{b} | a \rangle
\end{aligned} \tag{D.28}$$

This final form has the same structure as Eq. (D.24) so that the sum can be collected into the following structure with no angular-momenutm coupling coefficients,

$$t_{ij}^a J_{\bar{b}} \leftarrow \frac{1}{2} \sum_{\substack{klcd \\ J_1 J_3}} t_{kl}^a J_{1\bar{c}} V_d^{kl} J_1 \bar{c} t_{ij}^d J_{3\bar{b}}. \tag{D.29}$$

Amplitudes of different coupling structures are then gathered using relationships like those in Eq. (D.26) and (D.27).

REFERENCES

REFERENCES

- [1] H. Hergert, “Private communication.”
- [2] M. Shao, H. M. Aktulga, C. Yang, E. G. Ng, P. Maris, and J. P. Vary, “Accelerating nuclear configuration interaction calculations through a preconditioned block iterative eigensolver,” *CoRR*, vol. abs/1609.01689, 2016.
- [3] P. López Ríos, A. Ma, N. D. Drummond, M. D. Towler, and R. J. Needs, “Inhomogeneous backflow transformations in quantum monte carlo calculations,” *Phys. Rev. E*, vol. 74, p. 066701, Dec 2006.
- [4] R. Machleidt, “Chiral symmetry and the nucleon-nucleon interaction,” *Symmetry*, vol. 8, no. 4, 2016.
- [5] K. A. Brueckner and C. A. Levinson, “Approximate reduction of the many-body problem for strongly interacting particles to a problem of self-consistent fields,” *Phys. Rev.*, vol. 97, pp. 1344–1352, Mar 1955.
- [6] H. A. Bethe, “Nuclear many-body problem,” *Phys. Rev.*, vol. 103, pp. 1353–1390, Sep 1956.
- [7] J. Goldstone, “Derivation of the brueckner many-body theory,” *Proceedings of the Royal Society of London A: Mathematical, Physical and Engineering Sciences*, vol. 239, no. 1217, pp. 267–279, 1957.
- [8] F. Coester, “Bound states of a many-particle system,” *Nuclear Physics*, vol. 7, no. Supplement C, pp. 421 – 424, 1958.
- [9] F. Coester and H. Kümmel, “Short-range correlations in nuclear wave functions,” *Nuclear Physics*, vol. 17, no. Supplement C, pp. 477 – 485, 1960.
- [10] H. Kümmel, K. Lührmann, and J. Zabolitzky, “Many-fermion theory in exps- (or coupled cluster) form,” *Physics Reports*, vol. 36, no. 1, pp. 1 – 63, 1978.
- [11] J. C. Slater, “The theory of complex spectra,” *Phys. Rev.*, vol. 34, pp. 1293–1322, Nov 1929.
- [12] E. U. Condon, “The theory of complex spectra,” *Phys. Rev.*, vol. 36, pp. 1121–1133, Oct 1930.
- [13] R. F. Bacher, “The interaction of configurations: $sd - p^2$,” *Phys. Rev.*, vol. 43, pp. 264–269, Feb 1933.
- [14] C. W. Ufford, “Configuration interaction in complex spectra,” *Phys. Rev.*, vol. 44, pp. 732–739, Nov 1933.

- [15] J. Hubbard, “The description of collective motions in terms of many-body perturbation theory,” *Proceedings of the Royal Society of London. Series A, Mathematical and Physical Sciences*, vol. 240, no. 1223, pp. 539–560, 1957.
- [16] N. Hugenholtz, “Perturbation theory of large quantum systems,” *Physica*, vol. 23, no. 1, pp. 481 – 532, 1957.
- [17] H. Schaefer, *Quantum chemistry: the development of ab initio methods in molecular electronic structure theory*. Oxford science publications, Clarendon Press, 1984.
- [18] I. Shavitt and R. J. Bartlett, *Many-Body Methods in Chemistry and Physics: MBPT and Coupled-Cluster Theory*. Cambridge Molecular Science, Cambridge University Press, 2009.
- [19] J. Čížek, “On the correlation problem in atomic and molecular systems. calculation of wavefunction components in urselltype expansion using quantumfield theoretical methods,” *The Journal of Chemical Physics*, vol. 45, no. 11, pp. 4256–4266, 1966.
- [20] J. Čížek and J. Paldus, “Correlation problems in atomic and molecular systems iii. red-erivation of the coupled-pair many-electron theory using the traditional quantum chemical methodst,” *International Journal of Quantum Chemistry*, vol. 5, no. 4, pp. 359–379, 1971.
- [21] J. Čížek and J. Paldus, “Coupled cluster approach,” *Physica Scripta*, vol. 21, no. 3-4, p. 251, 1980.
- [22] P. Piecuch, K. Kowalski, I. S. O. Pimienta, and M. J. McGuire, “Recent advances in electronic structure theory: Method of moments of coupled-cluster equations and renormalized coupled-cluster approaches,” *International Reviews in Physical Chemistry*, vol. 21, no. 4, pp. 527–655, 2002.
- [23] E. Epelbaum, H.-W. Hammer, and U.-G. Meißner, “Modern theory of nuclear forces,” *Rev. Mod. Phys.*, vol. 81, pp. 1773–1825, Dec 2009.
- [24] R. Machleidt and D. Entem, “Chiral effective field theory and nuclear forces,” *Physics Reports*, vol. 503, no. 1, pp. 1 – 75, 2011.
- [25] S. Bogner, R. Furnstahl, and A. Schwenk, “From low-momentum interactions to nuclear structure,” *Progress in Particle and Nuclear Physics*, vol. 65, no. 1, pp. 94 – 147, 2010.
- [26] R. Roth, J. Langhammer, A. Calci, S. Binder, and P. Navrátil, “Similarity-transformed chiral $NN + 3N$ interactions for the ab initio description of ^{12}C and ^{16}O ,” *Phys. Rev. Lett.*, vol. 107, p. 072501, Aug 2011.
- [27] P. Navrátil, J. P. Vary, and B. R. Barrett, “Large-basis ab initio no-core shell model and its application to ^{12}C ,” *Phys. Rev. C*, vol. 62, p. 054311, Oct 2000.

- [28] P. Navrátil, S. Quaglioni, I. Stetcu, and B. R. Barrett, “Recent developments in no-core shell-model calculations,” *Journal of Physics G: Nuclear and Particle Physics*, vol. 36, no. 8, p. 083101, 2009.
- [29] B. R. Barrett, P. Navrátil, and J. P. Vary, “Ab initio no core shell model,” *Progress in Particle and Nuclear Physics*, vol. 69, no. Supplement C, pp. 131 – 181, 2013.
- [30] B. S. Pudliner, V. R. Pandharipande, J. Carlson, S. C. Pieper, and R. B. Wiringa, “Quantum monte carlo calculations of nuclei with $a \leq 7$,” *Phys. Rev. C*, vol. 56, pp. 1720–1750, Oct 1997.
- [31] S. C. Pieper, , and R. B. Wiringa, “Quantum monte carlo calculations of light nuclei,” *Annual Review of Nuclear and Particle Science*, vol. 51, no. 1, pp. 53–90, 2001.
- [32] J. Carlson, S. Gandolfi, F. Pederiva, S. C. Pieper, R. Schiavilla, K. E. Schmidt, and R. B. Wiringa, “Quantum monte carlo methods for nuclear physics,” *Rev. Mod. Phys.*, vol. 87, pp. 1067–1118, Sep 2015.
- [33] K. Tsukiyama, S. K. Bogner, and A. Schwenk, “In-medium similarity renormalization group for nuclei,” *Phys. Rev. Lett.*, vol. 106, p. 222502, Jun 2011.
- [34] K. Tsukiyama, S. K. Bogner, and A. Schwenk, “In-medium similarity renormalization group for open-shell nuclei,” *Phys. Rev. C*, vol. 85, p. 061304, Jun 2012.
- [35] H. Hergert, S. Binder, A. Calci, J. Langhammer, and R. Roth, “Ab initio calculations of even oxygen isotopes with chiral two-plus-three-nucleon interactions,” *Phys. Rev. Lett.*, vol. 110, p. 242501, Jun 2013.
- [36] S. K. Bogner, H. Hergert, J. D. Holt, A. Schwenk, S. Binder, A. Calci, J. Langhammer, and R. Roth, “Nonperturbative shell-model interactions from the in-medium similarity renormalization group,” *Phys. Rev. Lett.*, vol. 113, p. 142501, Oct 2014.
- [37] H. Hergert, S. K. Bogner, T. D. Morris, S. Binder, A. Calci, J. Langhammer, and R. Roth, “Ab initio multireference in-medium similarity renormalization group calculations of even calcium and nickel isotopes,” *Phys. Rev. C*, vol. 90, p. 041302, Oct 2014.
- [38] H. Hergert, “In-medium similarity renormalization group for closed and open-shell nuclei,” *Physica Scripta*, vol. 92, no. 2, p. 023002, 2017.
- [39] S. R. Stroberg, H. Hergert, J. D. Holt, S. K. Bogner, and A. Schwenk, “Ground and excited states of doubly open-shell nuclei from ab initio valence-space hamiltonians,” *Phys. Rev. C*, vol. 93, p. 051301, May 2016.
- [40] S. R. Stroberg, A. Calci, H. Hergert, J. D. Holt, S. K. Bogner, R. Roth, and A. Schwenk, “Nucleus-dependent valence-space approach to nuclear structure,” *Phys. Rev. Lett.*, vol. 118, p. 032502, Jan 2017.

- [41] V. Somà, C. Barbieri, and T. Duguet, “Ab initio gorkov-green’s function calculations of open-shell nuclei,” *Phys. Rev. C*, vol. 87, p. 011303, Jan 2013.
- [42] V. Somà, C. Barbieri, and T. Duguet, “Ab initio self-consistent gorkov-green’s function calculations of semi-magic nuclei: Numerical implementation at second order with a two-nucleon interaction,” *Phys. Rev. C*, vol. 89, p. 024323, Feb 2014.
- [43] V. Somà, A. Cipollone, C. Barbieri, P. Navrátil, and T. Duguet, “Chiral two- and three-nucleon forces along medium-mass isotope chains,” *Phys. Rev. C*, vol. 89, p. 061301, Jun 2014.
- [44] M. Włoch, D. J. Dean, J. R. Gour, M. Hjorth-Jensen, K. Kowalski, T. Papenbrock, and P. Piecuch, “Ab-initio coupled-cluster study of ^{16}O ,” *Phys. Rev. Lett.*, vol. 94, p. 212501, Jun 2005.
- [45] M. Woch, J. R. Gour, P. Piecuch, D. J. Dean, M. Hjorth-Jensen, and T. Papenbrock, “Coupled-cluster calculations for ground and excited states of closed- and open-shell nuclei using methods of quantum chemistry,” *Journal of Physics G: Nuclear and Particle Physics*, vol. 31, no. 8, p. S1291, 2005.
- [46] G. R. Jansen, J. Engel, G. Hagen, P. Navratil, and A. Signoracci, “Ab-initio coupled-cluster effective interactions for the shell model: Application to neutron-rich oxygen and carbon isotopes,” *Phys. Rev. Lett.*, vol. 113, p. 142502, Oct 2014.
- [47] G. R. Jansen, M. D. Schuster, A. Signoracci, G. Hagen, and P. Navrátil, “Open sd -shell nuclei from first principles,” *Phys. Rev. C*, vol. 94, p. 011301, Jul 2016.
- [48] G. Hagen, A. Ekström, C. Forssén, G. R. Jansen, W. Nazarewicz, T. Papenbrock, K. A. Wendt, S. Bacca, N. Barnea, B. Carlsson, C. Drischler, K. Hebeler, M. Hjorth-Jensen, M. Miorelli, G. Orlandini, A. Schwenk, and J. Simonis, “Neutron and weak-charge distributions of the ^{48}Ca nucleus,” *Nature Physics*, vol. 12, pp. 186 EP –, Nov 2015. Article.
- [49] K. Kowalski, D. J. Dean, M. Hjorth-Jensen, T. Papenbrock, and P. Piecuch, “Coupled cluster calculations of ground and excited states of nuclei,” *Phys. Rev. Lett.*, vol. 92, p. 132501, Apr 2004.
- [50] J. R. Gour, P. Piecuch, M. Hjorth-Jensen, M. Włoch, and D. J. Dean, “Coupled-cluster calculations for valence systems around ^{16}O ,” *Phys. Rev. C*, vol. 74, p. 024310, Aug 2006.
- [51] S. Binder, P. Piecuch, A. Calci, J. Langhammer, P. Navrátil, and R. Roth, “Extension of coupled-cluster theory with a noniterative treatment of connected triply excited clusters to three-body hamiltonians,” *Phys. Rev. C*, vol. 88, p. 054319, Nov 2013.
- [52] T. D. Morris, J. Simonis, S. R. Stroberg, C. Stumpf, G. Hagen, J. D. Holt, G. R. Jansen, T. Papenbrock, R. Roth, and A. Schwenk, “Structure of the lightest tin isotopes,” 2017.

- [53] N. Cabibbo, “Unitary symmetry and leptonic decays,” *Phys. Rev. Lett.*, vol. 10, pp. 531–533, Jun 1963.
- [54] M. Kobayashi and T. Maskawa, “Cp-violation in the renormalizable theory of weak interaction,” *Progress of Theoretical Physics*, vol. 49, no. 2, pp. 652–657, 1973.
- [55] I. S. Towner and J. C. Hardy, “The evaluation of v_{ud} , experiment and theory,” *Journal of Physics G: Nuclear and Particle Physics*, vol. 29, no. 1, p. 197, 2003.
- [56] I. S. Towner and J. C. Hardy, “An Improved calculation of the isospin-symmetry-breaking corrections to superallowed Fermi beta decay,” *Phys. Rev.*, vol. C77, p. 025501, 2008.
- [57] I. Towner, “Quenching of spin operators in the calculation of radiative corrections for nuclear beta decay,” *Physics Letters B*, vol. 333, no. 1, pp. 13 – 16, 1994.
- [58] I. Towner, “The nuclear-structure dependence of radiative corrections in superallowed fermi beta-decay,” *Nuclear Physics A*, vol. 540, no. 3, pp. 478 – 500, 1992.
- [59] F. Barker, B. Brown, W. Jaus, and G. Rasche, “Determination of —vud— from fermi decays and the unitarity of the km-mixing matrix,” *Nuclear Physics A*, vol. 540, no. 3, pp. 501 – 519, 1992.
- [60] W. Jaus and G. Rasche, “Nuclear-structure dependence of $o(\alpha)$ corrections to fermi decays and the value of the kobayashi-maskawa matrix element V_{ud} ,” *Phys. Rev. D*, vol. 41, pp. 166–176, Jan 1990.
- [61] J. C. Hardy and I. S. Towner, “Superallowed $0^+ \rightarrow 0^+$ nuclear β decays: A critical survey with tests of the conserved vector current hypothesis and the standard model,” *Phys. Rev. C*, vol. 71, p. 055501, May 2005.
- [62] J. Suhonen and O. Civitarese, “Weak-interaction and nuclear-structure aspects of nuclear double beta decay,” *Physics Reports*, vol. 300, no. 3, pp. 123 – 214, 1998.
- [63] F. T. Avignone, S. R. Elliott, and J. Engel, “Double beta decay, majorana neutrinos, and neutrino mass,” *Rev. Mod. Phys.*, vol. 80, pp. 481–516, Apr 2008.
- [64] S. R. Elliott, A. A. Hahn, and M. K. Moe, “Direct evidence for two-neutrino double-beta decay in ^{82}Se ,” *Phys. Rev. Lett.*, vol. 59, pp. 2020–2023, Nov 1987.
- [65] H. S. Miley, F. T. Avignone, R. L. Brodzinski, J. I. Collar, and J. H. Reeves, “Suggestive evidence for the two-neutrino double- β decay of ^{76}Ge ,” *Phys. Rev. Lett.*, vol. 65, pp. 3092–3095, Dec 1990.
- [66] D. L. Lincoln, J. D. Holt, G. Bollen, M. Brodeur, S. Bustabad, J. Engel, S. J. Novario, M. Redshaw, R. Ringle, and S. Schwarz, “First direct double- β decay q -value measurement of ^{82}Se in support of understanding the nature of the neutrino,” *Phys. Rev. Lett.*, vol. 110, p. 012501, Jan 2013.

- [67] K. Gulyuz, J. Ariche, G. Bollen, S. Bustabad, M. Eibach, C. Izzo, S. J. Novario, M. Redshaw, R. Ringle, R. Sandler, S. Schwarz, and A. A. Valverde, “Determination of the direct double- β -decay q value of ^{96}Zr and atomic masses of $^{90-92,94,96}\text{Zr}$ and $^{92,94-98,100}\text{Mo}$,” *Phys. Rev. C*, vol. 91, p. 055501, May 2015.
- [68] M. Redshaw, G. Bollen, M. Brodeur, S. Bustabad, D. L. Lincoln, S. J. Novario, R. Ringle, and S. Schwarz, “Atomic mass and double- β -decay q value of ^{48}Ca ,” *Phys. Rev. C*, vol. 86, p. 041306, Oct 2012.
- [69] S. Bustabad, G. Bollen, M. Brodeur, D. L. Lincoln, S. J. Novario, M. Redshaw, R. Ringle, S. Schwarz, and A. A. Valverde, “First direct determination of the ^{48}Ca double- β decay q value,” *Phys. Rev. C*, vol. 88, p. 022501, Aug 2013.
- [70] K. Hirata, T. Kajita, M. Koshiba, M. Nakahata, Y. Oyama, N. Sato, A. Suzuki, M. Takita, Y. Totsuka, T. Kifune, T. Suda, K. Takahashi, T. Tanimori, K. Miyano, M. Yamada, E. W. Beier, L. R. Feldscher, S. B. Kim, A. K. Mann, F. M. Newcomer, R. Van, W. Zhang, and B. G. Cortez, “Observation of a neutrino burst from the supernova sn1987a,” *Phys. Rev. Lett.*, vol. 58, pp. 1490–1493, Apr 1987.
- [71] R. M. Bionta, G. Blewitt, C. B. Bratton, D. Casper, A. Ciocio, R. Claus, B. Cortez, M. Crouch, S. T. Dye, S. Errede, G. W. Foster, W. Gajewski, K. S. Ganezer, M. Goldhaber, T. J. Haines, T. W. Jones, D. Kielczewska, W. R. Kropp, J. G. Learned, J. M. LoSecco, J. Matthews, R. Miller, M. S. Mudan, H. S. Park, L. R. Price, F. Reines, J. Schultz, S. Seidel, E. Shumard, D. Sinclair, H. W. Sobel, J. L. Stone, L. R. Sulak, R. Svoboda, G. Thornton, J. C. van der Velde, and C. Wuest, “Observation of a neutrino burst in coincidence with supernova 1987a in the large magellanic cloud,” *Phys. Rev. Lett.*, vol. 58, pp. 1494–1496, Apr 1987.
- [72] C. Hargrove, I. Batkin, M. Sundaresan, and J. Dubeau, “A lead astronomical neutrino detector: Land,” *Astroparticle Physics*, vol. 5, no. 2, pp. 183 – 196, 1996.
- [73] D. B. Cline, G. M. Fuller, W. P. Hong, B. Meyer, and J. Wilson, “Prospects for detection of a cosmologically significant neutrino mass from a galactic supernova neutrino burst using a neutral-current-based detector,” *Phys. Rev. D*, vol. 50, pp. 720–729, Jul 1994.
- [74] G. Ewan, “The sudbury neutrino observatory,” *Nuclear Instruments and Methods in Physics Research Section A: Accelerators, Spectrometers, Detectors and Associated Equipment*, vol. 314, no. 2, pp. 373 – 379, 1992.
- [75] K. Langanke, P. Vogel, and E. Kolbe, “Signal for supernova ν_μ and ν_τ neutrinos in water Čerenkov detectors,” *Phys. Rev. Lett.*, vol. 76, pp. 2629–2632, Apr 1996.
- [76] E. Kolbe, K. Langanke, G. Martnez-Pinedo, and P. Vogel, “Neutrino-nucleus reactions and nuclear structure,” *Journal of Physics G: Nuclear and Particle Physics*, vol. 29, no. 11, p. 2569, 2003.

- [77] O. Benhar, N. Farina, H. Nakamura, M. Sakuda, and R. Seki, “Electron- and neutrino-nucleus scattering in the impulse approximation regime,” *Phys. Rev. D*, vol. 72, p. 053005, Sep 2005.
- [78] E. Fermi, “Versuch einer Theorie der β -Strahlen. I,” *Zeitschrift fur Physik*, vol. 88, pp. 161–177, Mar. 1934.
- [79] F. L. Wilson, “Fermi’s theory of beta decay,” *American Journal of Physics*, vol. 36, no. 12, pp. 1150–1160, 1968.
- [80] B. H. Wildenthal, M. S. Curtin, and B. A. Brown, “Predicted features of the beta decay of neutron-rich sd-shell nuclei,” *Phys. Rev. C*, vol. 28, pp. 1343–1366, Sep 1983.
- [81] B. A. Brown and B. H. Wildenthal, “Corrections to the free-nucleon values of the single-particle matrix elements of the m_1 and gamow-teller operators, from a comparison of shell-model predictions with sd-shell data,” *Phys. Rev. C*, vol. 28, pp. 2397–2413, Dec 1983.
- [82] E. K. Warburton and B. A. Brown, “Effective interactions for the $0p1s0d$ nuclear shell-model space,” *Phys. Rev. C*, vol. 46, pp. 923–944, Sep 1992.
- [83] W. E. Ormand and B. A. Brown, “Isospin-mixing corrections for fp-shell fermi transitions,” *Phys. Rev. C*, vol. 52, pp. 2455–2460, Nov 1995.
- [84] I. S. Towner and F. C. Khanna, “Quenching of allowed gamow-teller β transitions in mirror nuclei,” *Phys. Rev. Lett.*, vol. 42, pp. 51–54, Jan 1979.
- [85] A. Ekström, G. R. Jansen, K. A. Wendt, G. Hagen, T. Papenbrock, S. Bacca, B. Carlsson, and D. Gazit, “Effects of three-nucleon forces and two-body currents on gamow-teller strengths,” *Phys. Rev. Lett.*, vol. 113, p. 262504, Dec 2014.
- [86] S. K. Bogner, H. Hergert, J. D. Holt, A. Schwenk, S. Binder, A. Calci, J. Langhammer, and R. Roth, “Nonperturbative shell-model interactions from the in-medium similarity renormalization group,” *Phys. Rev. Lett.*, vol. 113, p. 142501, Oct 2014.
- [87] J. Suhonen and O. Civitarese, “Probing the quenching of ga by single and double beta decays,” *Physics Letters B*, vol. 725, no. 1, pp. 153 – 157, 2013.
- [88] J. Engel, “Nuclear matrix elements for double-b decay,” *XXVI International Conference on Neutrino Physics and Astrophysics (Neutrino 2014)*, vol. 1666, 2015.
- [89] J. C. Slater, “The theory of complex spectra,” *Phys. Rev.*, vol. 34, pp. 1293–1322, Nov 1929.
- [90] A. Fetter and J. Walecka, *Quantum Theory of Many-particle Systems*. Dover Books on Physics, Dover Publications, 2003.
- [91] G. C. Wick, “The evaluation of the collision matrix,” *Phys. Rev.*, vol. 80, pp. 268–272, Oct 1950.

- [92] D. R. Hartree, “The wave mechanics of an atom with a non-coulomb central field. part i. theory and methods,” *Mathematical Proceedings of the Cambridge Philosophical Society*, vol. 24, no. 1, p. 89110, 1928.
- [93] V. Fock, “Näherungsmethode zur lösung des quantenmechanischen mehrkörperproblems,” *Zeitschrift für Physik*, vol. 61, pp. 126–148, Jan 1930.
- [94] D. Thouless, “Stability conditions and nuclear rotations in the hartree-fock theory,” *Nuclear Physics*, vol. 21, pp. 225 – 232, 1960.
- [95] L. Brillouin, “Les problèmes de perturbations et les champs self-consistents,” *Le journal de physique et le radium*, vol. 3, no. 9, pp. 373–389, 1932.
- [96] P. Pulay, “Convergence acceleration of iterative sequences. the case of scf iteration,” *Chem. Phys. Lett.*, vol. 73, no. 2, pp. 393 – 398, 1980.
- [97] P. Pulay, “Improved scf convergence acceleration,” *J. Comput. Chem.*, vol. 3, no. 4, pp. 556–560, 1982.
- [98] C. G. Broyden, “A class of methods for solving nonlinear simultaneous equations,” *Math. Comput.*, vol. 19, no. 92, pp. 577–593, 1965.
- [99] E. U. Condon, “The theory of complex spectra,” *Phys. Rev.*, vol. 36, pp. 1121–1133, Oct 1930.
- [100] C. D. Sherrill and H. F. Schaefer, “The configuration interaction method: Advances in highly correlated approaches,” vol. 34 of *Advances in Quantum Chemistry*, pp. 143 – 269, Academic Press, 1999.
- [101] C. Møller and M. S. Plesset, “Note on an approximation treatment for many-electron systems,” *Phys. Rev.*, vol. 46, pp. 618–622, Oct 1934.
- [102] J. Rayleigh, *The Theory of Sound*. The Theory of Sound, Macmillan, 1894.
- [103] E. Schrödinger, “Quantification of the eigen value problem,” *Annalen der Physik*, vol. 80, no. 13, pp. 437–490, 1926.
- [104] L. M. Frantz and R. L. Mills, “Many-body basis for the optical model,” *Nuclear Physics*, vol. 15, pp. 16 – 32, 1960.
- [105] B. H. Brandow, “Linked-cluster expansions for the nuclear many-body problem,” *Rev. Mod. Phys.*, vol. 39, pp. 771–828, Oct 1967.
- [106] T. P. Živković, “Existence and reality of solutions of the coupled-cluster equations,” *International Journal of Quantum Chemistry*, vol. 12, no. S11, pp. 413–420, 1977.
- [107] P. Piecuch, S. Zarrabian, J. Paldus, and J. Čížek, “Coupled-cluster approaches with an approximate account of triexcitations and the optimized-inner-projection technique. ii. coupled-cluster results for cyclic-polyene model systems,” *Phys. Rev. B*, vol. 42, pp. 3351–3379, Aug 1990.

- [108] P. Piecuch and K. Kowalski, “In search of the relationship between multiple solutions characterizing coupled-cluster theories,” in *Computational Chemistry: Reviews of Current Trends* (J. Leszczynski, ed.), vol. 5, pp. 1–104, Singapore: World Scientific, 2000.
- [109] N. Moiseyev, *Non-Hermitian Quantum Mechanics*. Cambridge University Press, 2011.
- [110] R. J. Bartlett and M. Musiał, “Coupled-cluster theory in quantum chemistry,” *Rev. Mod. Phys.*, vol. 79, pp. 291–352, Feb 2007.
- [111] G. Hagen, T. Papenbrock, M. Hjorth-Jensen, and D. J. Dean, “Coupled-cluster computations of atomic nuclei,” *Rep. Prog. in Phys.*, vol. 77, p. 096302, Sep 2014.
- [112] P. Szakács and P. R. Surján, “Stability conditions for the coupled cluster equations,” *International Journal of Quantum Chemistry*, vol. 108, no. 12, pp. 2043–2052, 2008.
- [113] “An updated set of basic linear algebra subprograms (blas),” *ACM Trans. Math. Softw.*, vol. 28, p. 135, 2002.
- [114] E. K. U. Gross, E. Runge, and O. Heinonen, *Many-particle theory / E.K.U. Gross, E. Runge, O. Heinonen*. A. Hilger Bristol ; Philadelphia, 1991.
- [115] N. Michel, W. Nazarewicz, M. Płoszajczak, and J. Rotureau, “Antibound states and halo formation in the gamow shell model,” *Phys. Rev. C*, vol. 74, p. 054305, Nov 2006.
- [116] G. Hagen, D. Dean, M. Hjorth-Jensen, and T. Papenbrock, “Complex coupled-cluster approach to an ab-initio description of open quantum systems,” *Physics Letters B*, vol. 656, no. 4, pp. 169 – 173, 2007.
- [117] E. Wigner and J. Griffin, *Group Theory and Its Application to the Quantum Mechanics of Atomic Spectra*. Pure and applied Physics, Academic Press, 1959.
- [118] C. Eckart, “The application of group theory to the quantum dynamics of monatomic systems,” *Rev. Mod. Phys.*, vol. 2, pp. 305–380, Jul 1930.
- [119] T. Hatsuda and T. Kunihiro, “Qcd phenomenology based on a chiral effective lagrangian,” *Physics Reports*, vol. 247, no. 5, pp. 221 – 367, 1994.
- [120] G. P. Lepage and S. J. Brodsky, “Exclusive processes in perturbative quantum chromodynamics,” *Phys. Rev. D*, vol. 22, pp. 2157–2198, Nov 1980.
- [121] S. R. Beane, E. Chang, W. Detmold, H. W. Lin, T. C. Luu, K. Orginos, A. Parreño, M. J. Savage, A. Torok, and A. Walker-Loud, “Deuteron and exotic two-body bound states from lattice qcd,” *Phys. Rev. D*, vol. 85, p. 054511, Mar 2012.
- [122] J. Beringer, J. F. Arguin, R. M. Barnett, K. Copic, O. Dahl, D. E. Groom, C. J. Lin, J. Lys, H. Murayama, C. G. Wohl, W. M. Yao, P. A. Zyla, C. Amsler, M. Antonelli, D. M. Asner, H. Baer, H. R. Band, T. Basaglia, C. W. Bauer, J. J. Beatty, V. I. Belousov, E. Bergren, G. Bernardi, W. Bertl, S. Bethke, H. Bichsel, O. Biebel,

E. Blucher, S. Blusk, G. Brooijmans, O. Buchmueller, R. N. Cahn, M. Carena, A. Cecucci, D. Chakraborty, M. C. Chen, R. S. Chivukula, G. Cowan, G. D'Ambrosio, T. Damour, D. de Florian, A. de Gouv  a, T. DeGrand, P. de Jong, G. Dissertori, B. Dobrescu, M. Doser, M. Drees, D. A. Edwards, S. Eidelman, J. Erler, V. V. Ezhela, W. Fetscher, B. D. Fields, B. Foster, T. K. Gaisser, L. Garren, H. J. Gerber, G. Gerbier, T. Gherghetta, S. Golwala, M. Goodman, C. Grab, A. V. Gritsan, J. F. Grivaz, M. Grunewald, A. Gurtu, T. Gutsche, H. E. Haber, K. Hagiwara, C. Hagmann, C. Hanhart, S. Hashimoto, K. G. Hayes, M. Heffner, B. Heltsley, J. J. Hern  ndez-Rey, K. Hikasa, A. H  cker, J. Holder, A. Holtkamp, J. Huston, J. D. Jackson, K. F. Johnson, T. Junk, D. Karlen, D. Kirkby, S. R. Klein, E. Klemp, R. V. Kowalewski, F. Krauss, M. Kreps, B. Krusche, Y. V. Kuyanov, Y. Kwon, O. Lahav, J. Laiho, P. Langacker, A. Liddle, Z. Ligeti, T. M. Liss, L. Littenberg, K. S. Lugovsky, S. B. Lugovsky, T. Mannel, A. V. Manohar, W. J. Marciano, A. D. Martin, A. Masoni, J. Matthews, D. Milstead, R. Miquel, K. M  nig, F. Moortgat, K. Nakamura, M. Narain, P. Nason, S. Navas, M. Neubert, P. Nevski, Y. Nir, K. A. Olive, L. Pape, J. Parsons, C. Patrignani, J. A. Peacock, S. T. Petcov, A. Piepke, A. Pomarol, G. Punzi, A. Quadt, S. Raby, G. Raffelt, B. N. Ratcliff, P. Richardson, S. Roesler, S. Rolli, A. Romaniouk, L. J. Rosenberg, J. L. Rosner, C. T. Sachrajda, Y. Sakai, G. P. Salam, S. Sarkar, F. Sauli, O. Schneider, K. Scholberg, D. Scott, W. G. Seligman, M. H. Shaevitz, S. R. Sharpe, M. Silari, T. Sj  strand, P. Skands, J. G. Smith, G. F. Smoot, S. Spanier, H. Spieler, A. Stahl, T. Stanev, S. L. Stone, T. Sumiyoshi, M. J. Syphers, F. Takahashi, M. Tanabashi, J. Terning, M. Titov, N. P. Tkachenko, N. A. T  rnqvist, D. Tovey, G. Valencia, K. van Bibber, G. Venanzoni, M. G. Vincter, P. Vogel, A. Vogt, W. Walkowiak, C. W. Walter, D. R. Ward, T. Watari, G. Weiglein, E. J. Weinberg, L. R. Wiencke, L. Wolfenstein, J. Womersley, C. L. Woody, R. L. Workman, A. Yamamoto, G. P. Zeller, O. V. Zenin, J. Zhang, R. Y. Zhu, G. Harper, V. S. Lugovsky, and P. Schaffner, “Review of particle physics,” *Phys. Rev. D*, vol. 86, p. 010001, Jul 2012.

- [123] D. R. Entem and R. Machleidt, “Accurate charge-dependent nucleon-nucleon potential at fourth order of chiral perturbation theory,” *Phys. Rev. C*, vol. 68, p. 041001, Oct 2003.
- [124] P. Navr  til, “Local three-nucleon interaction from chiral effective field theory,” *Few-Body Systems*, vol. 41, pp. 117–140, Dec 2007.
- [125] R. Roth, S. Binder, K. Vobig, A. Calci, J. Langhammer, and P. Navr  til, “Medium-mass nuclei with normal-ordered chiral $NN + 3N$ interactions,” *Phys. Rev. Lett.*, vol. 109, p. 052501, Jul 2012.
- [126] S. Levit and D. Orgad, “Statistics of hartree-fock levels in small disordered systems,” *Physical review. B, Condensed matter*, vol. 60, no. 8, pp. 5549–5560, 1999.
- [127] H. J. Lipkin, “Center-of-mass motion in the nuclear shell model,” *Phys. Rev.*, vol. 110, pp. 1395–1397, Jun 1958.
- [128] D. Gloeckner and R. Lawson, “Spurious center-of-mass motion,” *Physics Letters B*, vol. 53, no. 4, pp. 313 – 318, 1974.

- [129] R. F. Bishop, M. F. Flynn, M. C. Boscá, E. Buenda, and R. Guardiola, “Translationally invariant coupled cluster theory for simple finite systems,” *Phys. Rev. C*, vol. 42, pp. 1341–1360, Oct 1990.
- [130] A. Nogga, H. Kamada, W. Glöckle, and B. R. Barrett, “The α particle based on modern nuclear forces,” *Phys. Rev. C*, vol. 65, p. 054003, May 2002.
- [131] C. M. Vincent, “Optimal separation of center-of-mass motion,” *Phys. Rev. C*, vol. 8, pp. 929–937, Sep 1973.
- [132] G. Hagen, T. Papenbrock, and D. J. Dean, “Solution of the center-of-mass problem in nuclear structure calculations,” *Phys. Rev. Lett.*, vol. 103, p. 062503, Aug 2009.
- [133] G. R. Jansen, “Spherical coupled-cluster theory for open-shell nuclei,” *Phys. Rev. C*, vol. 88, p. 024305, Aug 2013.
- [134] G. H. Diercksen, B. O. Roos, and A. J. Sadlej, “Legitimate calculation of first-order molecular properties in the case of limited ci functions. dipole moments,” *Chemical Physics*, vol. 59, no. 1, pp. 29 – 39, 1981.
- [135] M. Ernzerhof, C. Marian, and S. Peyerimhoff, “Energy derivative versus expectation value approach: the dipole moment of co,” *Chemical Physics Letters*, vol. 204, no. 1, pp. 59 – 64, 1993.
- [136] D. J. Rowe, “Equations-of-motion method and the extended shell model,” *Rev. Mod. Phys.*, vol. 40, pp. 153–166, Jan 1968.
- [137] C. Lanczos, “An iteration method for the solution of the eigenvalue problem of linear differential and integral operators,” *Journal of research of the National Bureau of Standards (1934)*, vol. 45, pp. 255–282, 1950 10.
- [138] W. E. Arnoldi, “The principle of minimized iterations in the solution of the matrix eigenvalue problem,” *Quarterly of applied mathematics*, vol. 9, no. 1, pp. 17–29, 1951.
- [139] R. Lehoucq, D. Sorensen, and C. Yang, *ARPACK Users’ Guide*. Society for Industrial and Applied Mathematics, 1998.
- [140] S. M. Reimann and M. Manninen, “Electronic structure of quantum dots,” *Rev. Mod. Phys.*, vol. 74, p. 1238, 2002.
- [141] H.-A. Engel, V. N. Golovach, D. Loss, L. M. K. Vandersypen, J. M. Elzerman, R. Hanson, and L. P. Kouwenhoven, “Measurement Efficiency and n -Shot Readout of Spin Qubits,” *Phys. Rev. Lett.*, vol. 93, p. 106804, 2004.
- [142] J. Birman, R. Nazmitdinov, and V. Yukalov, “Effects of symmetry breaking in finite quantum systems,” *Phys. Rep.*, vol. 526, no. 1, pp. 1 – 91, 2013. Effects of symmetry breaking in finite quantum systems.

- [143] S. Tarucha, D. G. Austing, T. Honda, R. J. van der Hage, and L. P. Kouwenhoven, “Shell Filling and Spin Effects in a Few Electron Quantum Dot,” *Phys. Rev. Lett.*, vol. 77, p. 3613, 1996.
- [144] M. P. Lohne, “Coupled-cluster studies of quantum dots,” Master’s thesis, University of Oslo, 2010.
- [145] “*NIST Digital Library of Mathematical Functions*.” <http://dlmf.nist.gov/>, Release 1.0.14 of 2016-12-21, 2016. F. W. J. Olver, A. B. Olde Daalhuis, D. W. Lozier, B. I. Schneider, R. F. Boisvert, C. W. Clark, B. R. Miller and B. V. Saunders, eds.
- [146] I. Lindgren, “The rayleigh-schrodinger perturbation and the linked-diagram theorem for a multi-configurational model space,” *J. Phys. Pt. B Atom. M. P.*, vol. 7, no. 18, p. 2441, 1974.
- [147] J. Høgberget, “Quantum Monte-Carlo Studies of Generalized Many-body Systems,” Master’s thesis, University of Oslo, 2013.
- [148] V. K. B. Olsen, “Full Configuration Interaction Simulation of Quantum Dots,” Master’s thesis, University of Oslo, 2013.
- [149] N. M. Parzuchowski, T. D. Morris, and S. K. Bogner, “Ab initio excited states from the in-medium similarity renormalization group,” *Phys. Rev. C*, vol. 95, p. 044304, Apr 2017.
- [150] K. Emrich, “An extension of the coupled cluster formalism to excited states (i),” *Nuclear Physics A*, vol. 351, no. 3, pp. 379 – 396, 1981.
- [151] K. Emrich, “An extension of the coupled cluster formalism to excited states: (ii). approximations and tests,” *Nuclear Physics A*, vol. 351, no. 3, pp. 397 – 438, 1981.
- [152] K. Emrich and J. Zabolitzky, “Negative parity states in ^{16}O from coupled-cluster equations,” *Nuclear Physics A*, vol. 351, no. 3, pp. 439 – 455, 1981.
- [153] J. F. Stanton and R. J. Bartlett, “The equation of motion coupledcluster method. a systematic biorthogonal approach to molecular excitation energies, transition probabilities, and excited state properties,” *The Journal of Chemical Physics*, vol. 98, no. 9, pp. 7029–7039, 1993.
- [154] G. Hagen, M. Hjorth-Jensen, G. R. Jansen, R. Machleidt, and T. Papenbrock, “Continuum effects and three-nucleon forces in neutron-rich oxygen isotopes,” *Phys. Rev. Lett.*, vol. 108, p. 242501, Jun 2012.
- [155] A. Ekström, G. R. Jansen, K. A. Wendt, G. Hagen, T. Papenbrock, B. D. Carlsson, C. Forssén, M. Hjorth-Jensen, P. Navrátil, and W. Nazarewicz, “Accurate nuclear radii and binding energies from a chiral interaction,” *Phys. Rev. C*, vol. 91, p. 051301, May 2015.

- [156] F. Halzen and A. D. Martin, *Quarks and Leptons: An Introductory Course in Modern Particle Physics*. 1984.
- [157] J. C. Hardy and I. S. Towner, “Superallowed $0^+ \rightarrow 0^+$ nuclear β decays: A critical survey with tests of the conserved vector current hypothesis and the standard model,” *Phys. Rev. C*, vol. 71, p. 055501, May 2005.
- [158] I. S. Towner and J. C. Hardy, “Improved calculation of the isospin-symmetry-breaking corrections to superallowed fermi β decay,” *Phys. Rev. C*, vol. 77, p. 025501, Feb 2008.
- [159] K. Kubodera, J. Delorme, and M. Rho, “Axial currents in nuclei,” *Phys. Rev. Lett.*, vol. 40, pp. 755–758, Mar 1978.
- [160] E. Oset and M. Rho, “Axial currents in nuclei: The gamow-teller matrix element,” *Phys. Rev. Lett.*, vol. 42, pp. 47–50, Jan 1979.
- [161] D. Wilkinson, “Analysis of neutron beta decay,” *Nuclear Physics A*, vol. 377, no. 2, pp. 474 – 504, 1982.
- [162] J. Suhonen, *From Nucleons to Nucleus*. Theoretical and Mathematical Physics, Berlin, Germany: Springer, 2007.